

# **Stratospheric Water Vapour in the Tropics**

**Observations by Ground-Based Microwave Radiometry**

Sven H W Golchert



Institut für Umwelphysik  
Universität Bremen  
2009



# **Stratospheric Water Vapour in the Tropics**

**Observations by Ground-Based Microwave Radiometry**

vom Fachbereich Physik und Elektrotechnik  
der Universität Bremen

zur Erlangung des akademischen Grades eines  
Doktor der Naturwissenschaften (Dr. rer. nat.)  
genehmigte Dissertation

von  
Dipl.-Phys. Sven Heinrich Wolfgang Golchert  
aus Bremen

1. Gutachter: Prof. Dr. Justus Notholt
2. Gutachter: Prof. Dr. Klaus F. Künzi

Eingereicht am 9. Januar 2009



put “me” in the equation it’s alright

*Sonic Youth — Mote*



# Abstract

This thesis reports on observations of tropical stratospheric water vapour by the ground-based microwave radiometer/spectrometer WaRAM2 in 2007. The 22 GHz receiver is set up at Mérida Atmospheric Research Station on top of Pico Espejo, Venezuela ( $8^{\circ}32'N$ ,  $71^{\circ}03'W$ , 4765 m above sea level). It is the only such sensor that continuously operates at tropical latitudes. The high altitude site is ideally suitable for microwave observations, because most tropospheric water vapour is located below the sensor.

Water vapour plays a key role in middle atmospheric processes. Because of its large infrared resonance, it strongly participates in the radiative budget, both in terms of a greenhouse effect at lower altitudes and radiative cooling at higher altitudes. It is a source gas for the highly reactive hydroxyl radical, and exerts indirect effects on ozone destruction in the formation of polar stratospheric clouds. Due to its long lifetime, water vapour also serves as a dynamical tracer.

Several studies indicate a sustained increase in stratospheric water vapour over the second half of the 20th century, which is only partly explained by a concurrent increase in methane. The processes governing water vapour distribution, variability, and trends are still not sufficiently understood. Modelling capacity is currently restricted by the uncertainty and sparse availability of suitable observations, and their inherent discrepancies. Continuous long-term time series of stratospheric water vapour are of particular importance in the separation of trend signals from the large seasonal and annual variations in water vapour entering the stratosphere.

This work summarises existing water vapour observation techniques and their evolution. It demonstrates the utility of WaRAM2 measurements for mitigating the current observational shortcomings. The discussion focusses on improvements to the existing retrieval set-up, which eliminate undesired oscillations in the retrieved profiles. It also devotes detail to some issues that

have been identified in the data. The range of the WaRAM2 retrievals presented here is limited to 30 – 50 km at roughly 10 km vertical resolution, but could be extended downwards by refinements to the retrieval set-up that are currently being investigated. A numerical experiment supports the sensor's capacity to study seasonal variations in stratospheric water vapour entry levels. WaRAM2 results are compared to correlative data from Aura/MLS, yielding good agreement at 33 km. At 44 km, WaRAM2 is 0.7 ppmv (10%) lower than MLS on average.

Keywords: water vapour, stratosphere, tropics, microwave remote sensing, ground-based observation

# Danksagung

Im Gedanken an die Unterstützung, die ich auf dem Weg zu dieser Arbeit erfahren habe, assoziiere ich den Anblick des Sternenhimmels; und kaum dass ich meine, alle Beteiligten gezählt zu haben, stoße ich auf weitere. — Allen, die mich in meinem Studium, meiner Arbeit, und darüber hinaus unterstützt haben, möchte ich herzlich für den Beitrag danken, den sie damit auch für das Zustandekommen dieser Arbeit geleistet haben.

Meinem Betreuer Justus Notholt danke ich für die Gelegenheit, diese Arbeit in seiner bemerkenswert herzlichen Arbeitsgruppe Fernerkundung durchzuführen, seine Geduld und Anregungen im Umgang mit den außergewöhnlichen Widrigkeiten, denen ich im Rahmen dieser Arbeit begegnet bin, sowie für seine Rücksichtnahme auf meine familiären Belange. Klaus F. Künzi danke ich für die Übernahme des Koreferats sowie sein persönliches Interesse am Fortgang dieser Arbeit und zahlreiche hilfreiche Kommentare. Die hier gezeigten Daten verdanke ich seinem persönlichen Einsatz für den Wiederaufbau des WaRAM2, ohne den das Gerät nicht im Dezember 2006 wieder in Betrieb gegangen wäre. Beiden danke ich für das entgegengebrachte Vertrauen und die frühe Gelegenheit, Verantwortung zu übernehmen.

Meinen ehemaligen und jetzigen KollegInnen danke ich für das persönliche Klima in der Arbeitsgruppe und die ausgeprägte Bereitschaft zu gegenseitiger Unterstützung und lebhaften Diskussionen, auch abseits der Wissenschaft, sowie für das Wellness-Geschenk auf der Zielgeraden dieser Arbeit, das mir in wohliger Erinnerung bleibt. Einigen möchte ich besonders danken: Manuel Quack hat das WaRAM2 gebaut — hierfür danke ich auch allen UnterstützerInnen — und zahlreiche Vorarbeiten zur Auswertung geleistet; Mathias Palm hat mit fachlicher Betreuung, Retrieval-Diskussionen und seinen Ermunterungen, meinen Ergebnissen zu vertrauen, viel zu den Resultaten beigetragen, ferner zusammen mit Christoph Hoffmann eine gleicher-

maßen kurzweilige wie produktive Büroatmosphäre geschaffen und Teile des Manuskripts korrekturgelesen; Tine Weinzierl, Birgit Teuchert und Peter Grupe haben mir die Arbeit mit vielfältiger praktischer Unterstützung erleichtert. Nochmals Danke!

Gerd Hochschild und Jochen Groß von der MIRA Gruppe am Forschungszentrum Karlsruhe danke ich für die hervorragende Zusammenarbeit. Ohne ihren Einsatz für die Infrastruktur in Mérida und für die Beseitigung technischer Probleme wären die hier gezeigten Messungen nicht zustande gekommen. Gerhard Kopp danke ich für seine Unterstützung mit dem Retrieval.

Pedro Hoffmann von der Universidad de Los Andes (ULA), Mérida, hat unverzichtbare Beiträge für diese Arbeit geleistet, zeitweise unterstützt von Eduardo Diez y Riega V. und Silvia M. Calderón. Den ersten beiden und ihren Familien danke ich außerdem für die herzliche Aufnahme und hervorragende Betreuung vor Ort, mit einem besonderen Dank an Edith Hoffmann, deren Unterstützung die Dienstreisen nach Mérida fast leichter gemacht hat als eine Zugfahrt nach Delmenhorst. Den fortwährenden Interventionen von Marcos A. Peñaloza Murillo gegen unsere Arbeit in der MARS verdanke ich zu gewissem Grad einen dreiwöchigen Weihnachtsurlaub in Venezuela, wenn auch auf Kosten einer einjährigen Projektverzögerung. E. Tatiana Perez-Valero danke ich, dass sie mich bei meiner ersten Ankunft davor bewahrt hat, in Maiquetía zu stranden. Die folgende Busfahrt durch die Anden werde ich nicht vergessen. Ferner gilt mein Dank der ULA (Betrieb der MARS), der Sistema Teleférico de Mérida (Zugang zur Station) und ihren fröhlichen MitarbeiterInnen, sowie dem Instituto Nacional de Parques (INPARQUES, Erlaubnis zur Arbeit im Nationalpark Sierra Nevada).

Für die Bereitstellung der in dieser Arbeit verwendeten Daten danke ich den WissenschaftlerInnen des ECMWF<sup>1</sup>, des HALOE- und des MLS-Projekts<sup>2</sup>, sowie dem beteiligten Personal.

Die Universität Bremen sowie die Deutsche Forschungsgemeinschaft (Kennzeichen 50-EE-0010) haben Teile dieser Arbeit finanziert.

---

1 ECMWF operational data used in this work have been provided by ECMWF.

2 UARS/HALOE and Aura/MLS data used in this work were acquired as part of the NASA's Earth-Sun System Division and archived and distributed by the Goddard Earth Sciences (GES) Data and Information Services Center (DISC) Distributed Active Archive Center (DAAC). Aura/MLS analyses and visualizations used in this work were produced with the Giovanni online data system, developed and maintained by NASA GES DISC.

---

Randall Munroes großartiger Web-Comic XKCD hat mich selbst dann aufgemuntert, wenn sonst mal wieder alles den Bach runterging, und findet deshalb hier seinen angemessenen Platz an der Schnittstelle zwischen Wissenschaft und dem restlichen Leben.

Meinen FreundInnen danke ich für ihre vielfältige Unterstützung, Aufmunterung und Abwechslung, für die Möglichkeiten, Abstand zu nehmen, Quatsch zu machen, Perspektiven zu wechseln, und sanft wieder auf den Boden der Tatsachen zurückzufinden. Ich freue mich sehr über Eure Hilfe, ohne die mich diese Arbeit viel mehr Nerven gekostet hätte. Besonders erwähnen möchte ich die großen und kleinen Anteile von Neele Jargstorf, Jan Sparsam, Jana Witzenzellner, Christine Kirchhoff, Claudia Ribken, Mascha Scholz, Christoph Engemann und Anne Reuper. Dieser Dank gilt auch meinen Mitbewohnerinnen Dagmar Koch und Ute Schmitt. Zusammen mit Euch und Britta Schülzke, Uschy Weber, Arno Schoppenhorst und den Kindern Paula, Lotta, Julian und Enno, habe ich Kraft für diese Arbeit in einem gemütlichen Zuhause getankt. Ganz besonders danke ich Euch für Eure Geduld, wenn die Wissenschaft sich mal wieder vor die Reproduktionsarbeit gedrängelt hat. Dagmar und Arno danke ich zudem für die tollen lebenslusterhaltenden Maßnahmen beim Endspurt.

Kaddi Barsch ist mit mir nicht nur durch mehr Höhen und Tiefen dieser Arbeit gegangen als jeder andere Mensch; Du warst Fels in der Brandung, Kompass bei Donner, Sturm und Nacht, und hast mich mit einer wunderbaren und einzigartigen Aufmerksamkeit beschenkt. Diese Momente bleiben, und ich bin außerordentlich dankbar und glücklich, sie erlebt zu haben.

Meinen Eltern, Gudrun und Wolfgang Golchert, danke ich ganz besonders für ihre umfangreiche Unterstützung, die selten an Rechenschaft gebunden war und mir erlaubt hat, vieles auszuprobieren, was mich jetzt ausmacht. Ich freue mich sehr, den Abschluss dieser Arbeit zusammen mit Euch feiern zu können.

Zu guter Letzt danke ich Nieves von ganzem Herzen — für die neue und wunderbare Seite, von der Du mich das Leben betrachten lässt, und die nicht immer sanfte Beharrlichkeit, mit der Du mich an die wesentlichen Dinge erinnerst, Schlafen und Lachen zum Beispiel.

*Good enough.*



# Contents

<b>Abstract</b>	vii
<b>Danksagung</b>	ix
<b>1 Introduction</b>	1
<b>2 Water Vapour in the Atmosphere</b>	5
2.1 Basic Structure of the Atmosphere	5
2.2 Stratospheric Dynamics	8
2.3 Stratospheric Water Vapour	8
2.3.1 Dryness of the (Lower) Stratosphere	11
2.3.2 Trends (Past and Future)	13
2.4 Effects on Climate	14
<b>3 Water Vapour Observation Techniques</b>	17
3.1 <i>In Situ</i> Methods	18
3.1.1 Absorption Hygrometers	19
3.1.2 MOZAIC	22
3.1.3 Psychrometers	22
3.1.4 Dew/Frost Point Hygrometers	23
3.1.5 Optical Hygrometers	27
3.1.6 Photofragment Fluorescence Hygrometers	28
3.1.7 Tunable Diode Laser Hygrometers	32
3.1.8 Mass Spectrometry Hygrometers	36
3.2 Remote Sensing	37
3.2.1 Microwave Radiometry/Spectrometry	39
3.2.2 FOURIER Transform Spectroscopy	44
3.2.3 Monochromating Sensors	47
3.2.4 Global Positioning System	50
3.2.5 Light Detection and Ranging	51

---

<b>4 Radiometric Observation and Retrieval</b>	55
4.1 Atmospheric Emission	55
4.1.1 Rotational Transitions	55
4.1.2 Effects on Line Shape and Strength	56
4.1.3 Continua	59
4.2 Radiative Transfer	59
4.3 Receiver Set-Up	60
4.3.1 Path Length Modulator	62
4.3.2 Local Oscillator	64
4.3.3 Low Noise Amplifier	64
4.3.4 Spectrometer	65
4.4 Measurement Calibration	66
4.4.1 Frequency Calibration	66
4.4.2 Total-Power Calibration	67
4.4.3 Receiver Noise Temperature	68
4.5 Integration of Spectra	69
4.6 Retrieval of Geophysical Parameters	70
4.7 Retrieval Set-Up	74
<b>5 Results and Comparisons</b>	77
5.1 Instrument Characterisation	77
5.1.1 Frequency Stability	78
5.1.2 Spectrometer Resolution	80
5.1.3 Linearity	80
5.1.4 Baseline	88
5.1.5 Synthetic Retrieval	99
5.2 Results	101
5.2.1 Cold Load Radiance	102
5.2.2 Retrieval Characteristics	104
5.2.3 Retrieved Stratospheric Water Vapour	106
5.2.4 Discussion	108
5.3 Comparison	112
5.3.1 Aura/MLS	113
<b>6 Conclusions</b>	119

<b>Appendix</b>	121
<b>A Humidity Expressions</b>	123
<b>B Bibliography</b>	127



# List of Figures

2.1 FASCOD tropical temperature profile	6
2.2 Aspects of stratospheric dynamics	9
2.3 FASCOD tropical H <sub>2</sub> O profile	10
2.4 Atmospheric tape recorder from HALOE data	12
2.5 Origin of H <sub>2</sub> O at $\theta = 400$ K	13
3.1 Absolute and relative humidity	21
3.2 H <sub>2</sub> O and O <sub>2</sub> absorption around LYMAN- $\alpha$ wavelength	27
3.3 Improvement in laser absorption signal-to-noise ratio by wavelength modulation spectroscopy	33
4.1 Pressure broadening of rotational transitions	58
4.2 Schematic of WaRAM2 set-up	61
4.3 Frequency calibration	67
4.4 Total-power calibration	68
4.5 Receiver noise temperature (2004, 2005, and 2007)	69
4.6 Integration of spectra	71
5.1 Spectrometer frequency stability	78
5.2 Frequency shift between modelled and measured spectra	79
5.3 Spectrometer resolution bandwidth	80
5.4 Regions of seemingly enhanced noise in spectra	82
5.5 Systematic deviation between odd and even channels	82
5.6 Raw spectra at 8° and 46° elevation, and their ratios, for different transmission line attenuation	84
5.7 Sequence of mean ratios, <i>cf.</i> figure 5.6, and quotients of consecutive pairs of mean ratio	85
5.8 Channel-wise quotients of the ratio data, <i>cf.</i> figure 5.6	87

5.9	Quotient data from figure 5.8, odd channel readings divided by even channels	88
5.10	Illustration of how standing waves are averaged out by path length modulation	90
5.11	Effect of observing the cold calibration load at different angles, single and integrated spectra, January	91
5.12	(similar to figure 5.11, data taken in February)	91
5.13	(similar to figure 5.11, data taken in March)	92
5.14	(similar to figure 5.11, data taken in April)	92
5.15	Analysis of the evolution of standing waves on cold calibration load spectra	94
5.16	Illustration of a baseline fit for standing waves	98
5.17	Tropical lower stratospheric H <sub>2</sub> O abundance from HALOE data, zonal average 12°N–12°S.	99
5.18	Water vapour retrieved from artificial spectra, modelled according to HALOE data above	100
5.19	Retrieval from artificial spectra compared to HALOE data	101
5.20	Cold load radiance fit	103
5.21	Retrieval characteristics	105
5.22	WaRAM2 retrieved water vapour in 2007	106
5.23	WaRAM2 compared to HALOE, similar to figure 5.19, for qualitative impression of retrieval performance	107
5.24	Averaging kernels for three individual WaRAM2 results	109
5.25	Peak responses and centres of altitude of selected averaging kernels	110
5.26	Atmospheric state retrieval response to baseline polynomial and standing wave fit	111
5.27	Magnitude of baseline offset fitted to individual measurements	112
5.28	Aura/MLS water vapour, best matched in location and time with WaRAM2 measurements	114
5.29	Simulation of data from figure 5.28 as would be seen by WaRAM2	114
5.30	WaRAM2 results in relation to simulated MLS, Overview	115
5.31	WaRAM2 results in relation to simulated MLS at 24 km	115
5.32	WaRAM2 results in relation to simulated MLS at 33 km	116
5.33	WaRAM2 results in relation to simulated MLS at 44 km	117

# List of Tables

3.1	Remote sensors for observation of stratospheric water vapour	37
3.2	Ground-based microwave receivers at 22 GHz	40
5.1	WaRAM2 measurements in 2007	102



# List of Abbreviations

a.s.l. ....	above sea level [40]
ACE-FTS .....	Advanced Chemistry Experiment — FOURIER Transform Spectrometer [46]
ACE-MAESTRO	Advanced Chemistry Experiment — Measurement of Aerosol Extinction in the Stratosphere and Troposphere Retrieved by Occultation [46]
ACECHEM .....	Atmospheric Composition Explorer for Chemistry and Climate Interaction [43]
AGNES .....	<i>Automatisches GNSS-Netz Schweiz</i> , [German] Swiss Automatic GNSS-Network [50]
AIDA .....	Aerosol Interactions and Dynamics in the Atmosphere [17]
AIRS .....	Atmospheric Infrared Sounder [20]
ALIAS .....	Aircraft Laser Infrared Absorption Spectrometer [36]
ALOMAR .....	Arctic Lidar Observatory for Middle Atmosphere Research [40]
AMSOS .....	Airborne Microwave Stratospheric Observing System [41]
AOS .....	acousto optical spectrometer [65]
ARTS .....	Atmospheric Radiative Transfer Simulator [74]
ASTRO-SPAS ...	Astronomical Shuttle Pallet Satellite [48]
ATLAS .....	Atmospheric Laboratory for Applications and Science [42]
CCD .....	charge-coupled device [48]
CFH .....	University of Colorado cryogenic frost point hygrometer [25]
CHAMP .....	Challenging Minisatellite Payload [51]
CIRES .....	Cooperative Institute for Research in Environmental Sciences [36]

---

CNES	.....	<i>Centre National d'Études Spatiales</i> , [French] National Center for Space Research [35]
CNRS	.....	<i>Centre National de la Recherche Scientifique</i> , [French] National Center for Scientific Research [40]
CRISTA-NF	.....	Cryogenic Infrared Spectrometers and Telescopes for the Atmosphere — New Frontiers [48]
DIAL	.....	differential absorption lidar [51]
DLH	.....	Diode Laser Hygrometer [34]
DLR	.....	<i>Deutsches Zentrum für Luft- und Raumfahrt</i> , [German] German Aerospace Center [34]
DOAS	.....	differential optical absorption spectroscopy [52]
ECMWF	.....	European Centre for Medium-Range Weather Forecasts [12]
EOS	.....	Earth Observing System [42]
ESA	.....	European Space Agency [43]
FFTS	.....	fast FOURIER transform spectrometer [41]
FIRS-2	.....	Far-infrared Spectrometer 2 [47]
FISH	.....	Fast <i>In Situ</i> Stratospheric Hygrometer [30]
FLASH	.....	Fluorescent Airborne Stratospheric Hygrometer [31]
FLASH-B	.....	Fluorescent Advanced Stratospheric Hygrometer for Balloon [31]
FMS	.....	frequency modulation spectroscopy [32]
FTIR	.....	FOURIER transform infrared [44]
FWHM	.....	full width at half maximum [57]
FZ Karlsruhe	....	<i>Forschungszentrum Karlsruhe</i> , [German] Research Center Karlsruhe [17]
Giovanni	.....	GES DISC DAAC Interactive Online Visualization and Analysis Infrastructure; Goddard Earth Sciences, Data and Information Services Center, Distributed Active Archive Center [113]
GLORIA-AB	....	Global Radiance Limb Imager Experiment for the Atmosphere — Airborne [47]
GNSS	.....	global navigation satellite system [50]
GOMOS	.....	Global Ozone Monitoring by Occultation of Stars [50]
GPS	.....	Global Positioning System [50]
HALO	.....	High Altitude and Long Range Research Aircraft [47]

- 
- HALOE . . . . . Halogen Occultation Experiment [48]
- Harvard ICOS . . . . . Harvard Integrated Cavity Output Spectroscopy sensor  
[36]
- HIAPER . . . . . High-performance Instrumented Airborne Platform for  
Environmental Research [34]
- HIBISCUS . . . . . Impact of tropIcal Convection on the Upper troposphere  
and lower Stratosphere at gloBal Scale (*sic*  
) [35]
- IAP . . . . . *Institut für Angewandte Physik*, [German] Institute of  
Applied Physics, University of Bern [40]
- ICG, FZ Jülich . . . . . *Institut für Chemie und Dynamik der Geosphäre, For-*  
*schungszentrum Jülich*, [German] Institute of Chemistry  
and Dynamics of the Geosphere, Research Centre Jülich  
[47]
- IEAE . . . . . International Atomic Energy Agency [11]
- IF . . . . . intermediate frequency [61]
- IMIPAS . . . . . Imaging MIPAS [47]
- IMK . . . . . *Institut für Meteorologie und Klimaforschung*, [German]  
Institute for Meteorology and Climate Research, FZ Karl-  
ruhe [40]
- IR . . . . . infrared [7]
- IUP . . . . . *Institut für Umweltphysik*, [German] Institute of Envi-  
ronmental Physics, University of Bremen [40]
- IWV . . . . . integrated water vapour [125]
- JLH . . . . . JPL Laser Hygrometer [33]
- KARL . . . . . Koldewey Aerosol RAMAN Lidar [52]
- LASE . . . . . Lidar Atmospheric Sensing Experiment [53]
- LEANDRE II . . . . . *Lidar Embarque pour l'etude des Aerosols et des Nu-*  
*ages, de l'interaction Dynamique-Rayonnement et du cy-*  
*cle de l'Eau*, [French] Lidar for the Study of Aerosols  
and Clouds, of Interactions Between Dynamics and Ra-  
diation, and of the Water Cycle [53]
- LNA . . . . . low-noise amplifier [61]
- LO . . . . . local oscillator [64]
- MAHRSI . . . . . Middle Atmosphere High Resolution Spectrograph In-  
vestigation [49]

MARS .....	Mérida Atmospheric Research Station (Estación de Investigación Ambiental Humboldt, Pico Espejo, 8°32'N 71°03'W, 4765 m a.s.l.) [55]
MARSCHALS ..	Millimetre-wave Airborne Receiver for Spectroscopy Characterisation of Atmospheric Limb-Sounding [43]
MAS .....	Millimeter-wave Atmospheric Sounder [42]
MASTER .....	Millimeter Wave Acquisitions for Stratosphere/Troposphere Exchange Research [43]
MIAWARA .....	Middle Atmospheric Water Vapour Radiometer [40]
MIAWARA-C ...	MIAWARA — Compact [40]
MIPAS .....	Michelson Interferometer for Passive Atmospheric Sounding [45]
MIRA .....	<i>Millimeterwellenradiometer</i> , [German] Millimetre Wave Radiometer [40]
MLS .....	Microwave Limb Sounder [42]
MobRa .....	Mobile Radiometer [40]
MOZAIC I+II ...	Measurements of Ozone and Water Vapour by Airbus In-service Aircraft [22]
MOZAIC III ...	Measurements of Ozone, Water Vapour, Carbon Monoxide and Nitrogen Oxides by Airbus In-service Aircraft [22]
MPIfR .....	<i>MAX-PLANCK-Institut für Radioastronomie</i> , [German] MAX PLANCK Institute for Radio Astronomy [65]
MPS .....	<i>MAX-PLANCK-Institut für Sonnensystemforschung</i> , [German] MAX PLANCK Institute for Solar System Research [40]
NASA .....	National Aeronautics and Space Administration [24]
NASA/GSFC ....	(NASA) Goddard Space Flight Center [52]
NASA JPL .....	(NASA) Jet Propulsion Laboratory [24]
NCAR .....	National Center for Atmospheric Research [34]
NCAR FTS .....	NCAR FOURIER Transform Spectrometer [46]
NDACC .....	Network for the Detection of Atmospheric Composition Change [39]
NOAA .....	National Oceanic and Atmospheric Administration [14]
NOAA/AL .....	(NOAA) Aeronomy Laboratory [25]

- 
- NOAA/CMDL .. (NOAA) Climate Monitoring and Diagnostics Laboratory [25]
- NOAA/ESRL ... (NOAA) Earth System Research Laboratory [14]
- NOAA/ESRL CSD (NOAA/ESRL) Chemical Sciences Division [25]
- NOAA/ESRL GMD (NOAA/ESRL) Global Monitoring Division [14]
- NRL ..... Naval Research Laboratory [14]
- OEM ..... optimal estimation method [72]
- OSIRIS ..... Optical Spectrograph and Infrared Imager System [49]
- PLM ..... path length modulator [63]
- POAM ..... Polar Ozone and Aerosol Measurement [38]
- PREMIER ..... Process Exploration through Measurements of Infrared and Millimeter-wave Emitted Radiation [43]
- PSC ..... polar stratospheric clouds [2]
- PWV ..... precipitable water vapour [9]
- QBO ..... quasi-biennial oscillation [15]
- QCL ..... quantum cascade lasers [36]
- RH ..... relative humidity [19]
- RJ ..... RAYLEIGH-JEANS [60]
- RSD ..... Remote Sensing Division, NRL [40]
- SAFIRE-A ..... Spectroscopy of the Atmosphere by Using Far-Infrared Emission — Airborne [46]
- SAGE ..... Stratospheric Aerosol and Gas Experiment [38]
- SAW ..... surface acoustic wave [24]
- SCIAMACHY ... Scanning Imaging Absorption Spectrometer for Atmospheric Chartography [50]
- SCOUT-O3 ..... Stratosphere-Climate Links with Emphasis on the UTLS [43]
- SDLA ..... *Spectromètre à Diodes Laser Accordables*, [French] tunable diode laser spectrometer [35]
- SMR ..... Sub-Millimetre Radiometer [42]
- SRL ..... Scanning RAMAN Lidar [52]
- SST ..... sea surface temperature [15]
- STE ..... stratosphere-troposphere exchange [43]
- STEAM ..... Stratosphere Troposphere Exchange and Climate Monitor [43]
- SWARA ..... Stratospheric Water Vapour Radiometer [40]

---

TDL	.....	tunable diode lasers [28]
TELIS	.....	Terahertz Limb Sounder [43]
TTL	.....	tropical (tropopause) transition layer [6]
UARS	.....	Upper Atmospheric Research Satellite [42]
ULA	.....	<i>Universidad de Los Andes</i> [3]
UT/LS	.....	upper troposphere/lower stratosphere [17]
UV	.....	ultraviolet [7]
VMR	.....	volume mixing ratio [9]
VSMOW	.....	Vienna Standard Mean Ocean Water [11]
VSWR	.....	voltage standing wave ratio [63]
VUV	.....	vacuum ultraviolet [28]
WaRAM	.....	<i>Wasserdampf-Radiometer für atmosphärische Messungen</i> , [German] Water Vapour Radiometer for Atmospheric Measurements [40]
WASPAM	.....	<i>Wasser- und Spurengasmessung in der Atmosphäre mit Mikrowellen</i> , [German] Microwave Measurements of Water and Trace Gases in the Atmosphere [40]
WMS	.....	wavelength modulation spectroscopy [32]
WVMS	.....	Water Vapor Millimeter-wave Spectrometer [40]

# 1 Introduction

Earth's atmosphere is mainly composed of molecular nitrogen, oxygen, and argon, which together account for more than 99% of the constituents. Yet the less abundant species, so-called trace gases, are of particular scientific concern, since they govern processes of crucial importance to climate and life on Earth. Despite rare coverage in the public media, water vapour plays a key role in atmospheric processes. In the troposphere, it substantially contributes to heat transfer due to the large latent heat in its phase transitions, which readily occur in the atmospheric temperature range. The yearly amount of precipitation is about 40 times the total atmospheric water content, so its average residence time is about 9 days. This makes for the very turbulent dynamics throughout the troposphere.

Earth's overall radiative balance is driven by the dependence of atmospheric optical properties on wavelength: Part of the incoming shortwave (ultraviolet/visible/near infrared) solar radiation is absorbed before reaching the ground, whereas longwave (infrared) absorbers stop part of Earth's thermal emission escaping to space. Water vapour constitutes the largest gaseous source of infrared opacity in the atmosphere. Warming due to an increase in CO<sub>2</sub> results in a positive feedback by water vapour, since higher surface temperatures cause larger evaporation. At the same time, a higher abundance of water vapour may result in a larger fraction of cloud cover. Low-altitude stratus clouds reflect incoming shortwave radiation and thus promote net cooling. High-altitude cirrus clouds on the other hand mostly comprise ice crystals, which transmit shortwave but trap longwave radiation, resulting in a possible warming. In addition, clouds adhere to complex microphysics and involve rapid time scales and short length scales, all of which is hard to model. Hence the tropospheric response to changes in water vapour is difficult to discern.

Water vapour enters the stratosphere by ascent through the tropical tropo-

pause transition layer and by extratropical horizontal transport on isentropic surfaces. Throughout the stratosphere, additional water vapour is produced by methane oxidation, and no sinks exist. This makes for an increase in water vapour abundance with altitude, up to the stratopause. Water vapour accounts for some direct radiative cooling of the stratosphere; however the major cooling effects are induced by decreased ozone and increased trapping of infrared radiation in the lower atmosphere. Regarding stratospheric chemistry, water vapour provides the highly reactive OH radical, which directly contributes to stratospheric ozone destruction by catalytic cycles. Furthermore, it contributes to the formation of polar stratospheric clouds (PSC). During polar spring, PSC play a key role in heterogeneous chlorine chemistry, which effects the large-scale catalytic ozone destruction known as the ozone hole. Given its long chemical lifetime, water vapour is a good tracer for dynamical processes in the stratosphere. In particular, the seasonal cycle in water vapour entering the lower stratosphere is “imprinted” in the air as it ascends in the BREWER-DOBSON circulation; this is known as the atmospheric tape recorder.

Numerous studies report an increasing trend in stratospheric water vapour of the order of  $\sim 0.045 \text{ ppmv yr}^{-1}$  during the second half of the 20th century. Yet in the beginning, the data pool has been sparse, and discrepancies remain with respect to data from the 1980s onwards, when more observations become available. At the turn of the century, a sudden drop is observed, and since then, stratospheric water vapour seems to remain almost constant. There is no satisfactory scientific understanding of these effects, and they underline the importance of continuous monitoring, especially at tropical latitudes, where most of the transport into the stratosphere takes place.

This thesis deals with the operation of a ground-based microwave radiometer/spectrometer, WaRAM2, for the observation of middle atmospheric water vapour at Mérida Atmospheric Research Station (MARS). The sensor records thermal emission at 22 GHz. The vertical resolution of microwave observations is, in general, limited to about 8 km at best, but they deliver very good horizontal resolution with good long-term stability. The WaRAM2 sensor has been built in-house at *Institut für Umweltphysik, Universität Bremen*. The antenna and ellipsoidal mirror have been manufactured by Radiometer Physics GmbH (Meckenheim, Germany).

The initiative for MARS has been sparked by the interest in tropical ob-

---

servations for the validation of Envisat/SCIAMACHY, and ultimately in setting up a tropical primary station within the Network for the Detection of Atmospheric Composition Change (NDACC)<sup>1</sup>. The station is located on top of Pico Espejo in the Venezuelan Andes and is operated by the *Universidad de Los Andes* (ULA), Mérida, which has entered a partnership with *Forschungszentrum Karlsruhe* and the *Universität Bremen*. The site is accessible by the world's longest and highest cable car, Teleférico de Mérida. This location is particularly well suited to microwave observations, due to the reduced shielding of middle atmospheric signals by tropospheric water vapour. Regular observations at MARS started in 2004.

This thesis is structured as follows. Chapter 2 discusses some basic properties of the atmosphere, focussing on stratospheric water vapour. Building on this introduction to the problem at hand, chapter 3 extensively reviews various methods to infer water vapour abundance. It serves as a reference to appreciate the advantages and shortcomings of the individual techniques and their evolution with time. Observations by microwave radiometry/spectrometry form the main part of this thesis. Hence chapter 4 gives more detail about atmospheric radiative transfer in the microwave range, receiver set-up, data processing, and retrieval of geophysical parameters from the data. Chapter 5 subsequently presents the results of observations carried out in 2007. This includes instrument characterisation and a numerical experiment to explore the sensor's sensitivity limit. The report ends in a time-series of tropical stratospheric water vapour from WaRAM2 data and a comparison to correlative data from Aura/MLS. Chapter 6 sums up the key findings.

---

<sup>1</sup> The NDACC maintains a web site at <http://www.ndsc.ncep.noaa.gov/>.



## 2 Water Vapour in the Atmosphere

This chapter is dedicated to introducing in short the structure and dynamics of Earth's atmosphere. Special emphasis is put on stratospheric water vapour, and some of its chemical and radiative effects are discussed. Some of the standard expressions that deal with humidity are introduced in the appendix for reference. Unless stated otherwise, the discussion is based on BRASSEUR et al. (1999) and ROEDEL (2000).

### 2.1 Basic Structure of the Atmosphere

Two basic parameters about the structure of the atmosphere are the dependencies of pressure,  $p$ , and temperature,  $T$ , from altitude above ground,  $z$ . The former is directly related to the weight of air parcels in Earth's gravity field,  $dp/dz = -\rho g$ . When assuming air to be an ideal gas, and neglecting temperature variability throughout the atmosphere, this may be directly integrated to yield the barometric formula,

$$p(z) = p_0 \cdot \exp\left(-\frac{M_{air} g}{RT} \cdot (z - z_0)\right).$$

where  $p_0$  denotes pressure at height  $z_0$ ,  $M_{air} = 2.9 \cdot 10^{-2} \text{ kg mol}^{-1}$  mean molar mass of dry air,  $g = 9.8 \text{ ms}^{-2}$  gravitational acceleration, and  $R = 8.3 \text{ J mol}^{-1} \text{ K}^{-1}$  universal gas constant. Pressure exponentially decays with altitude, at a rate of approximately a decade every 16 km. In wet air, the decay is a little slower with altitude, because the molar mass of water is less than for air. Close to the ground, where water vapour is most abundant, this accounts for 1% of the mean molar mass.

Several processes, like adiabatic changes, radiative effects, and solar irradiance, govern the temperature structure. The magnitudes of these processes vary with altitude, hence so do the characteristic properties of Earth's atmo-

sphere, like the temperature gradient. Ground temperature and water vapour evaporation form important boundary conditions. A general idea of the tropical temperature profile is given in figure 2.1.

According to its characteristics, the atmosphere can be divided into several layers. The lowermost layer, called troposphere<sup>1</sup>, is dominated by heating from Earth’s surface, resulting in strong convection. Air is cooled adiabatically as it lifts up, which determines the negative temperature gradient. The decrease in temperature for dry air, called dry adiabatic lapse rate, is about  $10\text{Kkm}^{-1}$ . Since water vapour saturation pressure depends exponentially on temperature, moist air usually reaches saturation during uplift. This causes liquid or frozen water to form, and the release of latent heat in these phase transitions causes the moist adiabatic lapse rate to be less than the dry rate. Its exact value depends on air moisture content and ranges from  $3\text{Kkm}^{-1}$  (hot and wet) to  $10\text{Kkm}^{-1}$  (cool and almost dry). At tropical latitudes, the atmospheric transition from tropospheric to stratospheric characteristics is a gradual process. This is expressed by the notion of a tropical (tropopause) transition layer (TTL) that extends between roughly 11 – 18 km.

The stratosphere<sup>2</sup> is situated above the troposphere and extends to about

1 “sphere of change”, related to *τρόπος* (*tropos*), [Greek] turn

2 “layered sphere”, related to *stratus*, [Latin] (horizontal) layer

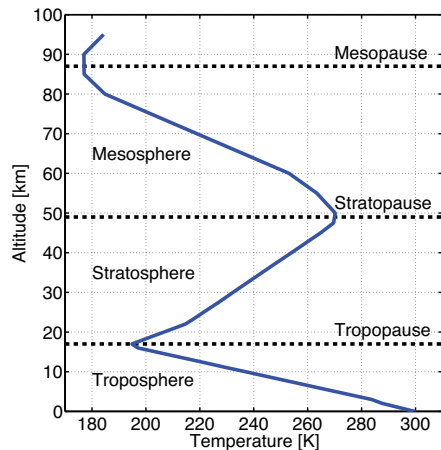


Figure 2.1: Temperature profile according to the FASCOD tropical atmospheric scenario (ANDERSON et al., 1986). Atmospheric layers are indicated.

50 km altitude. It is governed by equilibrium between absorption of ultraviolet (UV) solar radiation, which results in heating, and radiative cooling at infrared (IR) wavelengths. Solar UV radiation is mainly absorbed by ozone, and its heating effect increases with altitude. This introduces a positive gradient in temperature, and air masses are overall stably stratified. The dynamics that still exist in this layer are discussed below.

After heating attains its maximum, at about 50 km, the temperature gradient is again reversed. This marks the lower bottom of the mesosphere, which extends to about 85 km upwards. This layer is of particular interest at polar latitudes, since the high level of UV radiation leads to formation of radicals, which may be transported into the stratosphere by large-scale subsidence during the polar night.

The discovery of atmospheric layering is one of the most surprising findings in the history of meteorology. First records of temperature ceasing to decrease at what now is known the tropopause date back to 1894, carried out by ASSMANN. Allegedly after meeting ASSMANN in 1896, TEISSERENC DE BORT starts a series of balloon soundings, yielding similar results (DUBOIS, 1955, after (LABITZKE, 1998)). Both initially put their revolutionary findings down to measurement error. While TEISSERENC DE BORT optimises his instruments in several ways before eventually trusting in his data, ASSMANN and colleagues make many endeavours to confirm the measurements in a manned balloon flight, which eventually took place in 1901. Both individually publish their findings in spring 1902, within a couple of days. This fosters similar discoveries of ocean layering and solid Earth layering, and motivated WEGENER to propose the theory of continental drift (GREENE, 2000). Yet attribution of the original discovery is controversial: DUBOIS (1955, after (LABITZKE, 1998), see also (MBL, 2008)) reports the publications in 1902 to be a joint announcement founded on scientific cooperation and agreement. On the other hand, the Encyclopædia Britannica solely attributes the discovery to TEISSERENC DE BORT, and GREENE (2000) even presumes that ASSMANN chose to publish his data only after learning that TEISSERENC DE BORT did so. This need not be decided upon here.

Depending on context, the height coordinate in an atmospheric scenario

may conveniently be expressed as potential temperature,  $\theta$ ,

$$\theta = T \cdot \left( \frac{p_0}{p} \right)^\kappa, \quad \kappa = \frac{R}{M_{air} c_p}.$$

$T$  denotes temperature of a given air parcel that originates at pressure  $p$ , and  $c_p$  specific heat of air at fixed pressure (other constants like above).  $\theta$  indicates the temperature that the air parcel would attain if it were moved adiabatically to the reference pressure  $p_0$ . Thus adiabatic processes by definition occur on levels of constant  $\theta$ , called isentropes.

## 2.2 Stratospheric Dynamics

If radiative processes from within were the only force on the stratosphere, it would almost remain in equilibrium. BREWER (1949) has been the first to observe contradicting evidence, in terms of a steep decrease in mid-latitude water vapour just above the tropopause. This has brought about the idea of global circulation, nowadays known as BREWER-DOBSON circulation, in which air enters the stratosphere through the tropical tropopause – only there temperatures are sufficiently low to provide the observed degree of dehydration. Afterwards, air travels pole-wards and eventually returns to the tropopause. It has initially been thought that such circulation could be forced by radiative cooling of the winter hemisphere, which is less exposed to solar irradiation. However, CORIOLIS force effectively cancels any such circulation by eastward deflection. Also, air must lose angular momentum as it moves pole-ward. Instead propagating atmospheric waves, which transfer energy and angular momentum from the troposphere to higher altitudes, drive the global circulation (HOLTON et al., 1995). While the deposited energy may simply be radiated away, the angular momentum influx is balanced by forcing of meridional flow. This description is summarised by figure 2.2. (ROSCOE, 2006; SHEPHERD, 2007)

## 2.3 Stratospheric Water Vapour

Atmospheric water vapour content is closely related to temperature at the ground. This is because saturation pressure, as mentioned above, depends

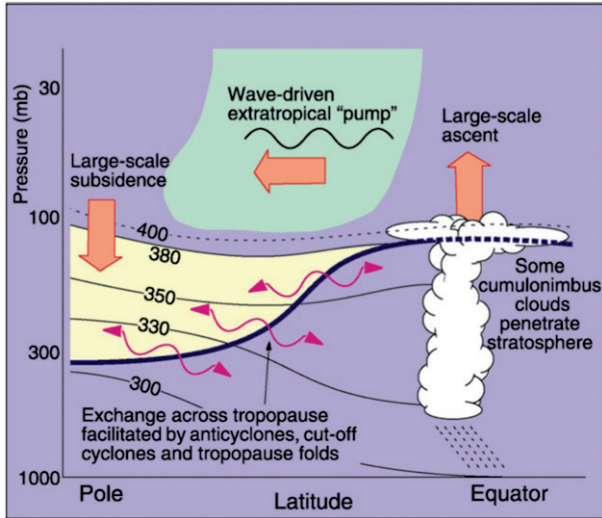


Figure 2.2: Aspects of stratospheric dynamics. The thick blue line indicates the tropopause. The green shaded area denotes the region of forcing by atmospheric waves, broad orange arrows describe the direction of global circulation. The yellow shaded area marks the region where direct stratosphere-troposphere exchange may occur on isentropes (labels denote potential temperatures  $\theta$  [K]). Taken from ROSCOE (2006).

exponentially on temperature. In equatorial regions it can reach up to 60 mm precipitable water vapour (PWV) (*cf.* section A), whereas in cold polar regions, its largest abundance is less than a tenth of this value. Starting from these values, the vertical gradient of water vapour in the troposphere is governed by the decrease in saturation pressure. Figure 2.3 displays a typical water vapour profile according to the FASCOD tropical atmospheric scenario. At sea level, water vapour amounts to 2.6 Vol.-% volume mixing ratio (VMR). As temperature decreases, most of this condenses or deposits, and stratospheric entry values are 2 – 3 ppmv. Stratospheric water vapour accounts for less than 1% of its overall atmospheric content. Yet still it exerts a major influence on stratospheric chemistry and dynamics and feeds back to climate processes at the ground, which is discussed in section 2.4 below.

In addition to transport, water vapour is produced in the stratosphere by oxidation of methane. This reaction is responsible for the increase in water vapour above 20 km that can be read from figure 2.3. Methane is discharged

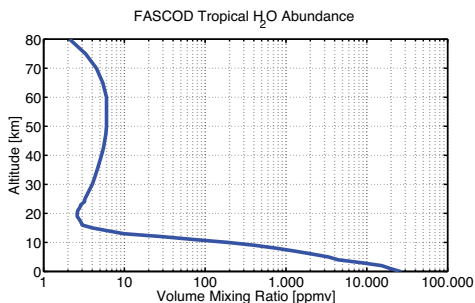
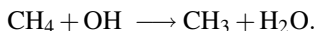


Figure 2.3: Water vapour profile according to the FASCOD tropical atmospheric scenario (ANDERSON et al., 1986).

from the biosphere and marks the only organic compound long-lived enough ( $\sim 10$  years) to be transported to the stratosphere in significant amounts. The most important source for methane is release from geological deposits, natural gas fields, where it has been formed by anaerobic decay of organic matter. Human-induced sources, like exhaust from the warm and waterlogged soil of rice crop growing, industrial livestock farming, and fermentation of organic rubbish, have become increasingly important. Methane concentration has nearly tripled since pre-industrial times. Its growth rate appears to recently have come to stand still (BOUSQUET et al., 2006), but thawing of Siberian permafrost soil holds potential for a massive release of methane into the atmosphere (SEMILETOV et al., 2008).

Given its long atmospheric lifetime, methane is well mixed throughout the troposphere at a level of currently about 1.8 ppmv. The same level of methane is accordingly observed to enter the stratosphere from the TTL. Throughout most of the stratosphere, destruction of methane is dominated by reaction with hydroxyl radicals (LE TEXIER et al., 1988),



In addition, there are several reactions of methane with excited atomic oxygen that eventually result in the production of water. The total yield is close to 2 molecules of water per molecule of methane. No other sources of water vapour exist throughout the stratosphere, and satellite observations indicate that “total hydrogen”, defined as  $2 \cdot [\text{CH}_4] + [\text{H}_2\text{O}]$ , is relatively constant in this region.

Higher up into the mesosphere, water vapour is increasingly photolysed by solar irradiation around LYMAN- $\alpha$  wavelength and the SCHUMANN-RUNGE bands. Yet localised maxima are observed at 65 – 75 km during po-

lar summer and tropical equinox, and another at higher altitudes only during polar summer, which are discussed e.g. by SONNEMANN et al. (2005, 2008), respectively.

Observations based on a new generation of sensors (*cf.* sections 3.1.6-3.1.7) have recently hardened the case for a third route of significant water entry to the stratosphere, which is by convective ice lofting. Due to the localised nature of such events, their importance for the total stratospheric water vapour budget remains an open question. The rate of ice entry to the stratosphere may be inferred from measurements of water isotopologue separation,  $\delta D$ ,

$$\delta D = 1000\%_0 \cdot \left( \frac{[HDO]/[H_2O]}{2R_{VSMOW}(D/H)} - 1 \right), \quad (2.1)$$

$R_{VSMOW}(D/H) = 155.76 \pm 0.1$  ppm being the isotopic ratio for Vienna Standard Mean Ocean Water (VSMOW)<sup>3</sup>. Slowly ascending air exhibits a depression in HDO, because this so-called semiheavy water preferentially condenses from the gas phase. Consequently, if water is convectively injected to the stratosphere, it is less depleted in HDO. Consideration of ice lofting much improved the simulation of  $\delta D$  in the Lagrangian model of stratospheric water vapour entry levels discussed below. (DESSLER et al., 2007)

### 2.3.1 Dryness of the (Lower) Stratosphere

As introduced in section 2.2, the aridity of the stratosphere results from what is now known as the BREWER-DOBSON circulation. Air predominantly enters the stratosphere by passing the TTL, and is then distributed throughout in an upward-pole-ward-downward motion. Temperature within the TTL reaches below 200K, which effectively “freeze-dries” the bypassing air to water vapour levels that are consistent with stratospheric observations.

The temperature of the TTL is subject to an annual cycle that yields lowest values during boreal winter. The cause of this cycle remains an open

---

3 VSMOW is the standard reference for the isotope ratios of H and O in purified water. It is maintained and prepared by the International Atomic Energy Agency (IAEA), Vienna, Austria, which sends out small portions of VSMOW to laboratories for calibration. The almost exhausted VSMOW has recently been replaced by a successor called VSMOW2, which reproduces the isotopic composition of VSMOW well within uncertainties of field laboratory measurements. (IAEA, 2008)

question, yet it modulates the degree of dehydration that occurs in the TTL. This signal is imprinted on air that ascends into the stratosphere, as if it were recorded on magnetic tape (figure 2.3.1). For this reason it has been termed the atmospheric “tape recorder” (MOTE et al., 1996). One benefit of this clear signal is that it allows quantifying the magnitude of upward motion in the stratospheric BREWER-DOBSON circulation. It has also resolved a long-standing puzzle about the so-called hygropause, a region of minimum water vapour abundance that is observed above the tropopause (KLEY et al., 1979): The hygropause merely marks the upward propagation of the annual minimum in water vapour entering the stratosphere.

Despite the qualitative picture being correct, water vapour volume mixing ratio upon entry to the stratosphere,  $[\text{H}_2\text{O}]_e$ , is over-estimated when calculated in Eulerian coordinates<sup>4</sup>; annual and zonal mean temperatures of the TTL are too high to agree with observed stratospheric water vapour. FUEGLISTALER et al. (2005) instead calculate  $[\text{H}_2\text{O}]_e$  from a Lagrangian model, based on ECMWF<sup>5</sup> re-analysis (ERA-40) wind and temperature data. They infer that trajectories entering the stratosphere from the TTL mainly

4 In fluid mechanics, Eulerian coordinates denote the study of flow at a fixed point of reference.

Lagrangian coordinates instead consider flow by following motion of fluid particles.

5 European Centre for Medium-Range Weather Forecasts

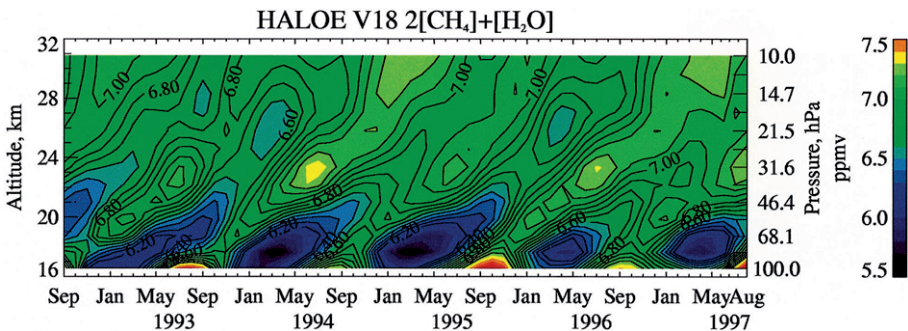


Figure 2.4: Total water ( $2 \cdot [\text{CH}_4] + [\text{H}_2\text{O}]$ ) volume mixing ratio from HALOE observations, zonal average over the latitude band  $12^\circ\text{N}$ – $12^\circ\text{S}$ . The data clearly indicate upward propagation of an annual cycle in dehydration, caused by a corresponding cycle in TTL temperature. Taken from SHEPHERD (2000, originally from MOTE et al.).

travel a region over the western Pacific ( $\sim 100^\circ\text{W}$ – $150^\circ\text{E}$ ), which exhibits a global minimum in tropopause temperatures. During boreal summer, the Indian monsoon system is identified to be an additional region of similar importance. To compare the model data to observations, trajectories that originate in the stratosphere must also be taken into account. This is illustrated by figure 2.5. Between 1979–2001, mean  $[\text{H}_2\text{O}]_e$  from the model amounts to about 3.5 ppmv, and the amplitude of the annual variation in  $[\text{H}_2\text{O}]_{\text{T}400}$ , water vapour volume mixing ratio at  $\theta = 400\text{ K}$ , is about 1.7 ppmv, in good agreement with observations.

### 2.3.2 Trends (Past and Future)

There is some evidence for a sustained increase in stratospheric water vapour, about  $1\% \text{ yr}^{-1}$  ( $\sim 0.05 \text{ ppmv yr}^{-1}$ ), from 1980 to roughly 2000. Since then, observations are constant or indicate a decrease, depending on altitude (IPCC, 2007). However, the longest time-series of data have been obtained from balloon soundings at just two northern mid-latitude sites, with no temporal

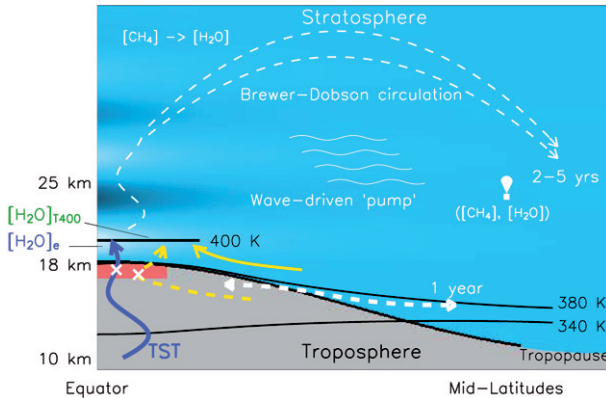


Figure 2.5: Trajectories of air that determine stratospheric water vapour VMR at  $\theta = 400\text{ K}$ ,  $[\text{H}_2\text{O}]_{\text{T}400}$ . The blue arrow indicates trajectories that account for entry into the stratopause,  $[\text{H}_2\text{O}]_e$ . The red area indicates where air travelling along these trajectories is reduced to its final water vapour VMR (called the Lagrangian cold point, shown as white crosses). Blue shading symbolises the atmospheric tape recorder. Taken from FUEGLISTALER et al. (2005).

overlap (NRL<sup>6</sup> and NOAA<sup>7</sup>/ESRL<sup>8</sup> GMD<sup>9</sup> frost point hygrometer, *cf.* section 3.1.4), so the observations must be handled cautiously with respect to changes on decadal time scales. SCHERER et al. (2008) present trend estimates from a reanalysis of the 1980–2000 data, which are 10–40% lower than previously reported, the correction being largest at highest altitudes. Around 2000/2001, several observations indicate a pronounced drop in stratospheric water vapour, which is consistent with an unusually cold anomaly in TTL temperature (RANDEL et al., 2006).

The reasons for the observed trend in stratospheric water vapour are all but well established. Increased methane levels may account for a third of the  $1\% \text{ yr}^{-1}$  trend. A variety of mechanisms are considered to completely account for the observations, e.g. increased  $\text{SO}_2$  levels from anthropogenic emissions, which result in formation of smaller ice crystals that are more readily lifted into the stratosphere (NOTHOLT et al., 2005). It is likely that different mechanisms are at play at different altitudes (IPCC, 2007).

If the observed trend were due to a rise in  $[\text{H}_2\text{O}]_e$ , temperatures around the tropical tropopause should have increased during 1960–2000. Observations however indicate a slight cooling, adding further obscurity to the matter. On the other hand, the trend data, having been won from mid-latitude measurements, so far do not allow inferring quantitative constraints on a possible change in  $[\text{H}_2\text{O}]_e$  neither. The combined uncertainties in the observations and in the wind and temperature data are too large (SCHERER et al., 2008).

## 2.4 Effects on Climate

Stratospheric processes have pronounced effects on Earth's climate. Albeit only abundant in trace amounts, stratospheric ozone, water vapour, and carbon dioxide exert significant radiative forcing. Perturbations in stratospheric dynamics propagate downwards to affect surface weather and climate. Some of these effects are introduced in short here.

Stratospheric water vapour acts as source gas for production of the highly

---

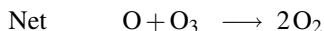
6 Naval Research Laboratory

7 National Oceanic and Atmospheric Administration

8 (NOAA) Earth System Research Laboratory

9 (NOAA/ESRL) Global Monitoring Division

reactive OH radical which is directly involved in catalytic ozone destruction, prevalently at 30 – 40km. Catalytic schemes essentially speed up the reactions that destroy odd oxygen in CHAPMAN's original scheme, like



A more detailed description of the reactions involved is given for example by WAYNE (2000). Additionally, increased levels of stratospheric water vapour indirectly contribute to ozone destruction by easier formation of polar stratospheric clouds (HINTSA et al., 1999). This is both through better availability of water and through lower temperatures, caused by water vapour radiative cooling.

Climate effects also stretch across atmospheric layers, and include the oceans: ROSENLOF and REID (2008) report on lower stratospheric temperatures above the western Pacific being significantly anti-correlated with sea surface temperature (SST) of the underlying ocean. The connection is almost simultaneous and is present on the scale of individual monthly anomalies. They suggest that this connection could be moderated by intensified deep convection in the troposphere, as introduced by higher SST. Modifications in cloud cover, and consequently in outgoing longwave radiation, would be another possible explanation. The data correspond well with the significant drop in stratospheric water vapour found around 2000/2001.

There is indication from modelled scenarios that the global meridional circulation will accelerate in response to global warming. Changes in stratospheric dynamics in turn affect the propagation of atmospheric waves. The stratosphere thus exerts a feedback to ground weather and climate, in particular at higher latitudes. For example, cold anomalies in northern hemispheric winter exhibit some correlation to the phase of the quasi-biennial oscillation (QBO). The exact mechanisms of such correlations remain to be established, but will form an important part of future climate modelling (BALDWIN et al., 2007).



### 3 Water Vapour Observation Techniques

A large number of techniques exist to measure water vapour from various platforms, *in situ* and by remote sensing. This is due to both the importance of water vapour in atmospheric processes and the experimental challenges that are involved in its observation. These intricacies have motivated the pursuit of a comprehensive assessment of upper tropospheric and stratospheric water vapour observations at the turn of the century (KLEY et al., 2000). Significant uncertainties remain, and have recently sparked an initiative to sum up new results over the past decade (SCHILLER et al., 2008).

The major focus are measurements in the upper troposphere/lower stratosphere (UT/LS), because in this region, water vapour exerts large dynamic and radiative effects, and its transport into the stratosphere is determined. Both are critical parameters in future climate modelling. The UT/LS also is a region of very sparse measurements, which is due to the challenging thermodynamic conditions there. In addition, even the most sophisticated scientific instrumentation may easily suffer from dry biases because of the difficulty to access areas of deep convection. Further demand for detailed and accurate measurements in the UT/LS has been created by the surprising observation of pronounced supersaturations with respect to ice (PETER et al., 2006). At the same time, the discrepancies between various sensors are so large that the interpretation of microphysical processes may change by choice of the observational data on which it is based (e.g. VÖMEL et al., 2007a). For this reason, an extensive laboratory intercomparison effort has been carried out at the unique AIDA<sup>1</sup> facility of FZ Karlsruhe<sup>2</sup>, Germany, in 2007<sup>3</sup>. The laboratory allows emulating all temperature, pressure and water vapour levels that are found up to the lower stratosphere. Campaign results

---

1 Aerosol Interactions and Dynamics in the Atmosphere

2 Forschungszentrum Karlsruhe

3 cf. <http://imk-aida.fzk.de/campaigns/RH01/Water-Intercomparison-www.htm>

have not yet appeared in peer-reviewed literature, but WEINSTOCK et al. (2008) indicate that the sensor discrepancies could not be reproduced in the laboratory set-up, so it must be further refined to match in-flight conditions.

The outlined issues limit our capacity to discern the parameters that control water vapour entering to the stratosphere, which is required to model future trends in the stratospheric water vapour budget. Observations of stratospheric water vapour are found to reasonably agree, the majority of sensors clustering within 10% ( $\sim 0.2 - 0.7$  ppmv) of each other (KLEY et al., 2000). Measurements are instead challenged by the smallness in stratospheric variability, which in turn necessitates changes of the order of a few tenths of 1 ppmv to be resolved. Accurate long-term monitoring forms a key requirement for our ability to detect and attribute trends in stratospheric water vapour abundance.

In light of these sobering remarks, this chapter aims to give an orientation about the various techniques for water vapour observation, and their individual benefits and shortcomings. The discussion covers a representative portion of sensors for the individual methods, while mostly maintaining focus on stratospheric applications. Furthermore, with respect to remote sensing methods, it is mostly restricted to sensors in current operation for tropical stratospheric measurements.

### 3.1 *In Situ* Methods

*In situ* measurements are of great importance for the study of rapid and small-scale processes that occur in water vapour, in particular with respect to clouds. They also contribute considerably to the validation of remote sensors, in particular space-borne, but are restricted in spatial and temporal coverage, due to the cost and limited availability of aircraft, balloon, and (rarely) rocket platforms. New instrumentation has been inspired by the interest in the water vapour isotopologue separation, cf. equation (2.1). First results from Hoxotope and the Harvard ICOS instrument, both introduced below, show much promise for the analysis of water vapour entry routes into the stratosphere.

The most pressing task remains to resolve the large disagreement between results from various sensors, yet progress has been small. To illus-

trate this, three quotes are given below from publications that also appear in sections 3.1.6, 3.1.4, and 2.3.2, respectively.

The reason for these striking discrepancies is still unknown, whether they are caused by instrumental or sampling artefacts. (...) The improvement of the accuracy of H<sub>2</sub>O measurements hence has to be a major issue of future activities. (ZÖGER et al., 1999)

Disagreements between aircraft borne instruments and balloon borne instruments have been reported in the past (...), and the comparison presented here reinforces the need to address this issue in more detail. (VÖMEL et al., 2007a)

A reliable quantification of trends in [H<sub>2</sub>O]<sub>e</sub> from the NOAA FP and HALOE middle latitude measurements due to processes not considered by Fueglistaler and Haynes (2005) is currently not possible due to the large difference between the residual to NOAA FP and to HALOE data. (...) Our analysis demonstrates the need for ongoing efforts to obtain long and continuous time series of stratospheric water vapour. (SCHERER et al., 2008)

### 3.1.1 Absorption Hygrometers

Many kinds of material vary in apparent physical properties, like weight or extent, according to their moisture content. This feature allows defining a very basic measure of humidity if one lets the material exchange moisture with surrounding air and thus attain equilibrium with local water vapour abundance. The observable properties vary with relative humidity (RH) rather than absolute humidity. This seems quite surprising, considering the large range of total moisture that corresponds to any fixed value of RH, dependent on temperature (HÄCKEL, 2005). The reasons why hydroactive material responds to RH do not find much attention. A simple model is given by ANDERSON (1995).

The most basic variant of absorption hygrometers is based on the elongation of hair as it gets wet, first utilised in an apparatus built by Swiss physicist HORACE BÉNÉDICT DE SAUSSURE in 1783 (Britannica, 2008Britannica). Most commonly, the elongation of the hair is passed on by a system of levers to some kind of dial, from which RH may be read. Hair has the advantage that it does not change length with temperature, it is however subject to ageing and sensitive to radiation. It is nowadays replaced by synthetic fibre, but the apparatus itself remains in widespread use given the sheer ease of its construction.

The vast majority of today's humidity observations by radiosondes rely on the dependence of electrical properties on absorbed moisture. At the time of this writing, 913 stations world-wide operate daily standard soundings of upper air parameters, of which roughly half deploy the HUMICAP type of sensors by Vaisala corporation, Finland (evaluated from OAKLEY, 2008). These comprise a thin polymer film capacitance whose permittivity changes with ambient RH. Other sensor types deploy carbon-based resistive elements. Standard soundings also require temperature and pressure to be recorded, but of these three, humidity observations are clearly the most difficult to obtain.

The performance of all hydroactive materials discussed here is critically dependent on the rate of exchange of water molecules with air. Low water vapour abundance, as caused by cold temperatures in the upper troposphere, hence limits the quality of radiosonde upper-tropospheric humidity data. For daytime soundings, heating of the sensor by solar irradiation needs to be corrected for. The presence of time lags in sensor response poses further challenge to the data user. A recent study related to validation of AIRS<sup>4</sup> on board the Aqua satellite indicates that measurements by Vaisala radiosondes are reasonably accurate throughout the troposphere when corrected for above error sources. Vaisala reports the accuracy and precision of the RS92 radiosonde as 0.5 K/0.2 K for temperature and 5/2 percentage points for RH (Vaisala, 2006). The combined uncertainty in the upper troposphere amounts to roughly 15–20 percentage points in  $RH_{ice}$  ( $\sim 60$  ppmv at 200 hPa) (READ et al., 2007). Other sensors break down at lower altitudes or exhibit severe errors when exposed to clouds, in particular thick ice clouds. (MILOSHEVICH et al., 2006)

Another problem arises from the commercial origin of modern radiosondes, which motivates sensor modifications and calibration procedures be kept business secrets. So any technological advance made in sensor fabrication necessitates further intercomparison efforts to ensure reliability of long-term time series made with different generations of sensors. The type of sensor, calibration procedure, and data corrections need be well documented to make intercomparison of radiosoundings feasible.

The relative ease of RH measurement helped establish its use as a standard

---

4 Atmospheric Infrared Sounder

measure for water vapour abundance. RH is a good indicator for the possibility of evaporation and condensation. Yet the dependence of RH on temperature makes its use rather awkward when absolute water vapour abundance is of interest, as is illustrated by figure 3.1. Due to this dependence, accurate measurement of temperature is fundamental for the use of RH data obtained by absorption hygrometers.

Special care needs to be taken in choosing the appropriate formulation of water vapour saturation pressure with respect to water,  $e_{aq}$ , when comparing RH to absolute abundance of water vapour. This complication is due to the historic practice to always report radiosonde measurements as RH with respect to water, also at temperatures below freezing. It requires extrapolation of  $e_{aq}$  to cold temperatures, where experimental data are difficult or impossible to obtain, since water cannot be supercooled below the homogeneous nucleation temperature ( $\sim 235$  K at sea level pressure). This introduces large disagreement between the various formulations of  $e_{aq}$ . For example at tropical tropopause temperatures, the formulation used by Vaisala deviates by 16% from a more accurate formulation devised by MURPHY and KOOP (2005). Unfortunately, radiosonde measurement protocols rarely disclose the formulation of  $e_{aq}$  that was assumed in sensor calibration. This uncertainty could be overcome if RH were additionally reported with respect to ice. Common formulations of saturation pressure over ice,  $e_{ice}$ , agree well with each other and with laboratory data. Considering the at-

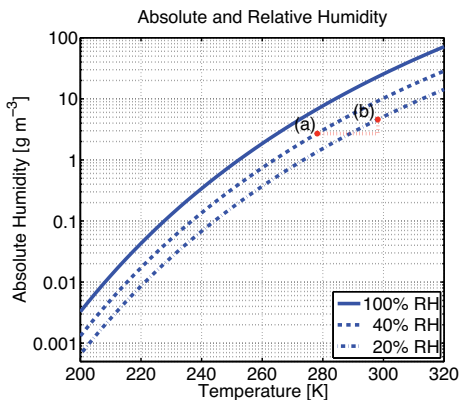


Figure 3.1: The blue curves denote absolute humidity,  $a$ , versus temperature at three different relative humidity levels, 100% RH (solid), 40% RH (dashed), and 20% RH (dash-dotted), according to the water vapour saturation pressure formulation with respect to water by MURPHY and KOOP (2005). The absolute water vapour abundance for a particular value of RH depends almost exponentially on temperature. Consider air with (a) RH = 40% at 5 °C, which translates to  $a = 2.7 \text{ g m}^{-3}$ , and (b) with RH = 20% at 25 °C, i.e.  $a = 4.6 \text{ g m}^{-3}$ : Despite halving RH, absolute humidity in (b) is 70% more than it is in (a).

mospheric temperature range, the largest relative deviations amount to less than 0.5%. (MILOSHEVICH et al., 2006)

### 3.1.2 MOZAIC

MOZAIC I-II<sup>5</sup> and MOZAIC III<sup>6</sup> fly on commercial passenger aircraft, which provides for very cost-effective access to the upper troposphere. The water vapour instrument comprises a HUMICAP-H capacitive element produced by Vaisala, Finland, and a PT100 resistive temperature sensor, both read by a Vaisala control unit. The sampling of air at the sensor introduces noticeable adiabatic heating, which is accounted for in data evaluation. Comparison against a precursor of the FISH photofragment fluorescence hygrometer yielded an accuracy of 10 percentage points RH. (HELTEN et al., 1998)

### 3.1.3 Psychrometers

Relative humidity of ambient air can also be measured based on the effect of evaporation cooling. A psychrometer implements this idea by recording the ambient temperature with two thermometers in parallel, one kept dry, the other covered by a wet cloth. Heat will be taken up by evaporation of water from the wet cloth, and will be released into the cloth by condensation of water vapour. However at RHs below 100%, i.e. when water vapour partial pressure is less than saturation pressure, evaporation prevails over condensation. This yields a lower reading  $T_w$  of the wet thermometer, whose difference to the "dry" temperature  $T_d$  is an indirect measurement of RH as given by SPRUNG's formula,

$$e_p = e_s(T_d) - \gamma \cdot (T_d - T_w).$$

$e_{p,s}$  denote water vapour partial and saturation pressure, the psychrometer constant  $\gamma$  is dependent on atmospheric conditions and can be approximated

<sup>5</sup> Measurements of Ozone and Water Vapour by Airbus In-service Aircraft

<sup>6</sup> Measurements of Ozone, Water Vapour, Carbon Monoxide and Nitrogen Oxides by Airbus In-service Aircraft

as  $0.67 \text{ hPa K}^{-1}$  below 500m altitude. Air must be exchanged around the thermometers rapidly enough to prevent false readings from evaporated water accumulating in the instrument case. To accomplish this, the so-called sling psychrometer needs to be manually whirled around. In balloon-borne applications, the condition has to be met by sufficiently high ascent/descent speed, or through regulating air flow by a ventilator as in the ASSMANN psychrometer. Psychrometers have been deployed for the measurements that led to discovery of the stratosphere at the turn of the twentieth century, but since been replaced in scientific use by more advanced measurement techniques.

### 3.1.4 Dew/Frost Point Hygrometers

Frost point hygrometers differ fundamentally from any other type of instrumentation discussed here in that they directly record the temperature at which water vapour from ambient air starts to deposit, called frost point (temperature)<sup>7</sup>. At higher ambient temperatures, the dew point is determined instead, i.e. the temperature at which condensation sets in. For simplicity, and given tropospheric temperatures commonly below freezing, the following discussion will explicitly refer to frost point only, with both phenomena in mind.

The basic idea in frost point hygrometers is to observe deposition on a surface that is exposed to moist air, as the surface is cooled. This principle appeals for its simplicity and its apparently being independent of other physical properties that are hard to obtain, like absorption cross sections in optical hygrometers. Because of this, frost point hygrometers serve as calibration standards in scientific and national standardisation applications alike. Such reference sensors for laboratory use are commercially available from e.g. MBW Calibration Ltd, Switzerland, or GE Sensing Company, USA.

Frost point hygrometry is first employed in the seventeenth century, when the experimenter filled a vessel with cold water or ice to watch condensation on the outside. Such a set-up has been used by CHARLES LE ROY to

---

<sup>7</sup> Frost point and dew point are denoted by a  $(p, T)$  pair in the phase diagram, so the exact term is frost point temperature. Yet in the present case,  $p$  is fixed to water vapour partial pressure of ambient air,  $e_w$ , so  $T$  at the onset of deposition is commonly called the frost point.

define the dew point in 1851, but it is subject to rather large error (BURNS, 2003). In modern frost point hygrometers, a thin layer of frost is maintained on some type of temperature-regulated surface, typically a mirror. Differential changes of frost layer thickness are recorded by the response of one or more photodetectors to controlled illumination of the mirror. The mirror temperature is accordingly regulated by an electronic feedback loop that is connected to a Peltier element. Alternatively, a thermistor may be used as a heating element, in which case the mirror is fixed to a cold sink to allow full temperature control. This design is favourable because of the lower temperatures it is able to achieve as well as faster response times (OLTMANS et al., 2000; MEZRIN and STAROKOLTSEV, 2001; VÖMEL et al., 2007a). Albeit highly accurate, frost point hygrometers are slow when compared to optical, photofragment fluorescence and tunable diode laser hygrometers (*cf.* sections 3.1.5–3.1.7). This is because, like absorption hygrometers (*cf.* section 3.1.1), they depend on exchange of water with the surrounding air, which is limited at low absolute humidity like found above the tropopause. Promise for a much improved response time lies in the use of surface acoustic wave (SAW) sensors for frost layer analysis instead of optical detectors, as demonstrated e.g. by HOUMMADY et al. (1995). HOENK et al. (2000) at NASA<sup>8</sup> JPL<sup>9</sup> have devised an operational instrument of this kind that has flown on the NASA DC-8 aircraft, but results appear not to have been published in peer-reviewed literature. Same holds true for an instrument developed by HANSFORD et al. (2006), at the University of Cambridge, UK, whose earliest version flew on a balloon in 1999. In the following, some frost point hygrometer implementations with significant scientific impact are shortly discussed.

BREWER (1949) has used a manually operated frost point hygrometer in the discovery of the extreme dryness of the stratosphere. Also the only available multi-decade record of *in situ* soundings has been obtained using frost point hygrometers on balloons. It is started by MASTENBROOK and OLTMANS (1983) at NRL, Washington, DC, in 1969. To avoid systematic errors from outgassing water, measurements are only taken during balloon descent, which is achieved by partially valving helium from the balloon at its

---

<sup>8</sup> National Aeronautics and Space Administration

<sup>9</sup> (NASA) Jet Propulsion Laboratory

ceiling altitude of roughly 28 km. The instrument undergoes electronical re-design in 1977 without precautions for intercomparison. When handed over to NOAA/CMDL<sup>10</sup> (now NOAA/ESRL GMD) at Boulder, CO, in 1980, it is equipped with a different heating system for the mirror and reconfigured to use ram flow through the sensor cavity instead of forced flow. Changes to the instrument calibration set-up are traceable to a US National Institute of Standards and Technology reference and have been intercompared to agree within 0.1 K of each other (OLTMANS et al., 2000). In-flight checks of instrument control, response time and repeatability of the measurement are carried out by periodically raising the mirror temperature above frost point. This procedure remains the same throughout all instrument revisions.

Under stratospheric conditions, the instrument response time is reported to be 20 – 35 s. At balloon descent rates of typically about 5 – 12 ms<sup>-1</sup>, this allows measurements be taken on a 250 m grid (MASTENBROOK and OLTMANS, 1983). The 1977–1979 data, after the first instrument redesign, appear systematically lower than previously and have been excluded from later trend analysis. For earlier Washington, DC measurements, the accuracy is reported as 1 K in frost point temperature, corresponding to 18% (0.75 ppmv) in lower stratospheric volume mixing ratio. For the same data, OLTMANS et al. (2000) later give a precision figure of 0.75 K, equivalent to 15% (0.60 ppmv). For the data subsequently taken at Boulder, they report an improved precision of 0.5 K, or 10% (0.40 ppmv). No accuracy is reported with these latter values.

There exists a frost point hygrometer for operation on the NASA WB-57 high altitude aircraft, which has been constructed at NOAA/AL<sup>11</sup> (now NOAA/ESRL CSD<sup>12</sup>) and used in Aura Validation Experiment campaigns. Instrument operation is however being described as inconsistent, and literature is scarce. (KELLY, 2006; VÖMEL et al., 2007a; READ et al., 2007)

The University of Colorado cryogenic frost point hygrometer (CFH) for balloon is loosely based on the NOAA/ESRL GMD design, however modified to avoid its earlier shortcomings. It is improved in weight, performance and cost by use of digital electronics. It dispenses with mechanical means

---

10 (NOAA) Climate Monitoring and Diagnostics Laboratory

11 (NOAA) Aeronomy Laboratory

12 (NOAA/ESRL) Chemical Sciences Division

to shield sunlight from the detector and thus is significantly less affected by cloud contamination, which occurs through adsorption of water or ice to the instrument's surfaces. Solar influences on the photodetector signal are discriminated by rapid on/off switching of the light source at a rate of 5 kHz. The CFH requires less skill to prepare operation and may descend by parachute rather than valving of the balloon. It solves the ambiguity between dew and frost point by force-freezing the condensate after first reaching a low limit in mirror temperature during ascent ( $-12.5\text{ }^{\circ}\text{C}$ ). To aid against formation of cubic ice crystals (as opposed to the common hexagonal structure), which may pose a problem at very low temperatures,  $T < 200\text{ K}$ , due to a higher saturation vapour pressure, the CFH evaporates the frost layer at 220 K to have it reform immediately as hexagonal ice only. These improvements render the sensor particularly well suited as a campaign instrument, and by consequence it is routinely used at several sites for validation efforts and process studies. The measurement error is of the same order of magnitude as with the last revision of the NOAA/ESRL GMD design, but at a higher data yield and quality. (VÖMEL et al., 2007a,b)

Meteolabor AG, Switzerland, offer a small series production type frost point sensor for balloon named SnowWhite that is used in operational soundings by MeteoSwiss. It provides excellent ease of use at comparably low cost and interfaces well with several kinds of radiosondes, which are needed to provide pressure and air temperature data, and ground communication. SnowWhite results however are somewhat mixed, and measurements are limited to the troposphere because a thermoelectric (Peltier) element is used to control the mirror temperature. This also affects the maximum detectable frost point depression from air temperature, and thus fixes the minimum detected humidity to 3 – 6% RH, which quickly exceeds the order of 1 ppmv when ascending into the stratosphere. Above this limit and in absence of some bias effects, the SnowWhite total accuracy is comparable to the last revision of the NOAA/ESRL GMD design. (VÖMEL et al., 2003; MILOSHEVICH et al., 2006)

### 3.1.5 Optical Hygrometers

Optical hygrometers measure the number density  $N$  of water vapour by direct use of BEER'S law regarding extinction of light in an absorbing substance of length  $l$ ,

$$\ln \left( \frac{I(\lambda)}{I_0(\lambda)} \right) = \alpha_\lambda \cdot l \cdot N \quad (3.1)$$

where  $I_0(\lambda)$  and  $I(\lambda)$  denote intensities before and after the absorber and  $\alpha_\lambda$  is the absorption coefficient at wavelength  $\lambda$ . A typical set-up comprises a lamp covering a spectral region with water vapour absorption features and a suitable photodetector. Added filters may protect the detector from sunlight and, for example, fluorescence effects (ZUBER and WITT, 1987). Despite this simple and easily accessible observation principle, optical hygrometers suffer from competing absorption by molecular oxygen at LYMAN- $\alpha$  wavelength. LYMAN- $\alpha$  radiation was typically used in this application because of lamp availability and the relatively strong water vapour absorption in that region. Figure 3.2 displays the ratio of water vapour to oxygen absorption around LYMAN- $\alpha$  wavelength. The dominance of water vapour absorption at LYMAN- $\alpha$  would in principle allow neglecting the variable contribution of oxygen, dependent on local pressure, to total absorption measurements.

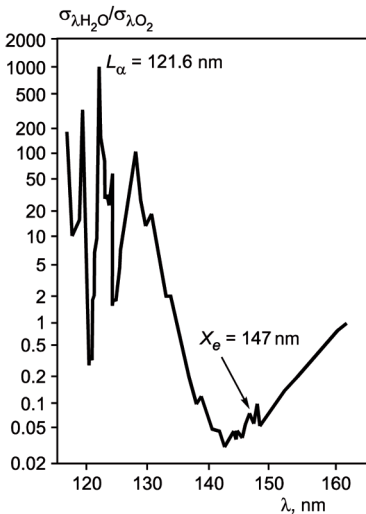


Figure 3.2: Ratio of water vapour to molecular oxygen absorption coefficients  $\sigma_\lambda$  around LYMAN- $\alpha$  wavelength. Taken from (KOZLOV et al., 2005).

This approach is hampered by spectral impurities of the lamps, resulting in non-uniform response of the instrument to water vapour and oxygen concentration. The optical absorption method is significantly promoted by use of other spectral regions, which have become available for *in situ* atmospheric measurements when tunable diode lasers (TDL) evolved into commercial packages. The light source being the key factor in deployment of this method, such instruments are consequently termed tunable diode laser hygrometers (*cf.* section 3.1.7).

### 3.1.6 Photofragment Fluorescence Hygrometers

Photofragment fluorescence hygrometers are based on the observation that polyatomic molecules, when irradiated by vacuum ultraviolet (VUV) radiation<sup>13</sup>, tend to leave behind fragments in electronically excited states.



The quantum yield  $\Phi$  of this reaction depends on the total availability of decomposition pathways for the parent molecule. The excited photofragments relax through spontaneous emission or quenching by other reactants.



Reaction (3.3a) is characterised by its associated decay rate  $\lambda_{h\nu}$ , the equivalent for reaction (3.3b) being the rate coefficients  $k_q^M$  for quenching by reactants M. As KLEY and STONE (1978) demonstrated, reactions (3.2) and (3.3a) allow deducing the reactant's volume mixing ratio in a sample of air. The idea is to expose the sample to e.g. LYMAN- $\alpha$  radiation and then measure the intensity of spontaneous emission from excited photofragments. Such emission may occur at different wavelengths, depending on the vibrational states  $b$ ,  $a$  of the photofragment before and after photon emission. The relative probability of a transition relates to the EINSTEIN coefficients  $A_{b,a}$ , so the expected intensity is given by

$$I_{(b,a)} \propto [XY^*] \cdot A_{b,a}, \quad (3.4)$$

---

<sup>13</sup> VUV radiation owes its name to the fact that it is absorbed by air, i.e. it only propagates in vacuum.

where the number density of photofragments  $[XY^*]$  can be derived from basic principles as

$$[XY^*] = \frac{[XYZ] \cdot J \cdot \Phi}{\lambda_{hv} + \sum_i k_q^{M_i} [M_i]} \quad (3.5)$$

with  $J$ : the photodissociation coefficient for  $XYZ$ .

In water vapour, reaction (3.2) has first been reported by TERENIN and NEUJMIN (1934).



When looking at  $\text{OH}^*$  in air, quenching is dominated by  $\text{N}_2$  and  $\text{O}_2$ , and the summation over quenching rates in equation (3.5) can be substituted by  $k_q^{\text{air}}[\text{air}]$ . In the UT/LS, quenching largely prevails photonic relaxation, so the whole denominator may be reduced to  $k_q^{\text{air}}[\text{air}]$  for illustrative reasons. Due to  $[\text{H}_2\text{O}] \ll [\text{air}]$  we may further approximate  $[\text{H}_2\text{O}]/[\text{air}]$  to be the  $\text{H}_2\text{O}$  volume mixing ratio  $\mu_V$ . Equations (3.4) and (3.5) then yield

$$I \propto \mu_V \cdot J \cdot \Phi$$

So in some atmospheric region, photofragment fluorescence responds almost linearly to  $\text{H}_2\text{O}$  VMR. It must however be taken into account that part of the incident LYMAN- $\alpha$  radiation will be absorbed by  $\text{O}_2$  and  $\text{H}_2\text{O}$  before reaching the fluorescence detector's field of view. At pressures higher than 200 hPa (roughly below 12 km altitude), pre-absorption by both species will result in an increasingly non-linear response of the instrument to  $\mu_V$ . To the other end, above 50 hPa (roughly 20 km),  $\lambda_{hv}$  may no longer be neglected in equation (3.5), as less and less quenching occurs. Consequently, some kind of secondary calibration is required to operate photofragment fluorescence hygrometers. The choice of calibration procedure is an important part of the experimental set-up, and differs among designs by different research laboratories. Fluorescence detection is sufficiently sensitive to determine  $\mu_V$  of the order of 1 ppmv in a few seconds.

The instrument was pioneered by KLEY et al. (1979) as a balloon payload, the NOAA LYMAN- $\alpha$  hygrometer, and fostered the discovery of the tropical hygropause. This instrument, and its subsequent revisions, deploy two nitrous oxide cells to measure LYMAN- $\alpha$  intensity before and after the

fluorescence detector. These allow eliminating the effects of pre-absorption and changes in lamp intensity, which essentially yields a linear response of the instrument to  $\mu_V$  covering several orders of magnitude. Since the instrument is an open cell design, it could only be flown at nighttime, to protect the measurements from systematic errors introduced by stray sunlight. Measurements were calibrated against the LYMAN- $\alpha$  absorption determined in parallel. In the stratosphere, where LYMAN- $\alpha$  absorption by water vapour is virtually nil, an extrapolation of the tropospheric calibration data is required. The airborne version of the instrument has been introduced by KLEY et al. (1982) and later been improved by KELLY et al. (1989). It replaces the nitrous oxide cells with a single but better placed iodine ionisation cell. The new geometry maintains the advantages of the earlier revision while eliminating the need for oxygen absorption correction. It also features a humidifier to allow calibration measurements on a regular basis without requiring the aircraft to pass regions where  $\mu_V \gtrsim 10$  ppmv. The precision of this sensor has initially been stated to be 5% with a total error of at most 20% for stratospheric measurements (0.20 ppmv and 0.80 ppmv, respectively, in the lower stratosphere).

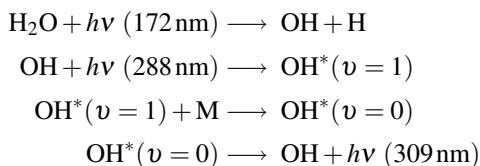
Another design often deployed on aircraft missions is described by WEINSTOCK et al. (1994), the Harvard LYMAN- $\alpha$  hygrometer, later updated by HINTSA et al. (1999). It includes a sophisticated set of filters and collimation in front of the fluorescence detector. The two photodiodes for absorption measurements are positioned such as to allow direct measurement of water vapour concentration according to BEER's law. The system is calibrated by help of a laboratory calibration bench, which provides an accuracy of 5% (corresponding to 0.20 ppmv in the lower stratosphere). The set-up does not identically reproduce all atmospheric conditions, but allows studying the general dependence of the instrumental response to the parameters involved. The instrument also facilitates in-flight calibration, comparable to the NOAA LYMAN- $\alpha$  hygrometer calibration procedure, which is used as consistency check for the laboratory calibration. The combined accuracy is reported as 10% (0.40 ppmv) for stratospheric measurements.

The Fast *In Situ* Stratospheric Hygrometer (FISH), introduced by ZÖGER et al. (1999) at Forschungszentrum Jülich, Germany, addresses some of the shortcomings of earlier designs. It features an improved lamp design, and allows determining the background count rate of the fluorescence detector.

Special emphasis has been put on the design of the laboratory calibration bench to realistically simulate atmospheric conditions. It is concluded measurements under stratospheric conditions can be accomplished to 0.2 ppmv precision in 1 s integration time with an accuracy of about 4% (0.20 ppmv). The instrument has been deployed on both aircraft and balloon.

The Fluorescent Airborne Stratospheric Hygrometer (FLASH) (SITNIKOV et al., 2007), originally devised as Fluorescent Advanced Stratospheric Hygrometer for Balloon (FLASH-B) (YUSHKOV et al., 1995) aims at utmost simplification of instrumental set-up. It sets aside the absorption detectors used in all other designs and instead focuses on providing the highest possible stability in the VUV lamp, which is the most critical parameter with respect to accuracy. The lamp intensity being constant to within 3% error, it was found sufficient to neglect continuous monitoring and only record the intensity for reference before and after flight. Calibration solely relies on laboratory measurements under realistic conditions. The instrument has also been used in rocket-borne soundings of mesospheric water vapour KHAPLANOV et al. (1996). The total error is reported to be about 8% (0.35 ppmv) under stratospheric conditions.

The measurement principle discussed here recently advanced by use of laser induced fluorescence detection (ST. CLAIR et al., 2008). The Hoxo-tope instrument, lending its name and fluorescence detector from the Harvard ER-2 Hydroxyl Experiment ("HO<sub>x</sub>"), provides the sensitivity necessary to determine the isotopic separation  $\delta D$  for H<sub>2</sub>O and HDO (*cf.* section 2.3), and flies aboard the NASA WB-57. Different from the above-mentioned instruments, the radicals are produced in electronical ground-state, and subsequently excited by a laser in a separate volume element that also hosts the fluorescence detectors.



The excitation window at 288nm is chosen to match a weak OH transition with a strong OD transition, to balance out for H<sub>2</sub>O being more than 3 orders of magnitude more abundant than HDO in atmospheric air. A tunable dye laser selectively excites the targeted rovibrational transitions. For 10s acquisition time, which is a limit given by instrumental set-up rather than physical principles, the authors report 5% (0.20ppmv/0.05ppbv) accuracy under stratospheric conditions with a precision of 0.02ppmv for H<sub>2</sub>O and 0.04ppbv for HDO. Due to small sampling volumes and high flow rates, the instrument responds much more rapidly to changes in water abundance than the Harvard LYMAN- $\alpha$  sensor introduced above.

### 3.1.7 Tunable Diode Laser Hygrometers

The optical absorption technique discussed above (*cf.* section 3.1.5) has found new attention when tunable lasers became available in the 1970s. The use of such lasers permits to choose absorption bands of the targeted species that are not affected by foreign effects, which posed a major constraint to water vapour absorption measurement at LYMAN- $\alpha$  wavelength due to highly variable absorption by oxygen. In addition, by retuning the laser to transitions of different line strength, the dynamical range of the measurements may be extended to match the large range of water vapour abundances from the ground to the stratosphere.

The commercial availability of small-package near-infrared TDLs has sparked the construction of instrumentation that is suitable for field use and thus given new rise to the optical absorption method (*cf.* FRIED *et al.*, 2008, for a select overview of today's applications in this area). However, the near-infrared spectral range has been opened up to meet the needs of the telecommunications industry<sup>14</sup>; detection of trace gas absorption at these wavelengths is limited to very weak transitions. Therefore the detectors need to be enhanced by noise-limiting techniques like wavelength modulation spectroscopy (WMS) or frequency modulation spectroscopy (FMS). Figure 3.3

---

<sup>14</sup> The demand for near IR lasers in telecommunication is connected to the loss characteristics of optical fibres, which are dominated by RAYLEIGH scattering towards the UV, rovibrational absorption towards the IR, and loss due to moisture-related impurities. Three windows at 850nm, 1310nm and 1550nm provide extraordinarily low loss.

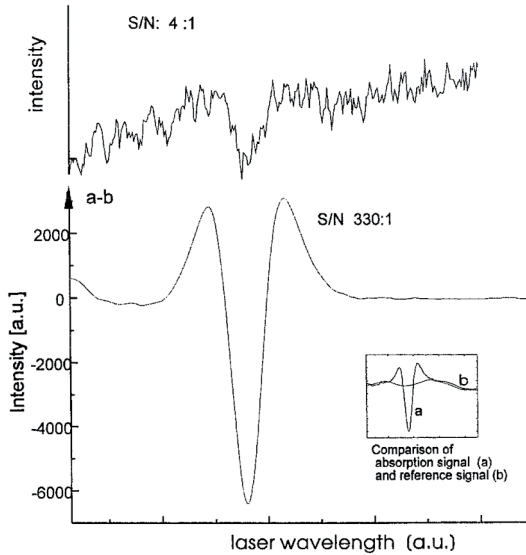


Figure 3.3: Comparison of the absorption signal of a water vapour rovibrational transition at 820 nm, effective optical path-length of 67 m (HERRIOTT cell). The upper panel displays the difference in intensity before and after passage of the cell. Below, the signal from wavelength modulation spectroscopy is given. The increase in signal-to-noise ratio is almost two orders of magnitude. Taken from GROSSKLOSS et al. (1994).

displays the gain in signal-to-noise ratio by WMS. A parallel approach is to enhance interaction length while maintaining a small detector volume by use of external cavities. While multi-pass (HERRIOTT or WHITE) cells gain roughly 2 orders of magnitude in sensitivity, cavities of resonant type (e.g. cavity ring-down spectroscopy, integrated cavity output spectroscopy) may push the detection limit by up to 5 orders of magnitude. An overview of these techniques is given by DEMTRÖDER (2007).

Numerous laser hygrometers have been constructed based on these ideas since the initial demonstrator by SILVER and HOVDE (1994). They commonly share an open-path design that appeals for lack of contamination by water adsorption. Results are often reported as  $\text{H}_2\text{O}$  VMR, despite the directly measurable quantity being number density, as obtained from BEER'S law, equation (3.1). Additional information about ambient pressure and temperature is required to make this transition. Although laser hygrometers routinely take part in aircraft campaigns, intercomparison is rare. An overview of more prominent instruments over the last decade is given below.

The JPL Laser Hygrometer (JLH) for wavelength modulated spectroscopy at  $1.37\ \mu\text{m}$  has originally been devised for the NASA ER-2 platform. It deploys a HERRIOTT cell with a total absorption path-length of 11.13 m

and is capable of measuring water vapour abundance from 0.1 ppmv up to 400 ppmv before reaching saturation. For stratospheric water vapour abundance a precision of  $\pm 0.05$  ppmv has been reported with an accuracy of 5% (0.2 ppmv) (MAY, 1998). A similar instrument is part of the NASA WB-57 instrumentation (READ et al., 2007), whereas for the NASA DC-8, a modified version of the instrument was produced with a single-pass optical path-length of 0.50 m to match the different altitude range of the aircraft. The modified measurement range extends from 10 ppmv to 7000 ppmv, with 1.3% precision at the higher end and 2.7% ( $\sim 0.6$  ppmv) at the lower, and 10% accuracy ( $\sim 2.0$  ppmv) (HERMAN and HEYMSFIELD, 2003). A commercial enterprise (MayComm Instruments Llc, USA) has been spun off and markets the instrument, tailored to the customers' specifications. The Open-path Jülich Stratospheric TDL Experiment (OJSTER), provided by MayComm, features 4 m optical path-length by a HERRIOTT cell, and is quoted a 4 ppmv detection limit with 2% precision and 5% accuracy (0.10 ppmv and 0.20 ppmv respectively). It has been deployed to the enviscope GmbH Learjet and the DLR<sup>15</sup> Falcon (SCHLICHT, 2006). The NCAR<sup>16</sup> flies a MayComm laser hygrometer on the new Earth Observatory Laboratory GV (Gulfstream V) aircraft<sup>17</sup>. This sensor was designed with two optical paths, 10 cm and 130 cm, to provide a combined water vapour detection range of 1 – 30,000 ppmv with better than 10% accuracy, or 0.4 ppmv in stratospheric volume mixing ratio (BOWMAN et al., 2007).

A different type of laser hygrometer has been jointly built by NASA Research Centers Langley and Ames for operation on the NASA DC-8. The Diode Laser Hygrometer (DLH) operates in the same wavelength range as JLH and in a comparable wavelength modulation mode, but does without an external cavity. Instead it spans a large open path from an aircraft fuselage window to the outer engine, parallel to the wing front. The laser beam is returned by a reflector on top of the engine that is built from "road-sign

---

<sup>15</sup> *Deutsches Zentrum für Luft- und Raumfahrt*, [German] German Aerospace Center

<sup>16</sup> National Center for Atmospheric Research

<sup>17</sup> The original project name, High-performance Instrumented Airborne Platform for Environmental Research (HIAPER), has been abandoned, maybe for the reason that the acronym could be mistaken for diaper.

material"<sup>18</sup>, and covers a total distance of 28.5 m before re-entering the window. To address the full dynamic range of tropospheric water vapour, the laser may be tuned to transitions of different line strength at the operator's discretion. The laser beam is allowed slight divergence, rather than being collimated, both for aircraft personnel safety and to minimise the loss of return signal due to water droplets in the path. *In situ* calibration is not feasible for such a long optical path. Two short cells (75 cm and 300 cm) are used instead, assuming the signal is linearly related to path length. Accuracy of the results is claimed to be better than 1 ppmv at 10 ppmv H<sub>2</sub>O abundance. (PODOLSKÉ et al., 2003; FRIED et al., 2008)

Several groups have demonstrated the use of TDL hygrometers from balloon. Such experiments have until very recently been hampered by the high cost and experimental skill required for external cavity laser spectrometers, and the logistics it takes to launch large balloons with heavy payloads. The sensor of the National Physical Laboratory, Teddington, UK, makes use of three wavelengths around 1.36  $\mu\text{m}$  and a HERRIOTT cell providing 101 m optical path. It has been used in the HIBISCUS<sup>19</sup> campaign in 2004, the accuracy is reported to be 10%, or 0.4 ppmv, with a detection limit of 0.5 ppmv (GARDINER et al., 2005). A prototype of the MayComm sensor for balloon has been flown during the Costa Rica campaign of the Aura Validation Experiment in 2006 (BRAATHEN, 2006, *cf.* presentation by H VÖMEL).

The *Groupe de Spectrométrie Moléculaire et Atmosphérique* at the *Université de Reims*, France, share more than a decade of experience with laser hygrometers on stratospheric balloons launched by CNES<sup>20</sup> (DURRY and MEGIE, 1999; DURRY et al., 2004). Their SDLA<sup>21</sup> series of instruments has recently been complemented by PicoSDLA, which takes advantage of new laser diode technology for the mid-IR. Using a spectral window near 2.63  $\mu\text{m}$ , or 3801  $\text{cm}^{-1}$ , two fundamental rovibrational transitions of water vapour with much larger absorption become accessible that allow a dramatic simplification in instrument set-up. A single-pass direct absorption measure-

---

18 3M Corporation Scotchlite Diamond Grade VIP reflective sheeting Series 3990 (PODOLSKÉ et al., 2003).

19 Impact of tropical Convection on the Upper troposphere and lower Stratosphere at global Scale (*sic!*)

20 Centre National d'Études Spatiales, [French] National Center for Space Research

21 Spectromètre à Diodes Laser Accordables, [French] tunable diode laser spectrometer

ment with 1 m optical path suffices to detect water vapour abundance up to 25 km altitude within 10% precision (0.4 ppmv). A WMS revision of the sensor is currently under construction to increase sensitivity and raise the detection limit further up into the stratosphere (DURRY et al., 2008).

Mid-IR quantum cascade lasers (QCL), which require cryogenic cooling, also push the frontier in airborne laser hygrometers. Valuable insight into the isotopic separation of atmospheric water has been provided by ALIAS<sup>22</sup>. This is a closed-path HERRIOTT cell-type instrument fed by a front facing evaporating inlet, so data refer to total water. Water and its isotopologues are detected around 6.73  $\mu\text{m}$ , or 1486  $\text{cm}^{-1}$  (WEBSTER and HEYMSFIELD, 2003; ROSENLOF, 2003). The Harvard group of JG ANDERSON make use of the same wavelength for off-axis integrated cavity output spectroscopy measurements, yielding an optical path-length of the order of 1 km. Their instrument, termed Harvard ICOS<sup>23</sup>, is fed by a rear facing inlet that only captures water vapour. Precision for 4 s measurements of  $\text{H}_2\text{O}$ , HDO and  $\text{H}_2^{18}\text{O}$  are reported as 0.14 ppmv, 0.10 ppbv and 0.16 ppbv, respectively. The corresponding accuracies are deduced from laboratory measurements as 0.20 ppmv, 0.05 ppbv and 0.25 ppbv. It is claimed that from these data the isotopic ratios of water vapour may be inferred with a precision of 50‰ for  $\delta\text{D}$  and 30‰ for  $\delta^{18}\text{O}$  (absolute values) (SAYRES et al., 2008).

### 3.1.8 Mass Spectrometry Hygrometers

An essentially new approach to hygrometry at low mixing ratios (1 – 10 ppm) has recently been awarded support through the Innovative Research Program at the Cooperative Institute for Research in Environmental Sciences (CIRES), at the University of Boulder and NOAA. THORNBERRY et al. (2008) propose to deploy a residual gas analyser for the detection of trace amounts of water vapour. Such devices are routinely being used to check against low levels of water vapour contamination in semiconductor fabrication. Since mass spectrometers detect the ratio of mass to charge, some kind of ionisation of the target species is required. The ratio of mass to charge is recorded for all constituents in a given sample of air. Thus the abundance of

---

<sup>22</sup> Aircraft Laser Infrared Absorption Spectrometer

<sup>23</sup> Harvard Integrated Cavity Output Spectroscopy sensor

water vapour may be referenced to that of nitrogen and oxygen. After careful laboratory calibration, this may serve as a continuous internal standard for measurements of H<sub>2</sub>O mixing ratio.

## 3.2 Remote Sensing

A multitude of sensors exist to remotely sense water vapour from the ground, from aircraft, balloons or rockets, or from space. They record radiation from thermal emission, solar scattering, or occultation and diffraction by Earth's atmosphere. Lidars are special because they actively probe the atmosphere. Table 3.1 gives an overview of the sensors that will be discussed here. The

Type	Platform			
	Ground-based	Balloon-borne	Airborne	Space-borne
MWRS	<i>cf.</i> table 3.2	TELIS	AMSOS MARSCHALS	[MAS] MLS SMR
FTS	⟨IMK⟩ ⟨BIRA-IASB⟩	MIPAS-B2 FIRS-2 MkIV	MIPAS-STR NCAR FTS SAFIRE-A	MIPAS ACE-FTS
Mono- chromating			CRISTA-NF	[HALOE] [MAHRSI] OSIRIS GOMOS SCIAMACHY
GPS	AGNES			BlackJack GPS
Lidar	KARL SRL ⟨JPL Raman⟩ ⟨IMK DIAL⟩		DLR DIAL LASE LEANDRE II	

Table 3.1: Overview of instruments discussed in section 3.2, sorted by platform and type of measurement (MWRS: Microwave Radiometry/Spectrometry, FTS: FOURIER Transform Spectroscopy, Monochromating: Monochromating Spectrometers, GPS: Global Positioning System). For the instrument acronym meanings, the reader is referred to the respective discussions. Square brackets denote instruments that are no longer in operation, angle brackets refer to instruments that bear no individual names.

discussion focusses on sensors that deliver profiles of stratospheric water vapour and are currently in operation. The latter criterion exempts experiments of significant impact, like the POAM<sup>24</sup> II+III and SAGE<sup>25</sup> I–III sensors. Three sensors are introduced despite no longer operating: HALOE forms a point of reference for observations e.g. of the atmospheric tape recorder effect, MAS marks an important step in passive microwave sounding of water vapour from space, and MAHRSI has recently found new interest with respect to the first mesospheric water vapour analyses from spaceborne UV measurements.

Ground-based observations are detrimentally affected by the large tropospheric abundance of water vapour, which effectively screens the signal from the UT/LS and degrades the signal-to-noise ratio of the stratospheric signal. It is therefore mandatory to undertake the observations from high altitude sites. Information about altitude distribution must be obtained from pressure broadening of the observed spectral lines in up-looking/single line-of-sight geometry. This geometry is also found in measurements from aircraft or balloons. Platforms that reach higher into the stratosphere, like large stratospheric balloons<sup>26</sup> or the M-55 Geophysica, NASA WB-57 and NASA ER-2 aeroplanes, allow deploying limb geometry as an alternative. This is the geometry of choice for many space-borne applications. It involves scanning the atmosphere at tangent altitudes, where each measurement is most sensitive at the tangent point<sup>27</sup>. This allows a higher vertical resolution than up-looking geometry, at the expense of coarser horizontal resolution along the line of sight, whose intersection with the atmosphere typically stretches 200 – 400 km, depending on tangent point height.

---

24 Polar Ozone and Aerosol Measurement

25 Stratospheric Aerosol and Gas Experiment

26 A catalogue of stratospheric balloon launches is available online at <http://stratocat.com.ar/indexe.html>.

27 The tangent point is defined as the point where the line of sight most closely approaches the idealised terrestrial globe.

### 3.2.1 Microwave Radiometry/Spectrometry

Microwave radiometers allow detecting the emission from thermally excited rotational transitions in atmospheric trace gas molecules<sup>28</sup>. Measurements may be performed under a large variety of meteorological conditions: The emission is thermally excited within the temperature range found in Earth's atmosphere, so observations are independent of direct solar irradiation. In absence of precipitation, scattering by clouds is also negligible, in particular at lower observation frequencies,  $\nu < 100$  GHz. Yet higher abundance of tropospheric water vapour, as implied by the formation of clouds, results in larger attenuation of the signal received from the middle atmosphere. Information about the vertical distribution of the species of interest is deduced from pressure broadening of the observed transitions, which dominates over DOPPLER broadening at least up to the stratopause. This requires to analyse the emission line shape (*cf.* section 4.1.2). Middle atmospheric trace gas profiles may then be retrieved with a vertical resolution of the order of 10 km. This rather coarse value is accompanied by a good horizontal resolution, of the order of 10 km in ground-based operation. Temporal resolution is determined by the signal-to-noise ratio that is required for retrieval, and thus depends e.g. on strength of the observed transition, and meteorological conditions. The intrinsic accuracy of microwave measurements is high, due to a very stable and simple calibration process (*cf.* section 4.4). The general theory of microwave remote sensing is laid out e.g. by JANSSEN (1993b).

Ground-based microwave observation of water vapour is mostly limited to the weak transition near 22 GHz. A sensor of such kind is used for the results presented in this work, and a short overview of other groups operating similar receivers is given in table 3.2. These groups collaborate within the NDACC<sup>29</sup>. The vertical range of these observations may extend up to 80 – 90 km, given adequately narrow spectrometer channels. By application of the radiometer formula, equation (4.4), these come at the cost of con-

---

28 Given appropriate spectral analysis, individual spectral lines in the emission may be resolved and analysed quantitatively. This type of sensor is discussed herein, and it should be conceived technically as a “microwave spectrometer”, as is indicated by the title of this section. However, the discussion reverts to the term “microwave radiometer” for being prevalent in the microwave spectrometer community.

29 Network for the Detection of Atmospheric Composition Change

Sensor operated by,	Location,	Lat.	Lon.	Altitude (Reference)
MIAWARA <sup>a</sup> IAP <sup>c</sup> , U Bern, Switzerland	Bern, Switzerland	47°N	7°E	550 m a.s.l. <sup>b</sup> (DEUBER et al., 2004)
MIAWARA-C <sup>d</sup> IAP, U Bern, Switzerland	(Prelim. at) Bern, Switzerland			(STRAUB, 2008)
MIRA <sup>e</sup> 5 IMK <sup>f</sup> , FZ Karlsruhe	(Prelim. at) Karlsruhe, Germany			(HOCHSCHILD et al., 2008)
MobRa <sup>g</sup>	(Prelim. at) Toulouse, France Laboratoire d'Aérodynamique, CNRS <sup>h</sup> , U Toulouse III, France			(MOTTE et al., 2008)
Onsala 22 GHz Onsala Space Obs., Sweden	Onsala Space Obs., Sweden	57°N	12°E	Sea level (FORKMAN et al., 2003)
SWARA <sup>i</sup>	Seoul, S Korea Sookmyung Women's U, Seoul, (coop. IAP, U Bern)	37°N	127°E	Sea level (DE WACHTER et al., 2008)
WaRAM <sup>j</sup> IUP <sup>k</sup> , U Bremen, Germany	Ny Ålesund, Svalbard	79°N	12°E	Sea level (LINDNER, 2002)
WaRAM2 IUP, U Bremen, Germany	Mérida, Venezuela	8°N	71°W	4760 m a.s.l. (QUACK, 2004)
WASPAM <sup>l</sup> MPS <sup>n</sup> , Lindau, Germany	ALOMAR <sup>m</sup> , Norway	69°N	16°E	380 m a.s.l. (SEELE and HARTOGH, 2000)
WVMS <sup>o</sup> 1 RSD <sup>p</sup> , NRL Washington, DC, USA	Lauder, New Zealand	45°S	170°E	370 m a.s.l. (NEDOLUHA et al., 2007)
WVMS2 RSD, NRL Washington, DC, USA	Table Mountain, CA, USA	34°N	118°W	2250 m a.s.l. (NEDOLUHA et al., 1996)
WVMS3 RSD, NRL Washington, DC, USA	Mauna Loa, HI, USA	20°N	156°W	3400 m a.s.l. (NEDOLUHA et al., 2007)

*a* Middle Atmospheric Water Vapour Radiometer

*b* above sea level

*c* *Institut für Angewandte Physik*, University of Bern

*d* MIAWARA — Compact

*e* *Millimeterwellenradiometer*

*f* *Institut für Meteorologie und Klimaforschung*, FZ Karlsruhe

*g* Mobile Radiometer

*h* *Centre National de la Recherche Scientifique*

*i* Stratospheric Water Vapour Radiometer

*j* *Wasserdampf-Radiometer für atmosphärische Messungen*

*k* *Institut für Umwelphysik*, University of Bremen

*l* *Wasser- und Spurengasmessung in der Atmosphäre mit Mikrowellen*

*m* Arctic Lidar Observatory for Middle Atmosphere Research

*n* *MAX-PLANCK-Institut für Sonnensystemforschung*

*o* Water Vapor Millimeter-wave Spectrometer

*p* Remote Sensing Division, NRL

Table 3.2: Ground-based microwave receivers at 22 GHz in use for retrieval of middle atmospheric water vapour profiles.

siderably longer integration times though. The lowest altitude for retrieving the profile is around 25km, mainly determined by instrumental limitations, so-called baseline effects, resulting in spurious spectral features. The total errors typically reported for such data are about 0.5 ppmv for integration times of up to 24 hours (e.g. NEDOLUHA et al., 1995).

The water vapour transition at 183 GHz is more than two orders of magnitude stronger than at 22 GHz, i.e. it requires less integration time for a certain signal-to-noise ratio. However, given the large tropospheric water vapour abundance, the signal from the middle atmosphere is usually saturated when observed from the ground. This may be avoided by use of airborne platforms, such as in case of the AMSOS<sup>30</sup> sensor, operated by IAP, U Bern. It flies on a campaign basis aboard a Swiss Army Learjet 35A and allows retrieval of water vapour profiles over an altitude range of 15 – 60km, with a vertical resolution rising from 8km near the bottom of this range to 16km at the top. The horizontal resolution along-track,  $60\text{ km} \pm 30\text{ km}$ , is dominated by spectra pre-integration, which is required to reduce thermal noise. Total error amounts to 10 – 15% (0.3 – 1.0 ppmv) (MÜLLER et al., 2008). The receiver has recently been equipped with two digital FFTS<sup>31</sup> units that help extend observations into the mesosphere. FLURY et al. (2008) report that the new data is suitable to infer lower mesospheric wind speeds, which is difficult to observe by other methods. The IAP team have also studied the feasibility of ground-based measurements at 183 GHz in an AMSOS campaign at the high alpine station Jungfrauoch, Switzerland ( $47^{\circ}\text{N } 7^{\circ}\text{E}$ , 3580 m a.s.l.). Observation of the 183 GHz signature at sufficient signal-to-noise ratio is restricted to very dry conditions in the winter season, and was found to be possible for roughly 7% of the time during November and December 1999. In January to March, no measurements were taken (SIEGENTHALER et al., 2001). KUWAHARA et al. (2008) report test measurements of a newly developed 183 GHz receiver at Atacama desert, Chile ( $23^{\circ}\text{S } 67^{\circ}\text{W}$ , 4800 m a.s.l.). The sensor is currently revised to reduce systematic error sources, introduced by double sideband operation (*cf.* section 4.3).

The 183 GHz signature has been adopted for space-borne measurements

---

30 Airborne Microwave Stratospheric Observing System

31 fast FOURIER transform spectrometer

by MAS<sup>32</sup>, a sensor that has taken part in three ATLAS<sup>33</sup> missions on the NASA Space Shuttle in April 1992, April 1993 and November 1994 (HARTMANN et al., 1996). MAS is conceptually similar to the MLS<sup>34</sup> instrument aboard UARS<sup>35</sup> that operated from September 1991 to August 1999. The 183 GHz receiver of UARS/MLS performed better than MAS, but unfortunately failed in April 1993. A modernised version of the MLS sensor has been devised for the EOS<sup>36</sup>-Aura platform and has been operating since July 2004 (WATERS et al., 1999). H<sub>2</sub>O retrievals from Aura/MLS data yield a vertical resolution better than 4 km below the stratopause, degenerating to worse than 10 km above. The difference is due to the limb sounding geometry, presently limited by the antenna beam width at lower altitudes and the required integration for weak signals higher up. The horizontal resolution is 7 km across-track, as determined by the instrument antenna pattern, and roughly 400 km along the line of sight. For the stratospheric results, the precision is quoted as 0.2 – 0.3 ppmv (4 – 9%) and the total error, estimated from a systematic uncertainty analysis, as 0.2 – 0.5 ppmv (4 – 11%) (LAMBERT et al., 2007).

Recent progress in microwave technology has fostered the construction of a new generation of more powerful receivers, operating at higher frequencies in the sub-millimetre range. Odin/SMR<sup>37</sup> is the first example of such with respect to water vapour observations from space. It has operated since 2002, covering the latitudinal range of 82.5°N to 82.5°S. The instrument shares observation time between aeronomy and astronomy. Standard H<sub>2</sub>O observations are carried out at 489 GHz and 557 GHz for the 20 – 70 km and 40 – 100 km altitude ranges, respectively. Close to 489 GHz, H<sub>2</sub><sup>18</sup>O and HDO isotopologues are also detectable, and a transition of H<sub>2</sub><sup>17</sup>O is observable at 552 GHz. Standard H<sub>2</sub>O measurements are taken on 4 days per month. Altitude resolution is limited to roughly 3 km by the integration time required for a single scan, the horizontal resolution along the line of sight is ~ 400 km. Precision is quoted as 1 ppmv (H<sub>2</sub>O), 0.5 ppbv (HDO), 30 ppbv

---

32 Millimeter-wave Atmospheric Sounder

33 Atmospheric Laboratory for Applications and Science

34 Microwave Limb Sounder

35 Upper Atmospheric Research Satellite

36 Earth Observing System

37 Sub-Millimetre Radiometer

( $\text{H}_2^{18}\text{O}$ ) and 0.4 ppbv ( $\text{H}_2^{17}\text{O}$ ) (URBAN et al., 2007). The lower altitude limit is given by saturation of the observed transition.

Other space-borne sensors have been devised dedicated to UT/LS soundings and stratosphere-troposphere exchange (STE), where the 325 GHz transition of water vapour offers the best trade-off between vertical resolution, line saturation and insensitivity to clouds (GASIEWSKI, 1992). The first such sensor to have actually been built is MARSCHALS<sup>38</sup>. It has flown on the M-55 Geophysica during the SCOUT-O3<sup>39</sup> campaign to Darwin, Australia, in December 2005. The data taken during this campaign indicate the ability to achieve a vertical resolution of less than 2 km for water vapour retrievals in the UT/LS (DINELLI et al., 2008). MARSCHALS has originally been intended as a demonstrator for the MASTER<sup>40</sup> instrument that was considered for inclusion in ESA's ACECHEM<sup>41</sup> space mission. A similar sensor has been proposed by the Odin team for a small satellite successor of Odin named STEAM<sup>42</sup>. Both efforts have recently been merged into the STEAMR (STEAM radiometer) component of the PREMIER<sup>43</sup> proposal which has been selected as one of six candidate missions for the ESA<sup>44</sup> Earth Explorer 7. The PREMIER mission concept involves further advances in terms of synergy between multiple sensors and platforms, and a 3D-tomographic retrieval approach. The latter results in an improved retrieval with better horizontal resolution, by incorporating into the retrieval the geometrical overlap between individual scans.

HOOGVEEN et al. (2005) describe a new balloon-borne instrument named TELIS<sup>45</sup> to fly on the MIPAS-B2 gondola. TELIS can be tuned to the water vapour transition at 557 GHz, yet the receiver performance is reported to be poor at this frequency. This is inferred from the direct-detection response of the mixer, as measured with a FOURIER transform spectrometer. This

---

38 Millimetre-wave Airborne Receiver for Spectroscopy Characterisation of Atmospheric Limb-Sounding

39 Stratosphere-Climate Links with Emphasis on the UTLS

40 Millimeter Wave Acquisitions for Stratosphere/Troposphere Exchange Research

41 Atmospheric Composition Explorer for Chemistry and Climate Interaction

42 Stratosphere Troposphere Exchange and Climate Monitor

43 Process Exploration through Measurements of Infrared and Millimeter-wave Emitted Radiation

44 European Space Agency

45 Terahertz Limb Sounder

method may itself be distorted by the strong H<sub>2</sub>O absorption (WANG et al., 2002), but HOOGEVEEN et al. give no further details about this. The sensor has flown for the first time in the SCOUT-O3 Large Balloon Campaign at Teresina, Brazil, in June 2008, but suffered from major technical problems (OELHAF et al., 2008).

### 3.2.2 FOURIER Transform Spectroscopy

FOURIER Transform Spectroscopy (FTS) denotes the concept of capturing spectra by recording some signal in the time or space domain and then numerically applying a FOURIER transform to convert to the frequency domain. Signals in the time domain may be detected by probing a sample with short light pulses, as for example in nuclear magnetic resonance applications. In FOURIER transform infrared (FTIR) spectroscopy, a MICHELSON interferometer is used to record the signal as a function of path length difference. The spectral resolution is determined by the maximum path length difference achievable with the interferometer. Other significant parameters are detector sensitivity with respect to wavelength, and the instrumental line shape. The FTS set-up operates without monochromators, and thus saves signal intensity for detection that would be lost in a dispersive spectrometer. If the measurement is limited by detector noise, as is commonly the case in the infrared, the method further benefits from the multiplex, or FELLGETT's advantage: Every single measurement simultaneously contributes to all frequency "bins", which offers a higher signal-to-noise ratio than a bin-by-bin measurement, given the same measurement time. This may however also introduce a "multiplex disadvantage" in case of signal fluctuations, which will likewise affect all bins.

Atmospheric FTIR spectroscopy applications depend on a cloud-free line of sight, since otherwise scattering by hydrometeors dominates radiative transfer. Measurements are based on thermal emission or absorption of solar irradiation. The Moon forms another light source, both by reflection of solar radiation and through its own thermal emission (NOTHOLT, 1994). Information about height distribution of trace gases may be inferred from limb geometry as well as from the pressure broadened line shape. However,

DOPPLER broadening limits the latter technique to far lower altitudes than for lines in the microwave range.

Retrieving water vapour profiles from ground-based FTIR data is a rather new application. SCHNEIDER et al. (2006a) report such measurements performed at the high altitude site Izaña Observatory (2.4 km above sea level), on the Island of Tenerife. They present water vapour profiles up to the tropopause, or 11 km altitude, with four independent layers. The uncertainty for the uppermost layer is listed as 50% on the condition of sufficient dryness in the lower troposphere, defined as slant column of less than  $5 \cdot 10^{21} \text{ cm}^{-2}$ . At Izaña Observatory, this criterion is met for about 10% of the data, but it could hold almost year-round at the NDACC primary stations on Mauna Loa, HI, USA, and at Jungfraujoch, Switzerland. Retrieving the isotopic separation  $\delta D$  is also claimed to be possible, at comparable performance (SCHNEIDER et al., 2006b). Similar efforts are also undertaken at Ile de la Réunion (FALLY et al., 2007).

MIPAS<sup>46</sup> denotes a suite of instruments that have been devised at IMK, FZ Karlsruhe, for emission FTIR spectroscopy of the atmosphere in limb geometry. They are deployed on large stratospheric balloons (MIPAS-B), on the M-55 Geophysica stratospheric aircraft (MIPAS-STR), and on Envisat. A comprehensive overview of the Envisat sensor, including measurement modes, calibration and characterisation, retrieval methodology, as well as references to MIPAS on other platforms, is given by FISCHER et al. (2008). Water vapour profiles from Envisat/MIPAS cover the whole globe and reach up to 42 km at a vertical resolution of 4.5 – 6.5 km, degrading to 6 – 8 km in dry regions (polar winter, tropical lower stratosphere). The vertical resolution would considerably benefit from smaller scanning steps, which are 3 km wide in nominal measurement mode between 6 – 42 km tangent altitude, and even larger above. The bottom altitude is limited by cloud top height and uncertainty introduced from the exponential increase in water vapour below the tropopause. The total error is in the range of 6 – 9% (0.2 – 0.6 ppmv) (MILZ et al., 2005). Isotopic separation  $\delta D$  may also be retrieved from these data, however at a coarser vertical resolution. Its total error amounts to less than 20% (35 – 110‰) for a latitudinally averaged analysis (STEINWAGNER et al., 2007).

---

46 Michelson Interferometer for Passive Atmospheric Sounding

The Canadian SCISAT-1 satellite carries ACE-FTS<sup>47</sup>, which operates in solar occultation from a highly inclined orbit. This is complemented by a UV/vis/near-IR grating spectrometer, ACE-MAESTRO<sup>48</sup>, with an almost identical field of view. This opens up unprecedented capacity, among space-borne sensors, to compare results from different spectroscopic methods. Unfortunately, water vapour is not on the priority list for ACE-MAESTRO, and little information has been published about the sparse results available so far. Publications about ACE-FTS also lack details about retrieval performance. As regards spatial resolution, the field of view stretches 3 – 4 km at the tangent altitude. However the spacing of scanning steps depends on the variable duration of individual occultation events: when the sun sets or rises perpendicular to the horizon, i.e. when the satellite heads directly in or against the direction of the sun, it covers more tangent altitude per time than in any other configuration. Altitude spacing of the measurements thus ranges from 2 km for long occultations to 6 km for short ones. Measurement uncertainty is not clearly indicated, but appears to be  $\sim 0.5$  ppmv. (CARLEER et al., 2008)

Airborne FTIR sensors may operate in up-looking or limb geometry. The former, like ground-based observations, require analysis of the pressure broadened line shape to obtain profile information. In this case, the vertical range typically extends from flight altitude to  $\sim 30$  km. From high-altitude operation in up-looking geometry, only column information may be derived. Apart from MIPAS-STR mentioned above, two other sensors should be considered here. The NCAR FTS<sup>49</sup> has been used in intercomparison campaigns for more than 25 years. It routinely flies aboard the NASA DC-8 medium-altitude aircraft, so it is restricted to up-looking geometry and operates in solar occultation mode. Total error for the retrievals obtained during the Aura/MLS validation campaign is 1 – 2 ppmv (COFFEY et al., 2008). SAFIRE-A<sup>50</sup> is special in that it observes far-infrared emission ( $10 - 250 \text{ cm}^{-1}$ ) and may be operated sensitive to polarisation, which is an asset in cloud formation studies. The sensor is dedicated to use on the M-55 Geophysica, with a balloon-borne version under way (CORTESI et al., 2005).

47 Advanced Chemistry Experiment — FOURIER Transform Spectrometer

48 Advanced Chemistry Experiment — Measurement of Aerosol Extinction in the Stratosphere and Troposphere Retrieved by Occultation

49 NCAR FOURIER Transform Spectrometer

50 Spectroscopy of the Atmosphere by Using Far-Infrared Emission — Airborne

Balloon-borne FTIR spectrometers reach higher into the stratosphere and thus cover a larger vertical range than airborne sensors in limb geometry. MIPAS-B2 has already been named above. Two other prominent sensors have recently been used in Aura/MLS validation, too: FIRS-2<sup>51</sup> by the Harvard-Smithsonian Center for Astrophysics is an emission sensor observing the 80 – 1650 cm<sup>-1</sup> range. NASA/JPL's MkIV instrument is operated in solar occultation mode over the 650 – 5650 cm<sup>-1</sup> region. Both yield water vapour results over 8 – 40 km altitude with 2 – 3 km vertical resolution. Total error appears to be of the order of 1 ppmv (LAMBERT et al., 2007).

MIPAS' successors, currently in development at IMK, FZ Karlsruhe, and ICG, FZ Jülich<sup>52</sup>, will allow higher spatial resolution and better coverage by use of two-dimensional detector arrays. GLORIA-AB<sup>53</sup> is prepared for use on the new HALO<sup>54</sup> platform operated by DLR, which is scheduled for its first scientific mission in July 2009. IMIPAS<sup>55</sup> is the corresponding space-borne sensor, which is part of the PREMIER payload currently under consideration for a future ESA Earth Explorer mission (*cf.* section 3.2.1). (FISCHER et al., 2008)

### 3.2.3 Monochromating Sensors

Monochromators, e.g. narrow-bandwidth filters, tunable FABRY-PÉROT interferometers, or diffraction gratings, are used in a variety of sensors covering the wavelength range from UV to far-IR. The combination of a filter and a suitable photodetector essentially renders a fixed-wavelength radiometer. Diffraction gratings are advantageous in that they instantaneously produce spectra. Several types of spectrometers involve a grating that may be revolved without losing focus at the detector and hence allow to record a spectrum, as for example in the EBERT-FASTIE and CZERNY-TURNER setups. These may be complemented by the use of detector arrays. In UV to

---

51 Far-infrared Spectrometer 2

52 *Institut für Chemie und Dynamik der Geosphäre, Forschungszentrum Jülich*, [German] Institute of Chemistry and Dynamics of the Geosphere, Research Centre Jülich

53 Global Radiance Limb Imager Experiment for the Atmosphere — Airborne

54 High Altitude and Long Range Research Aircraft

55 Imaging MIPAS

near-IR applications, CCD<sup>56</sup> arrays are nowadays often used to record the complete instantaneous spectrum at once, so the grating need no longer be revolvable. Middle atmospheric trace gas profiles may be inferred from solar, lunar or stellar occultation measurements, as well as from IR thermal emission.

HALOE<sup>57</sup> on UARS has delivered data about various trace gases, including water vapour, from solar occultation measurements during October 1991 through September 2005. This period does not match the temporal range of the measurements presented in this work, but the large spatial and temporal coverage of HALOE allows many water vapour intercomparisons, which justifies a short introduction here. HALOE provides data from about 30 occultations daily, whose locations vary with UARS-Earth-Sun geometry. Over the course of a year, the data cover a latitude range of roughly 75°N–75°S, and the measurement occurs at a given latitude 10 times a year for both sunrise and sunset. Water vapour abundance is derived from absorption at 6.6 μm over an altitude range of 15 – 80 km. The vertical and horizontal resolution at the tangent point are about 2 km and 10 km respectively. The smallest total errors of 20% or roughly 0.5 – 1.5 ppmv are reported for the 10 – 0.4 hPa layer (~ 16 – 55 km) (HARRIES et al., 1996).

CRISTA-NF<sup>58</sup> is a modernised airborne version of the CRISTA sensor that was twice deployed to space on the ASTRO-SPAS<sup>59</sup> platform in the late 1990s. CRISTA-NF took part in the SCOUT-O3 campaign to Darwin, Australia (*cf.* section 3.2.1). While differing in some instrumental details, both sensors are based on the detection of thermal emission from atmospheric trace gases in the mid-IR spectral range. The spectrometers are of EBERT-FASTIE type, each equipped with multiple exit slits/detectors to cut down acquisition time to ~ 1 s per spectrum. Water vapour abundance is retrieved from three spectral windows around 790 cm<sup>-1</sup> (~ 12.7 μm). The altitude coverage is limited to 7 – 17 km for airborne measurements; measurements can reach higher from space, but no such results have been reported for CRISTA. Resolution of the CRISTA-NF data is roughly 1 km × 2.5 km

---

56 charge-coupled device

57 Halogen Occultation Experiment

58 Cryogenic Infrared Spectrometers and Telescopes for the Atmosphere — New Frontiers

59 Astronomical Shuttle Pallet Satellite

(vert./horiz.) at the tangent point. The retrieval performs best just below the hypopause, where the total error is 20% at most ( $\sim 10$  ppm, *sic!*), becoming larger for higher and lower altitudes. (SCHAELEER et al., to appear; HOFFMANN et al., 2008)

Recently the first mesospheric water vapour retrievals from UV/vis data have been reported. The measurements are obtained from photofragment fluorescence (*cf.* section 3.1.6), which is induced by solar LYMAN- $\alpha$  irradiance in this case. The OH signature near 310 nm is recorded by Odin/OSIRIS<sup>60</sup>, and has also been observed by MAHRSI<sup>61</sup>, which accompanied CRISTA on ASTRO-SPAS. MAHRSI comprises a CZERNY-TURNER spectrometer and an intensified CCD detector. The instrument covers an instantaneous bandwidth of 4 nm with 0.02 nm resolution at 310 nm. OSIRIS on the other hand uses an EBERT-FASTIE type spectrometer and a CCD detector offering lower spectral resolution (1 nm), however at a larger bandwidth of 30 nm. The spectral analysis requires quantitative understanding of the thermal and non-thermal transitions of mesospheric OH. The photofragment signal must be discriminated from RAYLEIGH scattering and solar fluorescence. The latter is stimulated in the already existing OH by the (1, 0) transition at 280 nm, and can be separated from H<sub>2</sub>O photofragment fluorescence due to the lower rotational excitation in solar fluorescence. RAYLEIGH scattering is eliminated from OSIRIS spectra in terms of a reference spectrum. This is taken at 45 km tangent height and corrected for extinction by ozone and residual emission by OH, which is calculated from modelled OH distributions that match well with independent measurements. The reference spectrum is scaled to match the mesospheric limb scans at anchor points outside the observed OH bands at 306 nm, 312 nm, and 317 nm (GATTINGER et al., 2006). MAHRSI spectra resolve three discrete spectral lines from photofragment fluorescence, so the observed emission is instead scaled to match the intensity distribution that is expected according to our understanding of occupation probabilities of individual OH states. The vertical resolution for retrieval from either instrument is given as 4 km, and the altitude coverage is stated as the region where the results match comparative data from HALOE to within 30% ( $< 3$  ppmv), which is 70 – 85 km for MAHRSI and

---

60 Optical Spectrograph and Infrared Imager System

61 Middle Atmosphere High Resolution Spectrograph Investigation

75 – 85 km for OSIRIS. Unfortunately no discussion if the error budgets is presented. (STEVENS et al., 2008)

GOMOS<sup>62</sup> aboard Envisat is a stellar occultation grating spectrometer (KYRÖLÄ et al., 2004). It carries a dedicated detector to determine the extinction by water vapour around 936 nm, but data have not been published in the scientific literature to date. Three presentations<sup>63</sup> at the Second Workshop on the Atmospheric Chemistry Validation of Envisat indicate that results are difficult to obtain from these measurements. SCIAMACHY<sup>64</sup> is another grating spectrometer aboard Envisat. Among others, it performs solar and lunar occultation measurements, which are restricted by the Envisat orbit to the 50°N–70°N (solar occultations) and 20°S–90°S (lunar occultations) latitude bands. Water vapour retrievals from SCIAMACHY are hampered by spoilage of the sensor's near-IR detectors at 2.0 μm and 2.3 μm. PITERS (2007) reports some recent progress with water vapour retrieval from the 936 nm band, sensitive to the 10 – 30 km altitude range.

### 3.2.4 Global Positioning System

The Global Positioning System (GPS) is a global navigation satellite system (GNSS), developed by the United States Department of Defense and operated by the United States Air Force. GPS satellites broadcast minute microwave signals that enable a receiver to determine time, position, and velocity. These microwave signals are subject to diffraction from Earth's atmosphere, and some variability in this diffraction is caused by atmospheric water vapour abundance (BEVIS et al., 1992). So the aberration in signals received from several GPS satellites may be used to infer atmospheric water vapour abundance, usually in terms of total columns.

TROLLER et al. (2006) present a relatively novel approach of retrieving vertical distribution of water vapour from a ground-based network of GPS receivers, using the example of AGNES<sup>65</sup> operated by the Swiss Federal Office of Topography. It involves signals from pairs of satellites reg-

---

62 Global Ozone Monitoring by Occultation of Stars

63 cf. <http://envisat.esa.int/workshops/acve2/presentations/> (all presentations whose titles contain 'GOMOS H2O'), retrieved October 20, 2008

64 Scanning Imaging Absorption Spectrometer for Atmospheric Chartography

65 *Automatisches GNSS-Netz Schweiz*, [German] Swiss Automatic GNSS-Network

istered by pairs of receivers, so-called double-differenced data, which are assimilated into a tomographic analysis. The method is restricted to altitudes below  $\sim 10$  km and requires *a priori* knowledge about temperature. The same applies for the various space-borne sensors which observe GPS signals in radio occultation geometry (*cf.* LUNTAMA et al., 2008, for an overview of such sensors). In addition radio occultation observations allow retrieving the temperature profile of the atmosphere above  $\sim 10$  km at high precision ( $< 1$  K) with a vertical resolution of 0.5 – 1.5 km. The only *a priori* knowledge required is an initial temperature at the upper edge of the measuring range. The selection of this temperature mostly affects the upper layers. GOBIET et al. (2007) report on a novel retrieval scheme for the well-exploited data from the BlackJack GPS sensor aboard CHAMP<sup>66</sup>. Provided the initialisation temperature is adequately chosen, they find the retrieval bias (error) to be less than 0.5 K up to 35 km. Such temperature information could greatly benefit the elimination of uncertainties in mid-latitude stratospheric water vapour trends derived e.g. from HALOE and NOAA balloon data (SCHERER et al., 2008).

### 3.2.5 Light Detection and Ranging

Light Detection and Ranging is an active remote sensing technique, the instruments are nowadays conveniently termed lidars. Atmospheric trace gas abundance is deduced by sending out laser pulses to the atmosphere and recording the backscattered signal. The height information is obtained from the time delay between emission and detection, whereas concentration may be retrieved from the intensity of the backscatter. Two types of lidars allow monitoring atmospheric water vapour, the RAMAN lidar and the differential absorption lidar (DIAL).

A RAMAN lidar makes use of the inelastic RAMAN scattering effect: The incident photon is scattered while exciting a transition in the scattering molecule. The difference in energy (or frequency) of the scattered photon is characteristic of the scattering species. So RAMAN lidars require detection at a other wavelengths than that emitted by the laser. Water vapour mixing ratio is deduced from such measurements by relating the backscatter signal

---

<sup>66</sup> Challenging Minisatellite Payload

from H<sub>2</sub>O to that of N<sub>2</sub>. Yet to account for the instrumental response and the difference in signals produced by either species, some kind of absolute calibration is required. Most commonly, RAMAN lidars are calibrated against measurements by radiosondes.

The advantage of the comparatively simple laser technology is impeded by the small yield of RAMAN backscatter, which limits in particular the altitude range of daytime measurements. GERDING et al. (2004) have demonstrated water vapour retrievals from data taken by the ground-based Koldewey Aerosol RAMAN Lidar (KARL) reaching to 3 km in daylight conditions and 6 – 7 km during darkness. WHITEMAN et al. (2006) report precision better than 10% up to 4 km and 8 km at day and night, respectively, for the ground-based Scanning RAMAN Lidar (SRL) of NASA/GSFC<sup>67</sup>. The instrument frequently participates in intercomparison campaigns. A completely new RAMAN lidar was set up at the Table Mountain facility of NASA JPL. Individual profiles taken with this latter instrument reach as high as 18 km, yet problems in the receiver need to be addressed before the data may reliably be used (LEBLANC et al., 2008).

The DIAL method detects differential absorption of the species in question and thus removes the need for external calibration; it is an application of differential optical absorption spectroscopy (DOAS). Apart from MIE scattering by aerosols in the lower atmosphere, the return signal is largely produced by elastic RAYLEIGH scattering from air molecules, which exceeds RAMAN scattering by several orders of magnitude. Light needs to be sent out at two different wavelengths: The so-called "on-line" wavelength,  $\lambda_{\text{on}}$ , matches a molecular transition of the desired species, so there is significant absorption which attenuates the "on-line" beam according to BEER's law. The "off-line" wavelength is chosen at a distance sufficiently far from  $\lambda_{\text{on}}$  to avoid the absorption, but close enough to retain the same atmospheric scattering as for  $\lambda_{\text{on}}$ .

The distribution of water vapour in the atmosphere is rather unfavourable for ground-based DIAL measurements. Only strong absorption features provide enough backscatter to detect water vapour in UT/LS abundance, but also lead to the signal mostly being absorbed by tropospheric water vapour. Sufficiently strong and spectrally narrow laser pulses are hard to produce.

---

<sup>67</sup> (NASA) Goddard Space Flight Center

The use of water vapour DIALs is hence restricted to locations at higher altitudes or even aircraft. VOGELMANN and TRICKL (2008) report on a new instrument set up at Schneefernerhaus, Zugspitze, Germany. It reaches up to 12 km in daylight by tuning the observation to the line wing, which requires accurate knowledge of spectroscopic parameters and laser wavelength, as well as atmospheric pressure and temperature. Further improvements are required to commit the data to climate research. Three airborne water vapour DIALs have been intercompared by BEHRENDT et al. (2007) in the largest campaign to date of airborne water vapour DIAL: the DLR DIAL aboard the DLR Falcon, LASE<sup>68</sup> of NASA Langley Research Center aboard the NASA DC-8, and LEANDRE II<sup>69</sup> of CNRS aboard the NRL P-3. These sensors cover almost the complete range from ground to flight altitude, at horizontal and vertical resolution typically of the order of 10 km and less than 1 km, respectively. The campaign also serves to study the benefits of a space-borne water vapour lidar mission, which was considered in the European Space Agency's Earth Observation Envelope Programme 2, but eventually not selected for the design phase because of high cost and development risks (DI GIROLAMO et al., 2008). Recently first airborne water vapour lidar measurements of the UT/LS have been reported with the DLR DIAL on the DLR Falcon observing at zenith (KIEMLE et al., 2008).

---

68 Lidar Atmospheric Sensing Experiment

69 *Lidar Embarque pour l'étude des Aerosols et des Nuages, de l'interaction Dynamique-Rayonnement et du cycle de l'Eau*, [French] Lidar for the Study of Aerosols and Clouds, of Interactions Between Dynamics and Radiation, and of the Water Cycle



## 4 Radiometric Observation and Retrieval

The remote sensing group at IUP, U Bremen, observe tropical stratospheric water vapour with the dedicated 22 GHz microwave receiver WaRAM2. QUACK (2004) reports on initial deployment of this sensor to MARS<sup>1</sup>, alongside first results and comparisons. His work serves as a point of reference regarding instrumental details, so it suffices to briefly sum up about them here. The general theory of microwave radiometry is provided e.g. by JANSSEN (1993a).

### 4.1 Atmospheric Emission

The temperature range of the lower and middle atmosphere (roughly  $180\text{K} < T < 310\text{K}$ ) is well within reach for excitation of rotational transitions in atmospheric constituents. The least energetic transitions occur in the microwave region at 0.3 – 300 GHz.

#### 4.1.1 Rotational Transitions

By laws of quantum mechanics, molecules may only attain distinct levels of rotational energy. In a transition between two such levels,  $E_1$  and  $E_2$ , a photon that makes up for the energy difference  $\Delta E$  may be absorbed or emitted,

$$\Delta E = |E_1 - E_2| = h\nu_{1,2},$$

---

<sup>1</sup> Mérida Atmospheric Research Station (Estación de Investigación Ambiental Humboldt, Pico Espejo, 8°32'N 71°03'W, 4765 m a.s.l.)

where  $h$  is PLANCK's constant. A microwave radiometer detects the corresponding radiation at frequency  $\nu_{1,2}$ . For observations by WaRAM2 this is 22.235 GHz, corresponding to the  $6_{1,6} - 5_{2,3}$  transition in  $\text{H}_2\text{O}$  ( $J_{K_a, K_c}$  notation, where  $J$  is rotational angular momentum quantum number and  $K_a, K_c$  pseudo-quantum numbers for the so-called "asymmetric top" rotor (BARBER et al., 2006)). The most prominent emissions in the microwave range result from water vapour and molecular oxygen.

### 4.1.2 Effects on Line Shape and Strength

The strength  $S(T)$  of a transition is governed by quantum mechanics and quantum statistics. It depends on transition probability and occupation of the involved quantum states. The latter is related to temperature  $T$  via the BOLTZMANN distribution. Some more detail about this is given by WOHLT-MANN (2002). The resultant line intensity in terms of absorption coefficient  $\alpha(\nu)$  may be obtained from

$$\alpha(\nu) = nS(T)F(\nu)$$

where  $n$  denotes number density of the species in question and  $F(\nu)$ , normalised to 1, accommodates the independent effects on line shape. These are summarised below, in increasing order of importance (CLANCY and MUHLEMANN, 1993).

#### Natural Line Width

The natural line width is brought about by the finite life-time  $\Delta t$  of the excited state. According to HEISENBERG's uncertainty principle,  $\Delta E \Delta t \gtrsim \hbar$ , this introduces some uncertainty  $\Delta \nu = \Delta E/h$  in frequency. Its contribution to line shape is negligible when compared to the two other phenomena below.

#### DOPPLER Broadening

Thermal movement of the observed gases results in frequency shifts being imposed on the emission/absorption line. In thermodynamic equilibrium,

relative velocities of the individual molecules with respect to the observer obey MAXWELL's distribution. This allows to infer the DOPPLER related line shape,  $F_D(v, v_0)$ , with respect to line centre,  $v_0$ , as

$$F_D(v, v_0) = \frac{1}{\sqrt{\pi} \sigma_D(T)} \exp\left(-\left[\frac{v - v_0}{\sigma_D(T)}\right]^2\right).$$

The broadening parameter  $\sigma_D(T)$  is given by

$$\sigma_D(T) = \frac{v}{c} \sqrt{\frac{2kT}{m}},$$

where  $m$  is molecular mass,  $c$  speed of light and  $k$  BOLTZMANN's constant. The DOPPLER related FWHM<sup>2</sup> may be calculated from  $\Delta v_v(T) = \sqrt{\ln(2)} \sigma_D(T)$ .

### Pressure Broadening

Pressure broadening results from molecular collisions, which shorten the life-times of excited states. This introduces significant additional uncertainty  $\Delta v$ , which increases with pressure,  $p$ . A rather general expression for the line shape  $F_C(v, v_0)$  due to pressure broadening is given by the VAN VLECK-WEISSKOPF function,

$$F_C(v, v_0) = \frac{1}{\pi} \left[\frac{v}{v_0}\right]^2 \left[ \frac{\gamma_C}{[v - v_0]^2 + \gamma_C^2} + \frac{\gamma_C}{[v + v_0]^2 + \gamma_C^2} \right].$$

The broadening parameter,  $\gamma_C$ , involves constants,  $w$ ,  $x$ ,  $w_s$ , and  $x_s$ , that must be determined empirically.

$$\gamma_C = w [p - e] \left[\frac{T_0}{T}\right]^x + w_s e \left[\frac{T_0}{T}\right]^{x_s}.$$

The first term governs pressure broadening due to oxygen and nitrogen, while the second one handles self broadening of the observed species, in this case water vapour, at partial pressure,  $e$ .  $T_0$  is reference temperature, of arbitrary choice.

---

<sup>2</sup> full width at half maximum

### Pressure Shift

The 22 GHz emission line exhibits a pronounced frequency shift that originates from collision induced phase shifts in the radiation. This is accommodated by a modified VAN VLECK-WEISSKOPF line shape,

$$F_C^*(\nu, \nu_0) = \frac{1}{\pi} \left[ \frac{\nu}{\nu_0} \right]^2 \left[ \frac{\gamma_C}{[\nu - \nu_0']^2 + \gamma_C^2} + \frac{\gamma_C}{[\nu + \nu_0']^2 + \gamma_C^2} \right].$$

where  $\nu_0' = \nu_0 + \Delta\nu_0$ , and  $\Delta\nu_0$  denotes frequency shift. The pressure shift parameter bears resemblance to  $\gamma_C$ ; it incorporates the same exponent,  $x_s$ , and another empirical constant,  $d$ :

$$\Delta\nu_0 = d e \left[ \frac{T_0}{T} \right]^{\frac{1}{4} + \frac{3}{2} x_s}.$$

### Altitude Information in Line Shape

The composite line shape is obtained by convolving the individual components. Figure 4.1 illustrates the compound for the 22 GHz and 183 GHz emissions of water vapour in terms of FWHM versus pressure.

The indicated characteristics have important consequences for the presence of altitude information in the line shape. Pressure broadening is linear in pressure, thus exponentially decreasing with altitude. Yet with respect

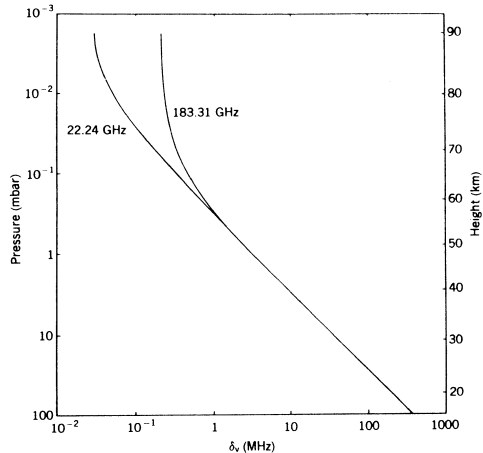


Figure 4.1: Dependence of rotational transition spectral line width on pressure. FWHM of the 22 GHz and 183 GHz emissions of water vapour has been computed in neglect of atmospheric temperature variations. This approximation does not affect the qualitative characteristics shown here. Taken from ROSENKRANZ (1993).

to the microwave range, it is the dominating effect on line shape, at least up to the stratopause. In other words, the signal at certain distance from the spectral line centre is connected to an individual altitude level, and this information may be extracted from the spectra. Contribution to line shape from DOPPLER broadening depends on the root of temperature, so it varies little throughout the lower and middle atmosphere. It also depends linearly on frequency of the observed transition, and this determines how high the spectral altitude information reaches into the mesosphere. The highest range may be attained by the lowest frequencies.

### 4.1.3 Continua

Some atmospheric constituents appear to not fully adhere to the concept of distinct emission lines. In addition to the sharp resonances laid out above, they exhibit some broad “continuum absorption”. The reasons for this are unclear. It could be due to bad representation of the far wings by the VAN VLECK-Weisskopf shape. The effect is particularly strong in water vapour, and must be empirically accounted for. A variety of polynomial representations exist, differing in fine tuning of the parameters (e.g. LIEBE, 1989; CRUZ-POL et al., 1998; ROSENKRANZ, 1998). LIEBE et al. (1993) is different in that it treats the continuum as the result of a pseudo-emission located in the far infrared.

## 4.2 Radiative Transfer

Microwave radiation is affected by emission, absorption, and scattering processes while travelling the atmosphere. The latter are hardest to handle, but, at 22 GHz, only play a dominant role during precipitation, in which case measurements are unfavourable anyway due to strong attenuation by water vapour and clouds. So in the present configuration, we may neglect scattering and thus handle the atmosphere as a grey body. In thermal equilibrium, KIRCHHOFF’s law states that emission  $\epsilon = \alpha$ . Radiative transfer, i.e. change in intensity  $I(\nu, s)$  along a propagation path  $s$  through the atmosphere, may

then be written differentially (JANSSEN, 1993b)

$$\left. \frac{dI}{ds} \right|_{\nu,s} = \alpha(\nu, s) \cdot \left[ -I(\nu, s) + I_{Pl}(\nu, T(s)) \right]. \quad (4.1)$$

$I_{Pl}(\nu, T)$  denotes PLANCK's law. We now introduce opacity  $\tau(\nu, s)$ , the atmospheric optical depth between reference point  $s_0$  and  $s$ ,

$$\tau(\nu, s) = \int_{s_0}^s ds' \alpha(\nu, s').$$

The integrated form of equation (4.1) then reads

$$\begin{aligned} I(\nu, s_0) = & I(\nu, s_\infty) \cdot \exp(-\tau(\nu, s_\infty)) \\ & + \int_{s_0}^{s_\infty} ds \left[ \alpha(\nu, s) \cdot I_{Pl}(\nu, T(s)) \cdot \exp(-\tau(\nu, s)) \right]. \end{aligned}$$

$s_\infty$  typically marks the upper "end" of the atmosphere, where  $I(\nu, s_\infty) = I_{Pl}(\nu, 2.7 \text{ K})$ , the cosmic background radiation.

In atmospheric applications of microwave radiometry, one regularly finds  $h\nu \ll kT$ , which gives rise to the RAYLEIGH-JEANS approximation of PLANCK's law. This motivates a linear scaling of intensity to so-called RAYLEIGH-JEANS (RJ) equivalent brightness temperature,

$$T_{RJ}(\nu) = \frac{c^2}{2k\nu^2} I(\nu) \text{ [K]}.$$

Throughout this work, absolute intensity is expressed in terms of  $T_{RJ}$ . It must not be mistaken for brightness temperature<sup>3</sup>, however in RAYLEIGH-JEANS approximation both values are of the same order of magnitude. For example, the liquid nitrogen cold calibration load of WaRAM2 has a thermodynamic temperature, i.e. brightness temperature, of roughly 73.3 K, but

$$T_{RJ, N_2(aq)}(22.2 \text{ GHz}) = \frac{c^2}{2k\nu^2} I_{Pl}(22.2 \text{ GHz}, 73.3 \text{ K}) = 72.7 \text{ K}$$

## 4.3 Receiver Set-Up

A schematic of the WaRAM2 receiver system is given by figure 4.2. As for

<sup>3</sup> Brightness temperature corresponds to thermodynamic temperature of a black body that would yield the same intensity as observed.

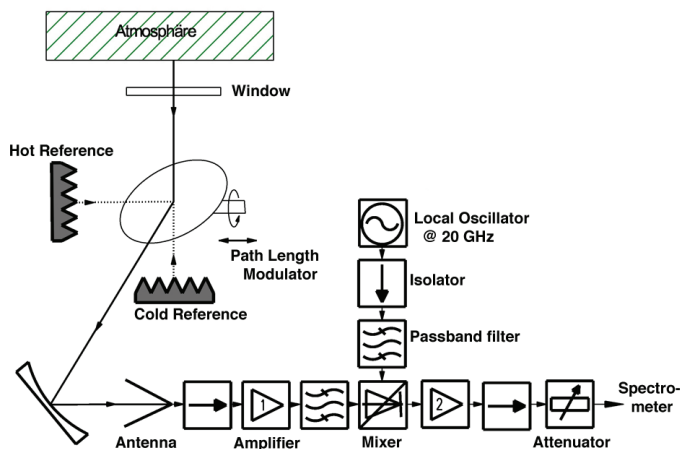


Figure 4.2: Schematic of the WaRAM2 set-up. The placement of quasi-optical elements does not correspond to angles or distances in the actual set-up. Taken from QUACK (2004).

microwave radiometry conventions, the set-up is described from back-end to front-end. WaRAM2 output to spectrometer is centred around 2.1 GHz intermediate frequency (IF). The programmable step attenuator that is indicated as part of the transmission line actually belongs to the spectrometer set-up. Isolator and amplifier 2 of WaRAM2 perform signal conditioning. In the heterodyne mixer, signal conversion from the 21.4 – 22.9 GHz image band to the 1.3 – 2.8 GHz IF band is carried out by superposing the signal with input from the much more intense local oscillator signal at 20.125 GHz. The bandpass filter en route the antenna acts as a sideband filter to suppress the undesired mirror sideband at 17.2 – 18.7 GHz. It is followed by the low-noise amplifier (LNA), which forms the most delicate component with respect to receiver noise. Between antenna and LNA, a waveguide isolator improves impedance matching, and maintains transition from coaxial line to waveguide.

The remaining components comprise the quasi-optics. This term refers to the use of components that are similar to geometrical optics, but in case of microwave beams, it must be considered that the wavelength is of the order of the beam width. This introduces pronounced spreading of the beam in direction of propagation. GOLDSMITH (1998) deals with the details of quasi-optical systems.

With respect to WaRAM2 quasi-optics, a corrugated horn antenna matches

impedance between the waveguide transmission line and free space, and by directivity selects a solid angle of  $\sim 11^\circ$  (FWHM) of the signal. An ellipsoidal mirror focusses the antenna beam to  $\sim 6^\circ$  (FWHM). The revolvable plane mirror is used to select the observation target and, in case of the sky, elevation angle. It integrates a path length modulator to degenerate undesired resonators in quasi-optical set-up.

All components operate at laboratory temperature ( $\sim 288$  K). Cooling, of the LNA and the antenna in particular, might be considered to reduce the thermal noise that the sensor itself contributes to the measurement. This option has been turned down in favour of reduced sensor complexity, which is an important design parameter for remote operation. Below, some components of particular importance for the present work are discussed.

### 4.3.1 Path Length Modulator

Impedance discontinuities introduce weak reflectances to the system, denoted by  $r$ , the fraction of incoming power that is reflected. Discontinuities may arise from mirrors, impedance transitions — like at the antenna —, grids, the liquid surface of the cold calibration load immersed in liquid nitrogen, the calibration load absorber material, microwave windows, and so on. Two opposing reflectors form a resonator, and as power is reflected back and forth within it, standing waves result. They show up as modulations of the measured signal in the frequency domain. The resonator geometry corresponds to the concept of a FABRY-PÉROT resonator. In neglect of loss at the discontinuities, i.e. transmittance  $t = 1 - r$ , the transmitted intensity may be expressed as (BERG, 2000)

$$\frac{I_{tr}}{I_0} = 1 - r_1^2 - r_2^2 + 2r_1 r_2 \cos(2\delta) + \mathcal{O}(r_1^3, r_2^3), \quad (4.2)$$

where

$$2\delta = \frac{4\pi \nu d}{c}$$

denotes phase lag between two consecutive incidences of the beam at one reflector within the resonator, stretching across distance,  $d$ .

Standing waves may not be completely eliminated, because the antenna

always poses a strong reflector in the receiver system, due to the impedance transition from free space to wave guide and, eventually, coaxial transmission line. BERG (2000) reports that the antenna's reflection coefficient typically amounts to 0.2, or 2.6 VSWR<sup>4</sup>. This agrees well with synthetic calculations carried out by HOFFMANN (2008) and within the scope of this work. Recent studies raise questions about how well some 22 GHz corrugated horn antennas are matched to free space (DE WACHTER et al., to appear, and G HOCHSCHILD, IMK, FZ Karlsruhe, pers. corr.). If such problems exist with the WaRAM2 antenna may not be ascertained by the operational measurements presented in this work.

To reduce standing waves, the experimenter must look at the remaining elements of the instrumental set-up, of which there are only a few in the present WaRAM2 design. A path length modulator (PLM) is deployed to reduce the periodic contribution of standing waves to the spectra. It introduces a sinusoidal variation of the resonator length, in the present case by reciprocating the revolvable mirror with amplitude  $d_p$ . GUSTINCIC (1977) has conceptually described the operation of a path length modulator, which yields a modified expression for the intensity transmitted by the resonator,

$$\frac{I_{tr}}{I_0} = 1 - r_1^2 - r_2^2 + 2r_1 r_2 J_0(2\delta_p) \cos(2\delta),$$

where  $2\delta_p = 2\delta d_p/d = 4\pi \nu d_p/c$  denotes the maximum difference in phase lag introduced by the reciprocating mirror.  $J_0(x)$  is a BESSEL function of first kind, which arises from averaging over an expression like  $\cos(d + d_p \sin(\omega t))$ .

Standing waves are suppressed by adjusting  $2\delta_p$  to a root of  $J_0(x)$ . Since  $\delta_p$  is related to signal frequency, ideal suppression can only be achieved for a single frequency. Because of this,  $d_p$  should in general be chosen with respect to the centre frequency of the observed transition. However, the suppression at the left and right ends of the observed bandwidth is still about two orders of magnitude: When optimising about the first root of  $J_0(x)$ ,  $x_1 = 2.405$ , we obtain

$$d_p = \frac{x_1 c}{2\pi \cdot 22.235 \text{ GHz}} = 2.58 \cdot 10^{-3} \text{ m.}$$

---

4 voltage standing wave ratio

Using this value, and solving for  $x = 2\delta_p$  at 21.6GHz, yields 2.336 and  $J_0(2.336) = 3.62 \cdot 10^{-2}$  (at 22.8GHz: 2.466,  $J_0(2.466) = -3.13 \cdot 10^{-2}$ ).

It is important to note that suppression of standing waves by a path length modulator only affects the modulation of the received signal, i.e. the cosine term in equation (4.2). In other words, the received intensity is still systematically lower than it would be in absence of the standing wave. This must be considered when assuming the radiance received from the cold load, which is affected by strong resonators between different parts of the antenna and the liquid nitrogen surface in the cold calibration load (*cf.* section 5.1.4).

### 4.3.2 Local Oscillator

The local oscillator (LO) has been a source of trouble in earlier operation of WaRAM2 (QUACK, 2004). It has been refurbished in 2004 and 2005, but failed again in the spring of 2005, shortly after being reinstalled. Before commencing measurements in the winter of 2006, the local oscillator has been reconfigured and complemented by a power booster to accomplish the 13dBm signal level required by the WaRAM2 mixer. Yet despite these efforts, degradation of the local oscillator is again apparent from the data presented below (*cf.* section 5.1.1).

### 4.3.3 Low Noise Amplifier

The overall receiver performance is largely dependent on noise level  $P_N$  of the LNA. The noise characteristics of an amplifier with amplification,  $G$ , and bandwidth of operation,  $\Delta\nu$ , are commonly expressed as noise figure

$$F = 10 \cdot \lg \left( 1 + \frac{P_N}{P_0} \right) \quad [\text{dB}].$$

It is referred to the noise level  $P_0 = GkT_0\Delta\nu$  of an ideally matched resistor at reference temperature  $T_0 = 290$  K. The original WaRAM2 LNA has a noise figure  $F$  of 3.6dB, which is far from optimum. As supposed by QUACK (2004), a LNA with  $F = 1.9$  dB has been acquired and fitted to WaRAM2 as part of this work.

### 4.3.4 Spectrometer

The receiver signal is spectrally resolved by an acousto optical spectrometer (AOS) (SCHIEDER et al., 1989, refer to SEST-LRS for a predecessor of the type used here). It delivers 100 spectra per second, at  $\sim 1.2$  GHz usable instantaneous bandwidth. Each spectrum comprises 2048 channels with 0.7 MHz spacing and a resolution bandwidth of 1.1 MHz. Laser and BRAGG cell are temperature stabilised by a dedicated water cycle.

To obtain a frequency grid for the observed spectra, a comb generator signal is measured at regular intervals, which provides the harmonics of a 100 MHz signal. In addition, “dark current” or zero spectra may be read from the AOS, which is the reported signal with the input port terminated by a  $50\Omega$  resistance. It is important to correct for the zero spectrum when analysing a comb spectrum, because the odd and even channels systematically disagree in offset (KRUPA, 1998). It must also be considered when calculating direct ratios of raw spectra, like in calculation of the Y-factor (*cf.* below) or for the linearity analysis presented in section 5.1.3. However in total-power calibration, no zero correction is required, since in that case only direct differences of raw spectra are considered.

The spectrometer has originally been dedicated to the MIRA 2 radiometer that is operated by FZ Karlsruhe for the observation of ozone and other trace gases (KOPP, 2000, e.g. ). At MARS, observation time is shared between MIRA 2 and WaRAM2. Both sensors would greatly benefit from providing a dedicated spectrometer for WaRAM2 observations. At the same time, the upper altitude limit for retrieval might be improved, which is currently set to  $\sim 50$  km by the resolution bandwidth of the present AOS. A new generation of FFTS developed at MPIfR<sup>5</sup>, Bonn, Germany, allows replacing the AOS without requiring further modification to the existing receiver setup, because they may analyse the 1.5 – 3.0 GHz range by under-sampling at  $3\text{GS s}^{-1}$ .<sup>6</sup> The currently available configurations include 1.5 GHz instantaneous bandwidth at 212 kHz resolution bandwidth and 0.75 GHz instanta-

5 MAX-PLANCK-*Institut für Radioastronomie*, [German] MAX PLANCK Institute for Radio Astronomy

6 An adaptation of the IF chain to a new spectrometer would be desirable in the long run, though. The current IF band is located at 1.3 – 2.8 GHz. This would result in the 1.5 – 1.3 GHz signal being imaged to the 1.5 – 1.7 GHz reading of the FFTS discussed here, and

neous bandwidth at 53 kHz resolution bandwidth, which can be chosen from in software (KLEIN et al., 2008).

## 4.4 Measurement Calibration

The detected spectral power must be calibrated to meaningful frequency and power units. With respect to the latter, it is worthwhile noting that noise added by the receiver components is an integral part of the measurement. In simplified form, the power read from a spectrometer channel,  $C_i$  (shorthand for “(spectrometer) counts in response to antenna input  $i$ ”), may be expressed as

$$C_i = G[T_{RJ,i} + T_{RJ,rec}] + C_{zer} \text{ [a.u.]}. \quad (4.3)$$

Here  $G$  denotes a proportionality factor,  $T_{RJ,i}$  power incident to the antenna,  $T_{RJ,rec}$  noise contribution from the receiver (receiver noise temperature), and  $C_{zer}$  zero spectrum of the spectrometer. All parameters exhibit individual dependence on observation frequency, which is dropped for clarity.  $[T_{RJ,i} + T_{RJ,rec}]$  is termed system noise temperature,  $T_{RJ,sys}$ . To first order, it determines the sensitivity of the sensor to changes in input signal,  $\Delta T_{RJ}$ . This is given by the well known radiometer formula,

$$\Delta T_{RJ} \propto \frac{T_{RJ,sys}}{\sqrt{B\tau}}, \quad (4.4)$$

where  $B$  denotes spectral bandwidth and  $\tau$  observation time.

### 4.4.1 Frequency Calibration

Figure 4.3 exemplifies how a frequency scale is assigned based on a zero-corrected comb spectrum. GAUSSIAN distributions are fitted to the individual teeth by minimisation of the residua, which yields fractional channel positions of the comb teeth. Knowledge about which frequency to expect at the  $n$ -th tooth is fed separately to the algorithm. The resultant (position, frequency) pairs are used as support grid, from which frequencies for

---

the 2.8 – 3.0GHz signal being lost, yielding an observable radio frequency range of 21.8 – 22.9GHz.

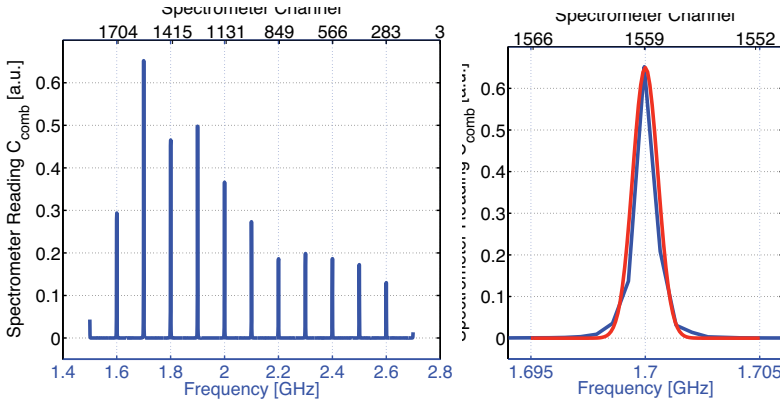


Figure 4.3: Example of a WaRAM2 frequency calibration for data taken on 12 Jan 2007, 20:44 UTC. (Left panel) Comb spectrum plotted versus spectrometer channels (top axis) and resultant frequency calibration (bottom axis). (Right panel) Detail of a single comb tooth. A GAUSSIAN distribution is fitted to the signal by minimisation of the residuum (result plotted in red) to obtain its (fractional) channel position.

the integer channel numbers are obtained by cubic interpolation. The outlined procedure forms an improvement over the previously existing algorithm, which lacked zero-correction, matched the comb teeth positions less well, and used linear interpolation between the grid points.

#### 4.4.2 Total-Power Calibration

Recalling equation (4.3), neither  $G$  nor  $T_{RJ,rec}$  are known for the individual spectrometer channels, and some kind of power calibration is required to solve for any  $T_{RJ,i}$ , in particular atmospheric signal. In WaRAM2, so-called total-power calibration is regularly carried out. To this end, observation of the atmosphere,  $T_{RJ,a}$ , is interleaved with measurements of the signals of two black body calibration loads,  $T_{RJ,h}$  and  $T_{RJ,c}$ , at well known physical temperatures,  $T_h \approx 293$  K (laboratory ambient temperature) and  $T_c = 73.3$  K (liquid nitrogen temperature at  $p \approx 575$  hPa). By application of equation (4.3), this results in a linear system of three equations in the three unknowns,  $G$ ,  $T_{RJ,a}$ , and  $T_{RJ,rec}$ , which may easily be solved for atmospheric signal

$$T_{RJ,a} = \frac{C_a - C_c}{C_h - C_c} \cdot [T_{RJ,h} - T_{RJ,c}] + T_{RJ,c}. \quad (4.5)$$

A typical calibration cycle is illustrated by figure 4.4. The algorithmic implementation of total-power calibration also has been refined during this work, and a  $\sim 0.5$  K positive bias has been removed from the calibration.

### 4.4.3 Receiver Noise Temperature

The system of equations mentioned above may be solved for receiver noise temperature instead,

$$T_{RJ,rec} = \frac{T_{RJ,h} - Y T_{RJ,c}}{Y - 1} \quad \text{with } Y = \frac{C_h - C_{zer}}{C_c - C_{zer}}.$$

$Y$  is called the Y-factor and gives initial indication about receiver performance with respect to noise, if  $T_{RJ,h}$  and  $T_{RJ,c}$  are well known and constant. Typical characteristics of WaRAM2 receiver noise temperature and their improvement by instrumental updates are given in figure 4.5. The transition from 2004 ( $\overline{T_{RJ,rec}} = 660$  K, 633 K at  $\nu_{H_2O}$ ) to 2005 ( $\overline{T_{RJ,rec}} = 470$  K, 432 K at  $\nu_{H_2O}$ ) indicates that a proper level of LO power is crucial in sensor operation. The mixer specifications demand for 13 dBm LO power, which has been hard to meet in the past. It is strongly advised to evaluate new LO and

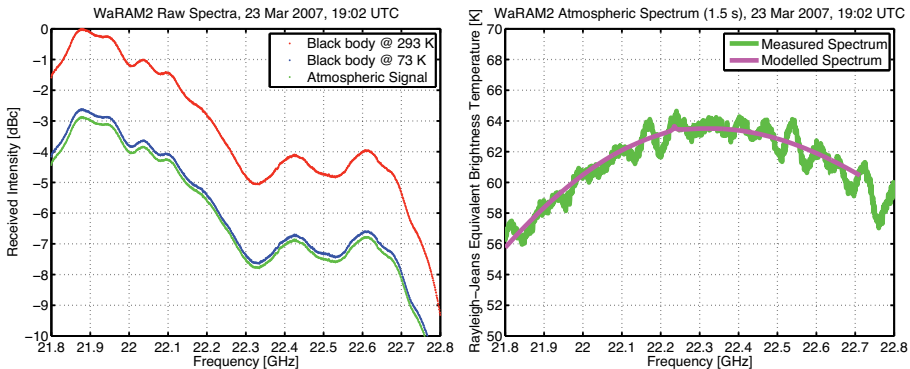


Figure 4.4: Example of a WaRAM2 total-power calibration for data taken on 23 Mar 2007, 19:02 UTC. (Left panel) Raw spectra  $C_h$ ,  $C_c$ , and  $C_a$ , in units of dBc by reference to the maximum reading in  $C_h$ . (Right panel) Total-power calibrated spectrum obtained from equation (4.5), superposed by an example retrieval.

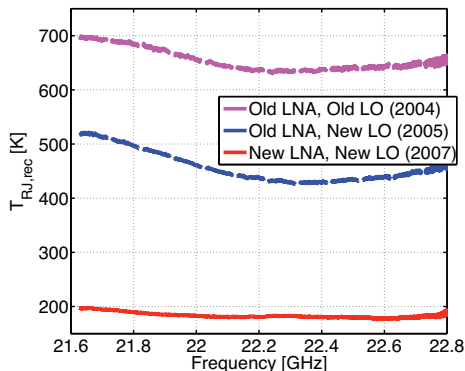


Figure 4.5: Examples of WaRAM2 receiver noise temperature. Data taken on 2 Apr 2004 5:53, 12 Mar 2005 22:29, and 12 Jan 2007 20:00 (all times UTC). Between 2004 and 2005, the local oscillator has been refurbished, and in late 2005, the low noise amplifier has been upgraded.

mixer options for future instrumental upgrades, to eliminate the apparent shortcomings of the present configuration.

The benefit from the new LNA ( $\overline{T_{RJ,rec}} = 194\text{K}$ ,  $183\text{K}$  at  $\nu_{\text{H}_2\text{O}}$ ) may also be appreciated from figure 4.5. In total, WaRAM2 receiver noise has been reduced by almost a factor of 4 since first operation at MARS. In terms of the radiometer formula, equation (4.4), observation time  $\tau \propto \frac{1}{T_{RJ,sys}^2}$  when maintaining the same sensitivity. Hence under favourable atmospheric conditions,  $T_{RJ,a} = 10\text{K}$ , a factor of 11 in measurement time is gained, while in very bad conditions,  $T_{RJ,a} \approx 100\text{K}$ , the improvement still amounts to a factor of 6.7.

## 4.5 Integration of Spectra

To reduce thermal noise on the recorded spectra, we integrate<sup>7</sup> over consecutive measurements. WOHLTMANN (2002) discusses in some detail an algorithm that allows integrating spectra of varying tropospheric background. It applies a scaling factor to the spectral line information received from the stratosphere, which individually corrects for the attenuation due to tropospheric radiative transfer. To this end, for analysis of earlier WaRAM2 data QUACK (2004) reverts to a two layer model of the atmosphere, in which the troposphere is treated like a sheet of semi-transparent absorber, so tro-

<sup>7</sup> "to integrate spectra" is common speak for "averaging over a series of spectra" in the microwave radiometry community

pospheric attenuation is directly related to the recorded background temperature. The quantitative relationship may be derived from radiative transfer model calculations when using correlative profile data, e.g. from radiosondes, as input. This strategy resembles the reference beam calibration approach for observations at 22 GHz. In these, the required scaling is deduced from sky tipping measurements (e.g. NEDOLUHA et al., 1995). Yet the two layer model implies that the tropospheric attenuation occurs uniformly, independent of frequency. This assumption only holds close to the spectral line centre, which effectively limits the altitude range for retrieval to above 35 km (ibid.). For a more complete discussion of the two layer model shortcomings with respect to water vapour retrieval, the reader is again referred to WOHLTMANN (2002).

In the light of above named restrictions, the present work is concerned with obtaining information about tropospheric attenuation directly from the spectra. This may in principle be done by considering the tropospheric part of the water vapour profile in logarithmic retrieval, i.e. when retrieving for the logarithm of the state vector,  $\log(\mathbf{x})$ . This requirement is introduced by the exponential gradient of water vapour distribution across the troposphere. However neither QUACK (2004) nor the present work have so far succeeded in obtaining sufficient retrieval convergence in this approach. For the time being, we must ensure to only integrate over spectra that have been taken under comparable atmospheric conditions. An illustration of this is given by figure 4.6. The integration algorithm starts from an analysis of the average spectral power in a 70 MHz interval around the line centre to infer atmospheric variability. An atmospheric spectrum is only considered in integration if its average spectral power within this interval is at most 5 K more than the smallest value found in the course of a day. Depending on atmospheric conditions, this results on average in half of the measurements being discarded.

## 4.6 Retrieval of Geophysical Parameters

To retrieve geophysical parameters from the measured spectra, henceforth denoted by  $\mathbf{y}$ , we require a model,  $\mathbf{F}$ , of atmospheric radiative transfer that relates  $\mathbf{y}$  to the desired quantities, in particular the volume mixing ratios of

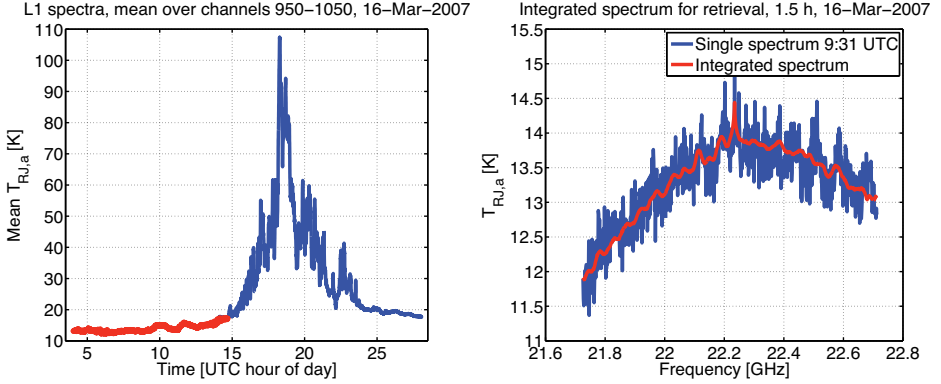


Figure 4.6: Example results of the integration algorithm for WaRAM2 spectra, which aims at maintaining uniform atmospheric conditions in all integrated spectra. Individual measurements comprise 1.5 s of atmospheric observation. (Left panel) Average spectral power in a 70MHz interval around the line centre, plotted versus time. Red colour indicates spectra that are considered in integration. (Right panel) The integrated spectrum (red) is compared to an individual spectrum (blue).

trace gases at different altitudes. They are part of the state vector,  $\mathbf{x}$ , which holds all parameters that contribute to  $\mathbf{y}$  in a reproducible way. RODGERS (2000) deals in great detail with the aspects of such retrieval, and the following discussion is based on his work.

The relationship between between state vector and measurement is given by

$$\mathbf{y} = \mathbf{F}(\mathbf{x}) + \varepsilon,$$

where  $\varepsilon$  denotes measurement error.  $\mathbf{F}(\mathbf{x})$  is called the forward model. To make  $\mathbf{F}(\mathbf{x})$  available to computational solution, and use the powerful apparatus of linear algebra,  $\mathbf{F}(\mathbf{x})$  must be discretised and linearised about some linearisation point  $\mathbf{x}_l$ , like

$$\mathbf{y} = \mathbf{F}(\mathbf{x}_l) + \mathbf{K}_l[\mathbf{x} - \mathbf{x}_l] + \varepsilon + \mathcal{O}([\mathbf{x} - \mathbf{x}_l]^2), \quad \text{where } \mathbf{K}_l = \left. \frac{\partial \mathbf{F}}{\partial \mathbf{x}} \right|_{\mathbf{x}_l}$$

$$\Leftrightarrow \mathbf{y} \approx \mathbf{K}_l \mathbf{x} + \varepsilon \quad \text{by choice of coordinates.} \quad (4.6)$$

For traditional reasons,  $\mathbf{K}_l$  is called the weighting functions matrix, but a variety of names are in use for it, and often it is merely denoted the JACOBIAN

(matrix of the forward model). Its dependence on linearisation point  $\mathbf{x}_l$  will initially be dropped for clarity.

The trouble in solving equation (4.6) for  $\mathbf{x}$ , in atmospheric applications, arises from the rows of  $\mathbf{K}$  being almost all linearly dependent; the system is over-determined. Furthermore  $\mathbf{K}$  has a null space, i.e. there exist non-zero states  $\mathbf{x}_N$  for which  $\mathbf{K}\mathbf{x}_N = 0$ . These states do not contribute to  $\mathbf{y}$ , in other words, information about them cannot be inferred from a measurement of  $\mathbf{y}$ . Hence equation (4.6) is under-determined at the same time. The problem is made worse by the presence of noise.

To overcome the limitations of this so-called ill-posed problem, additional information must be introduced in terms of regularisation. This may for example be done by imposing a smoothness constraint on the solution, as in TIKHONOV regularisation. From a BAYESian point of view, prior knowledge about the expected solution may be used. This is the direction taken here, commonly referred to as optimal estimation method (OEM). This assumes that we know about the mean solution  $\mathbf{x}_a$ , the *a priori* state, and associated covariance matrix  $\mathbf{S}_x$ . Based on this information, the best estimate of the solution,  $\hat{\mathbf{x}}$ , is the  $\mathbf{x}'$  that minimises the cost function

$$\chi^2 = [\mathbf{x}' - \mathbf{x}_a]^T \mathbf{S}_x^{-1} [\mathbf{x}' - \mathbf{x}_a] + [\mathbf{y} - \mathbf{K}\mathbf{x}']^T \mathbf{S}_\varepsilon^{-1} [\mathbf{y} - \mathbf{K}\mathbf{x}'].$$

$\mathbf{S}_\varepsilon$  is the measurement noise covariance. Assuming linearity of the forward model,  $\mathbf{y} = \mathbf{K}\mathbf{x} + \varepsilon$ , and GAUSSian probability distributions, the best estimate may be derived analytically as

$$\hat{\mathbf{x}} = \mathbf{x}_a + \mathbf{G}[\mathbf{y} - \mathbf{K}\mathbf{x}_a], \quad (4.7)$$

where  $\mathbf{G}$  is the gain matrix, or contribution function matrix,

$$\mathbf{G} = \mathbf{S}_x \mathbf{K}^T [\mathbf{K}\mathbf{S}_x \mathbf{K}^T + \mathbf{S}_\varepsilon]^{-1}. \quad (4.8)$$

Equation (4.7) is a useful expression to study retrieval characteristics, of which some results shall be given here. Introducing the averaging kernel matrix  $\mathbf{A} = \mathbf{G}\mathbf{K}$ , we obtain a relation between the best estimate  $\hat{\mathbf{x}}$  and the true atmospheric state  $\mathbf{x}$ ,

$$\hat{\mathbf{x}} = \mathbf{A}\mathbf{x} + [\mathbf{I} - \mathbf{A}]\mathbf{x}_a + \mathbf{G}\varepsilon. \quad (4.9)$$

It becomes clear that  $\mathbf{A} = \partial\hat{\mathbf{x}}/\partial\mathbf{x}$ , so  $\mathbf{A}$  describes the sensitivity of the retrieval to changes in the true state. For the elements of the state vector that

represent a profile, the corresponding rows of  $\mathbf{A}$  describe smoothing functions, the so-called averaging kernels. For an example plot, the reader is referred to the retrieval characteristics discussion in section 5.2.2 (figure 5.21).

A vast range of information can be gained from the averaging kernels. Their shape tells about altitude resolution of the retrieval. At altitudes where the measurement provides sufficient information for retrieval, the averaging kernels should peak at the associated grid level. This corresponds to  $\hat{x}_p$  (the element of  $\hat{\mathbf{x}}$  that belongs to layer  $p$ ) being a weighted mean of the true state values  $x_{p\pm\Delta p}$  around that layer. Furthermore, the area below an averaging kernel should be unity in this case. At levels where it is not, the *a priori* contributes to the best estimate as per the second term in equation (4.9).

Two types of error in the estimated profile can be derived from equation (4.9), which will be considered when discussing results below. Solving for error,  $\delta_{\hat{\mathbf{x}}} = \hat{\mathbf{x}} - \mathbf{x}$ , we obtain

$$\delta_{\hat{\mathbf{x}}} = [\mathbf{A} - \mathbf{I}] [\mathbf{x} - \mathbf{x}_a] + \mathbf{G}\boldsymbol{\varepsilon}. \quad (4.10)$$

The first term on the right hand side is called smoothing error and describes the error related to finite resolution of the retrieval. To accurately estimate the loss of information in  $\hat{\mathbf{x}}$  from smoothing, i.e. the smoothing error statistics in terms of covariance  $\mathbf{S}_s$ , the smoothing errors  $[\mathbf{A} - \mathbf{I}] [\mathbf{x}' - \bar{\mathbf{x}}]$  need to be explicitly calculated for an appropriate ensemble of states  $\{\mathbf{x}'\}$  with mean  $\bar{\mathbf{x}}$ . When  $\mathbf{S}_E$  is the covariance of the ensemble about  $\bar{\mathbf{x}}$ , this yields

$$\mathbf{S}_s = [\mathbf{A} - \mathbf{I}] \mathbf{S}_E [\mathbf{A} - \mathbf{I}]^T. \quad (4.11)$$

The second term on the right hand side of equation (4.10) represents the retrieval noise, or observation error. Since the covariance related to measurement noise  $\boldsymbol{\varepsilon}$  may usually be directly observed, we may immediately deduce

$$\mathbf{S}_o = \mathbf{G}\mathbf{S}_\varepsilon\mathbf{G}^T. \quad (4.12)$$

Atmospheric applications usually fall short of the assumption that  $\mathbf{F}(\mathbf{x})$  is linear, which was embedded in equation (4.7) to find a best estimate  $\hat{\mathbf{x}}$ . We must instead start with an initial guess  $\mathbf{x}_0$  (which may, but need not be  $\mathbf{x}_a$ ), and iteratively seek the solution. In water vapour retrievals, the tropospheric distribution introduces considerable non-linearity, which may be appropri-

ately tackled by using LEVENBERG-MARQUARDT iteration:

$$\mathbf{x}_{i+1} = \mathbf{x}_i + [\mathbf{S}_x^{-1} + \gamma_i \mathbf{D} + \mathbf{K}_i^T \mathbf{S}_\varepsilon^{-1} \mathbf{K}_i]^{-1} [\mathbf{K}_i^T \mathbf{S}_\varepsilon^{-1} [\mathbf{y} - \mathbf{F}(\mathbf{x}_i)] - \mathbf{S}_x^{-1} [\mathbf{x}_i - \mathbf{x}_a]].$$

The diagonal scaling matrix  $\mathbf{D}$  accommodates for different magnitudes and dimensions in  $\mathbf{x}$ , and its simplest choice is  $\mathbf{D} = \mathbf{S}_x^{-1}$ .  $\gamma_i$  governs a balancing between plain GAUSS-NEWTON iteration ( $\gamma_i \rightarrow 0$ ) and steepest descent ( $\gamma_i \rightarrow \infty$ ). In the present work,  $\gamma_i$  is handled according to the strategy by PRESS et al. (*cf.* (RODGERS, 2000)): The retrieval is provided an initial value,  $\gamma_0$ , which is updated according to the change in  $\chi^2$ . If  $\chi^2$  decreases as the result of an iteration step,  $\gamma_i$  is reduced by a factor  $c_0$ . Otherwise,  $\gamma_i$  is raised by a factor  $c_\infty$ , and the iteration step is repeated, i.e. the  $\mathbf{x}_{i+1}$  which increased  $\chi^2$  is dismissed.

It may be shown that the error terms derived above, equations (4.11), (4.12), maintain the same shape in non-linear problems, as long as  $F(\hat{\mathbf{x}})$  is close to linear with respect to the range of measurement error  $\varepsilon$  (the moderately non-linear case, according to RODGERS (2000)). Yet it is of crucial importance now to consider the dependence of  $\mathbf{K}_l$  on linearisation point  $\mathbf{x}_l$ , which will affect entities  $\mathbf{A}$  and  $\mathbf{G}$  in above equations. Applying

$$\hat{\mathbf{K}} = \left. \frac{\partial \mathbf{F}}{\partial \mathbf{x}} \right|_{\hat{\mathbf{x}}}$$

in equation (4.8), we obtain a modified gain matrix  $\hat{\mathbf{G}}$  and subsequently averaging kernels matrix  $\hat{\mathbf{A}} = \hat{\mathbf{G}} \hat{\mathbf{K}}$  for use in error quantification.

## 4.7 Retrieval Set-Up

Computationally, the retrieval is carried out using ARTS<sup>8</sup>-1-0 (BUEHLER et al., 2005), a versatile software that simulates atmospheric radiative transfer for monochromatic pencil beams in absence of scattering and on the assumption of local thermodynamic equilibrium. Both conditions apply in case of the present observations. Large parts of the software have been developed at IUP, U Bremen. The retrieval set-up is maintained by Qpack

<sup>8</sup> Atmospheric Radiative Transfer Simulator

(ERIKSSON et al., 2004), a package of Matlab scripts that assists the user in sensor modelling, error characterisation, and optimisation of the calculation grids, among others. Most importantly, the iterative inversion is carried out by Qpack. It also allows considering polynomial and periodical baseline parameters as part of the retrieval.

In operational WaRAM2 retrieval, a polynomial of order 1 (i.e. slope and offset) is considered, as well as a variable set of twenty standing wave periodicities (*cf.* section 5.1.4). *A priori* water vapour is taken from the FAS-COD tropical atmospheric scenario (ANDERSON et al., 1986). Temperature, pressure, and altitude information are taken from ECMWF operational analyses by linear interpolation between the surrounding grid points. Spectroscopy is chosen according to ROSENKRANZ (1998). This is a full model for emission/absorption by water vapour, so the line shape configuration of ARTS/Qpack does not come into play. Furthermore the oxygen, nitrogen, and carbon dioxide continua are considered according to ARTS formulations O2-PWR98 (Rosenkranz), N2-Self-Standard, CO2-Self-PWR93 (Rosenkranz), and CO2-Foreign-PWR93 (Rosenkranz). The carbon dioxide continua hardly contribute to the model spectra at all in the present environment.



## 5 Results and Comparisons

WaRAM2 has been recommissioned for atmospheric measurements at Mérida Atmospheric Research Station in December 2006. All measurements presented herein originate from this location. This chapter is concerned with instrument characteristics derived from these data, and sensor sensitivity. It also discusses the results from water vapour retrieval, and gives a comparison with correlative data.

### 5.1 Instrument Characterisation

WaRAM2 operation in 2007 has seen the recurrence of some earlier frequency stability issues. The frequency calibration procedure has been refined, but no major flaws could be identified. Therefore a degradation of the local oscillator is suspected to cause the instability. In addition, total-power calibrated spectra exhibit regions of seemingly enhanced noise at the line centre and towards higher frequencies, which turns out to result from disagreements between the odd and even spectrometer channel readings. This has motivated an investigation of the degree of non-linearity in the receiver. Since no direct linearity measurements can be carried out from remote, a novel measurement sequence is presented that depends on atmospheric signals and different settings of the programmable step attenuator instead.

This section also deals with the progress that has been made in baseline characterisation, which has already been considered a key problem in WaRAM2 retrieval by QUACK (2004). The surface of liquid nitrogen in the cold calibration load could be identified to be the dominating source of variability in standing waves on the spectra. Some numerical analyses of standing wave contamination are outlined, together with a discussion of how they are accounted for by the retrieval.

## 5.1.1 Frequency Stability

### Spectrometer

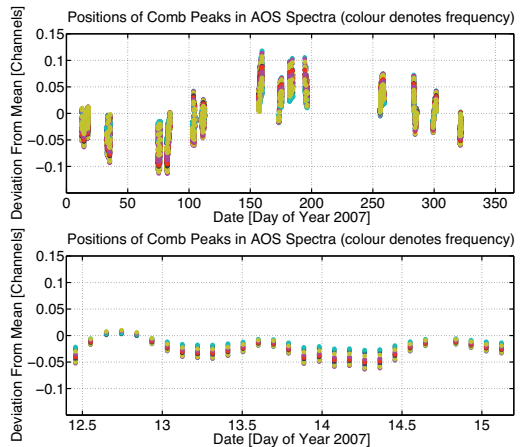
Fluctuations in the way the input frequencies are mapped to the AOS channels predominantly depend on mode hopping of the laser diode, which may be introduced by temperature or length variations in the laser resonator. Also the deflection angle of the BRAGG cell depends on temperature, albeit to a lower degree. A careful temperature stabilisation of the delicate parts leads to excellent frequency stability of the present spectrometer<sup>1</sup>, as reported in figure 5.1. In the complete ensemble of WaRAM2 measurements in 2007, the locations of the comb generator peaks vary by 0.2 channels at most, which is roughly equivalent to  $(139 \pm 5)$  kHz. Over the course of a few days, the stability is of the order of 0.05 channels, or  $(35 \pm 2)$  kHz.

### Local Oscillator

Despite the excellent stability of the spectrometer, the frequency calibrated data do not well match the line centre. Offsets occasionally amount to as

<sup>1</sup> The benefit of temperature stabilisation can most clearly be seen in comparison to data taken without, like during a WaRAM2 campaign to Schneefernerhaus, Zugspitze, Germany (QUACK, 2004).

Figure 5.1: (Upper panel) The detected positions of comb spectra peaks deviate only little from the mean of all measurements in 2007. Data for individual comb peaks are distinguished by colour. A comb spectrum comprises 13 such peaks, corresponding to signals at 1.5 – 2.7 GHz in 0.1 GHz intervals. Since the frequency grid for AOS spectra depends on calibration against comb spectra, data are plotted against AOS channel numbers here. See section 4.4 regarding derivation of fractions of channels. (Lower panel) Expanded view of a 48-hour portion of the measurements.



much as 2 channels. While Qpack allows retrieving for a frequency shift in the measured data, this has not so far been successfully set up for WaRAM2 data. The offset is instead matched by minimising the residuum between measured and synthesised spectra near the line centre, when introducing a manual shift to the ARTS/Qpack backend frequency grid. The time series of frequency offsets derived by this method is given in figure 5.2. The observed frequency shifts are roughly 100 times larger than expected when considering the inherent frequency stability for the local oscillator, which is specified as 1 ppm ( $\sim 20$  kHz). Given the large spread of the shifts about their mean, 0.85 MHz, this even holds true for assuming the mean to be a fixed offset from the specified local oscillator signal frequency. No clear indication can be obtained from the data to explain the cause of these offsets. To identify potential sources of this error, the calibration scheme for WaRAM2 raw data has been carefully reviewed and improved in the scope of this work (*cf.* section 4.4.1). The frequency is calibrated at higher accuracy now, yet no systematic flaws could be uncovered. In absence of other possible explanations, the frequency drifts must be attributed to malfunction of the local oscillator.

The local oscillator makes use of a phase-locked loop to maintain the stability of the output signal. Locking status can be queried from the device by use of a dedicated TTL line. In summer 2007, the sensor has been upgraded to monitor the locking status during operation, but the recorded data give no evidence for malfunction.

QUACK (2004) reports that unstable local oscillator operation also manifests in a significant increase in receiver noise temperature, and such has indeed occurred for measurements taken during six days in October 2007. Some of these data appear so distorted that the centre of the water vapour signature or even the overall line shape cannot unambiguously be identi-

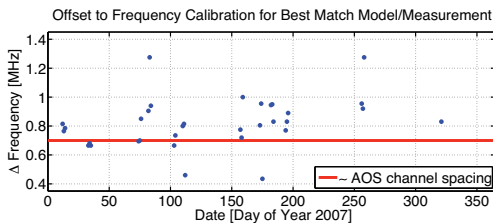


Figure 5.2: Frequency shifts that must be added to the individual frequency calibrations to achieve best match between modelled and measured spectra at the line centre. The red line indicates the spacing of two adjacent channels.

fied. The same conditions are observed for all nine days of measurement in 2008, with the exception of a couple of hours on January 20th. This might indicate some kind of degradation in the local oscillator. For the time being, the remaining data will be processed with a manual frequency adjustment if needed.

### 5.1.2 Spectrometer Resolution

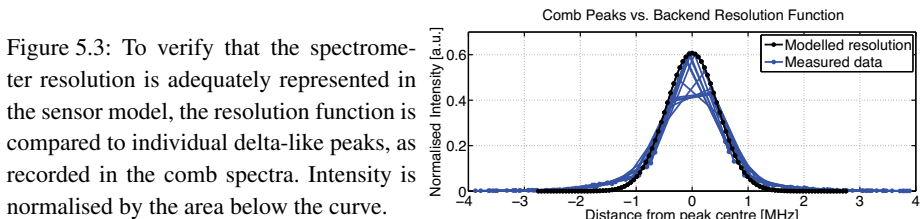
The resolution bandwidth of the spectrometer is reported as 1.1 MHz (SCHIEDER et al., 1989). The passband is modelled by a GAUSS distribution with 1.1 MHz FWHM. Figure 5.3 compares this to the intensity recorded at the comb spectra peaks. Since the line width of the comb generator signal is small compared to the spectrometer resolution bandwidth, the recorded signals allow approximating the spectrometer response function. The data confirm that the spectrometer resolution complies with the specification.

### 5.1.3 Linearity

Linear operation of the receiver is a crucial requirement to perform accurate measurements. To carry out linearity measurements on the WaRAM2 front-end, all components except for the horn antenna and the waveguide input isolator have been taken to our Bremen laboratory in November 2005. These measurements, of both individual components and the complete set-up, have been performed on a scalar network analyser<sup>2</sup>. Unfortunately the attached synthesised sweeper<sup>3</sup> only reaches up to 20 GHz, so the WaRAM2 front-end could not be characterised in its nominal input frequency range

<sup>2</sup> Hewlett Packard 8757C

<sup>3</sup> Hewlett Packard 83620A



(21.5 – 23.0GHz). Yet to get a hint about front-end fidelity, the band pass filters on both the input line and the local oscillator line have been removed and the local oscillator replaced with a signal generator<sup>4</sup> tuned to 17.6GHz, 10dBm. Measurements could then be performed at 19 – 20GHz input frequency, covering a considerable fraction of the designed IF range. Results could be read to a precision of  $\sim 0.5\%$  of the input signal. Within these error limits, and keeping in mind the restrictions of the test set-up, only limited information on linear operation of the front-end is available from these tests. A more sensitive method has thus been devised in this work based on measurements with the sensor in its regular laboratory set-up (*cf.* below).

Receiver linearity is put into question by the observation of some distortions in integrated atmospheric spectra. It is found that the noise is not adequately reduced in certain regions, including the line centre, as is demonstrated in figure 5.4. More thorough inspection of these spectra uncovers a systematic deviation of the power levels indicated in the odd and even spectrometer channels, shown in figure 5.5. The relation to spectrometer channels excludes the front-end from causing this particular type of effect, as it has no component that could generate such an effect. The spectrometer, on the other hand, features two distinct amplifier circuits to readout the odd and even CCD pixels (G HOCHSCHILD, IMK, FZ Karlsruhe, pers. corr.). This design is found frequently in AOS units and typically results in a small "ripple" offset being present in the dark current ("zero") readouts of adjacent channels. Yet the deviations reported here cannot arise from these offsets, since if they did, they would necessarily cancel out in a total-power calibration. Their presence hence indicates some type of non-linearity in the even or odd channels, or both, and indeed calls into question the linearity of the spectrometer as a whole.

However the overall magnitude of these artefacts is small. They have gone unnoticed over years of observations of the much stronger ozone signature at 273 GHz, which is observed at a higher noise level with MIRA-2. To alleviate the ambiguity in WaRAM2 measurements, only the odd spectrometer channel readings shall be used when retrieving water vapour profiles. It has

---

4 Rohde & Schwarz SMR 20

Figure 5.4: WaRAM2 power calibrated spectra exhibit regions of seemingly enhanced noise at the line centre and right wing.

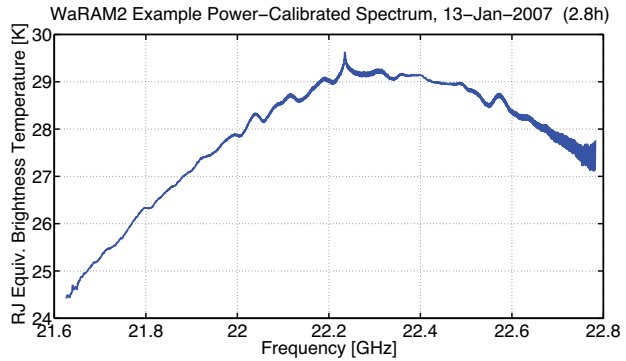
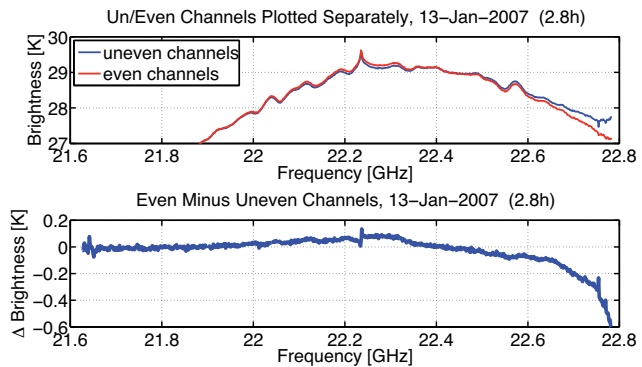


Figure 5.5: (Upper panel) A separated plot of odd and even spectrometer channels shows that the fluctuations displayed in figure 5.4 are in fact caused by systematic deviations between these ensembles. (Lower panel) An example of the residuum when taking the spectrum of even channels minus the spectrum of odd channels. Data are plotted at the frequencies of the odd channels.



nevertheless been attempted to gather more information about this issue using signals provided by the WaRAM2 front-end.

A basic investigation of receiver linearity involves observing a reproducible relative change in input signal at different power levels, regardless of the total power level. A linear sensor should always record the same relative change in input signal. Now given a suitably rapid measurement sequence, the sky qualifies as input signal when observed under two distinct elevation angles. This is based on the assumption that the sensor characteristics do not change when observing the sky at different elevation angles, which is indeed required for proper sensor operation, but may not be tested by the procedure

proposed here.<sup>5</sup> By help of a programmable step attenuator that is part of the spectrometer, the total power level may be varied.

Figure 5.6 illustrates a measurement sequence that has been obtained to test this idea. The programmable step attenuator is configured to consecutive values  $\in \{3 \text{ dB} \dots 9 \text{ dB}\}$ <sup>6</sup>, and for each setting, a 1 s observation of the sky at  $8^\circ$  and  $46^\circ$  is performed. The zero-corrected<sup>7</sup> raw spectra are henceforth denoted by  $C_8$  and  $C_{46}$ . They are functions of frequency  $\nu$ , time  $t$ , and IF attenuation  $Y$ , without explicitly considering this in their notation here.

The relative change in input signal is adequately represented by the channel-wise ratios  $C_8/C_{46}$  at fixed  $t$  and  $Y$ . In case of negligible atmospheric variation when collecting the data, two consecutive such ratios would be identical in a linear receiver. Example ratio spectra are given in the lower panel of figure 5.6. They show some resemblance to the 22 GHz water vapour signature, which is indeed expected due to the different intersection of the antenna beam with the atmosphere at different elevation angles. Yet the ratios differ in overall magnitude and exhibit significant deviations from the expected shape. Different magnitudes may result from atmospheric variability, which can be ruled out as discussed below. Deviations from expected line shape may readily be attributed to the variation of receiver noise temperature with observation frequency, since the contribution from receiver noise is still present in the data analysed here. It may however also indicate a receiver non-linearity, though its origin (front-end, spectrometer, or both) cannot be deduced from the present measurements.

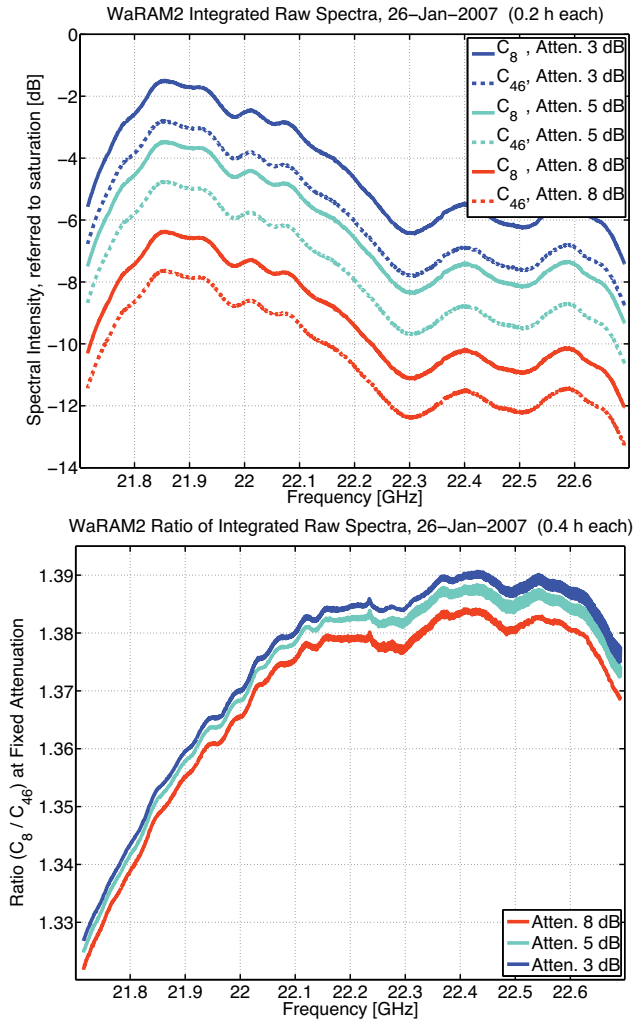
The deviations in shape roughly correspond to gradients in the raw spectra, which on their part indicate bad impedance matching on the transmission line from the antenna to the spectrometer. No such problems have been present in the scalar network analyser measurements discussed at the beginning of this subsection, and they are suspected to originate in the link from the front-end to the spectrometer. It catches the eye that almost the same gradients in spectral power apply to the comb spectra (*cf.* figure 4.3), but no further analysis is possible from remote. The problems can only be over-

<sup>5</sup> Antennas that do not operate to specification, as brought up in section 4.3.1, form an obvious scenario for the sensor characteristics to change with the position of the revolvable mirror, if part of the main lobe is spilling out of the optical guidance.

<sup>6</sup> Part of the spectrum is saturated at attenuation less than 3 dB.

<sup>7</sup> *cf.* section 4.3.4.

Figure 5.6: (Upper panel) Zero-corrected raw spectra taken at different elevation angles into the sky. Colour denotes different settings of the programmable step attenuator. Individual spectra are recorded in 1 s. The plotted spectra each correspond to the mean of 681 such measurements. (Lower panel) Ratios of the zero-corrected spectra at  $8^\circ$  and  $46^\circ$  elevation angle. Colour again denotes setting of the programmable attenuator. Individual ratios comprise two 1 s measurements, and again the mean of 681 such ratios is presented in one spectrum. See body text for discussion.



come by proper tuning of the IF chain, but again lack of access to the sensor prohibited such action in the scope of this work.

The mismatch between odd and even channels is also clearly visible in the  $C_8/C_{46}$  ratio spectra. Recalling figure 5.5 (lower panel), the total-power calibrated spectrum shows a small region around 22.4 GHz where deviations between odd and even channels effectively cancel out. Quite surprisingly,

this is not the case for the ratio spectra  $C_8/C_{46}$  given here. This will be considered in short at the end of this subsection.

To check if the measurement sequence is rapid enough to allow the assumption of atmospheric stability, the evolution of the input signal over time must be inspected. To this end, the individual mean ratios are plotted against time in figure 5.7 (upper panel). The data indicate some variability,

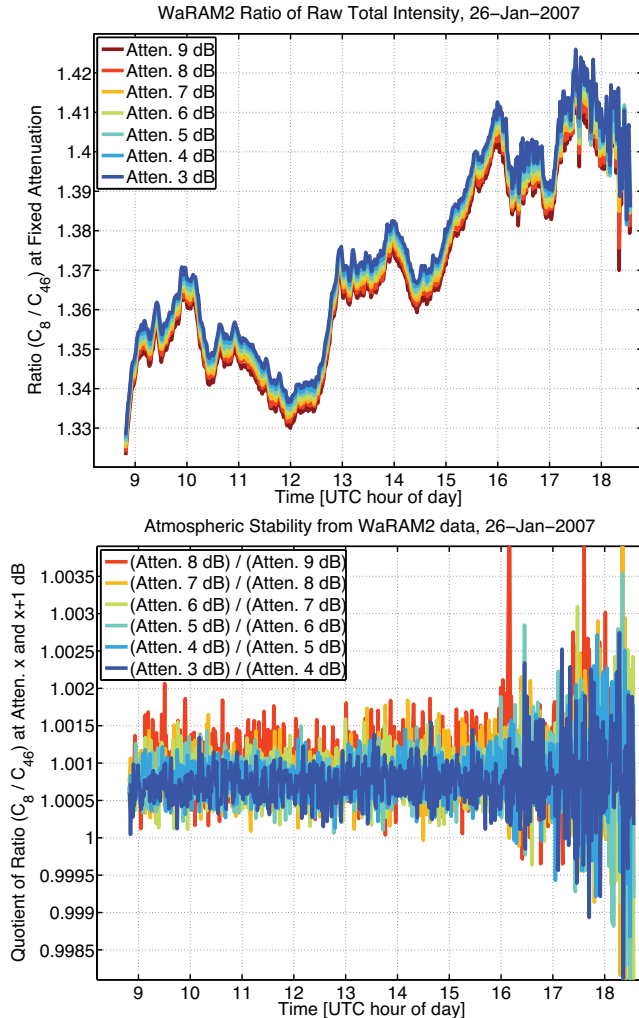


Figure 5.7: (Upper panel) For each single pair of measurements at  $8^\circ$  and  $46^\circ$  elevation (*cf.* figure 5.6), the mean of  $C_8/C_{46}$  is plotted. (Lower panel) For every consecutive pair of ratio data (*cf.* above) the quotient is computed. Absence of a trend in these data indicates that measurements are taken rapidly enough to not be affected by atmospheric variability. See body text for discussion.

the largest being observed between 12:30 and 13:00 UTC with mean ratios rising by  $\sim 2.5\%$  (ratio  $1.34 \rightarrow 1.375$  at 3 dB attenuation). Nevertheless, the data appear stably stacked, which suggests adequacy of the measurement sequence timing to not be affected by atmospheric variability. The picture becomes clearer when plotting the quotients of consecutive ratios (lower panel), whose variability is less than  $0.5\%$  up to 16:00 UTC. After this time, considerably more variability is found. This is due to convection of moist air from lower altitudes, which is driven by solar heating (the local time zone is UTC  $- 4$ h, apparent solar time is 4.7h behind UTC on average). It effects a characteristic diurnal cycle of tropospheric background temperature, as illustrated by figure 4.6 (left panel) with respect to averaging over atmospheric spectra. Around noon, the associated variations become more rapid than the measurement sequence described here, and our initial assumption about atmospheric stability breaks down. Hence later data are exempted from further analysis. All data before 16:00 UTC lie above unity, their individual means amounting to  $\sim 1.008$ . This clearly excludes to explain the effect by changes in the atmospheric signal.<sup>8</sup> Suitability of the data for linearity assessment has thus been established, at least up to 16:00 UTC.

To investigate if the data allow quantitatively inferring the degree of non-linearity, the results are displayed with respect to frequency in figure 5.8 (upper panel). Large variability between adjacent channels illustrates the deviation between odd and even spectrometer channels. Despite accounting for this effect, the variability appears too large and the data too discontinuous with respect to incident power to allow deriving exactly the non-linearity in the receiver. The lower panel correlates the observed non-linearity to colour-coded saturation degree, expressed as  $C_8 - C_{46}$ , of the spectrometer channel. It presents weak support for the statement that a lower saturation introduces larger non-linearity, which is due to larger contribution of differential non-linearity in the analogue/digital converters (KRUPA, 1998). The lower saturation also exhibits considerably larger variability, as is expected from the loss in precision.

Eventually a look can be taken at the deviation between odd and even channels in the quotient data. To this end, the odd channel quotients are di-

---

<sup>8</sup> If the ratio of atmospheric signal from  $8^\circ$  and  $46^\circ$  elevation really lowered by  $0.8\%$  every 2s, both signals would have to be the same at the end of the day.

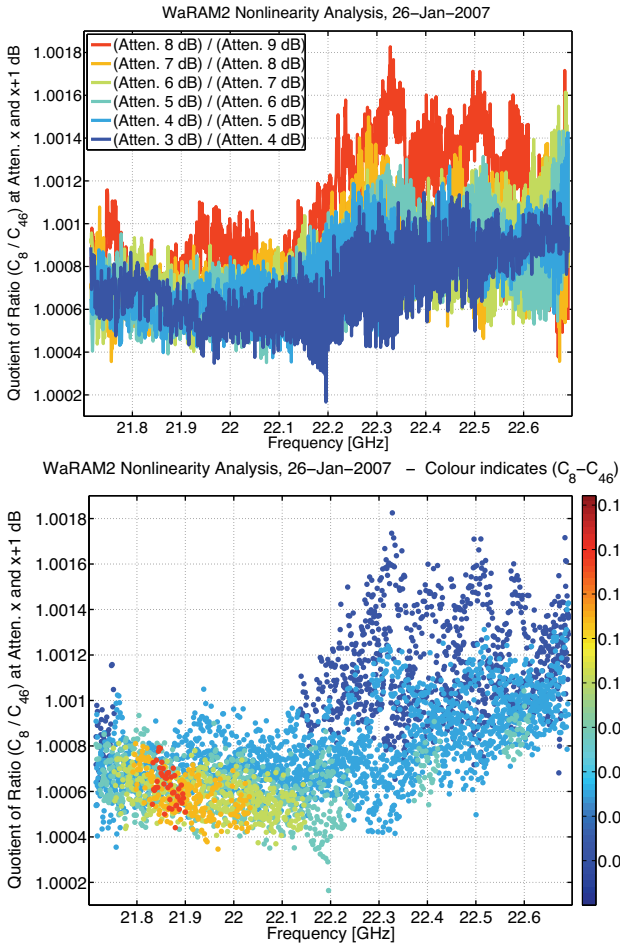


Figure 5.8: (Upper panel) Channel-wise quotients of the ratio data presented in figure 5.6 (lower panel). See the legend for programmable attenuator setting in each quotient calculation. Deviation to larger values means that at lower power levels, the ratio  $C_8/C_{46}$  becomes smaller. In a linear receiver, all data should be unity, except for measurement noise. (Lower panel) Same as above, but colour instead indicates saturation degree, expressed as  $C_8 - C_{46}$ , of the corresponding spectrometer channel.

vided by their even channel counterparts. After taking the mean over time of the resulting spectra, noise is further reduced by collecting the data into 10 channel wide bins. The complete analysis is displayed in figure 5.9. As is expected from the initial observations presented in this subsection, the deviation attains some of its largest values at the centre of the observed water vapour signature. From the line centre to higher frequencies, the deviations attain larger magnitude, both with respect to frequency and attenuator setting. The largest deviations amount to about 0.4‰; below 22.0GHz, data

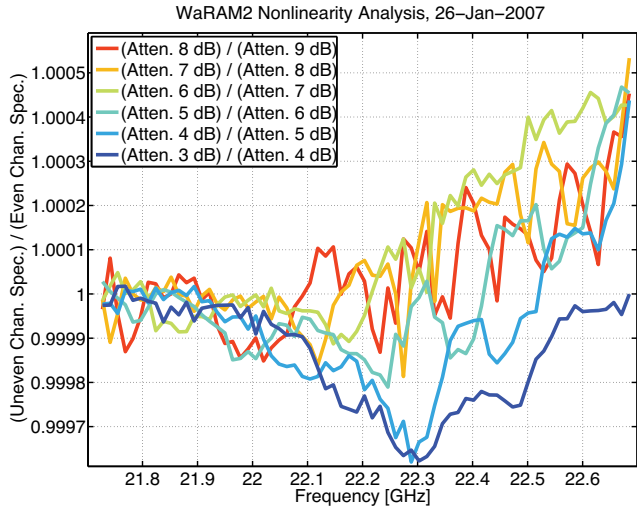


Figure 5.9: Quotient data (*cf.* figure 5.8) from odd spectrometer channels divided by data from even spectrometer channels. Individual spectra are averaged over time, and the result collected into 10 channel wide bins. See body text for discussion.

for individual attenuator settings range within 0.1‰ of the mean. The plot does not indicate a preferential attenuator setting to alleviate the odd/even channel mismatch at the line centre, which is partly due to the large gradient in spectral power recorded around the line centre. It is possible for the mismatch effects to cancel out, as has accidentally been found in the vicinity of 22.4GHz. This region appears free of the artefacts discussed here when total-power calibrated (*cf.* figure 5.4), but exhibits considerable artefacts in relative "calibration" (*cf.* figure 5.6).

Mapping of observation frequencies to spectrometer channels is done in hardware, so it neither was possible from remote to alleviate the issues at the line centre by assigning it to supposedly better spectrometer channels. This option may only be checked by an operator who has direct access to the instrument. It involves to replace the LO with a signal generator, to mix the atmospheric signal at other frequencies.

### 5.1.4 Baseline

The term "baseline" denotes how the power spectra measured by a microwave radiometer deviate from the actual atmospheric signal. Such deviations arise from a variety of instrumental effects, e.g. from non-linearity

like discussed above. One can significantly reduce the error introduced by non-linearity by operating the receiver in a reference beam mode (KLEIN, 1993). Yet in case of the water vapour signature at 22 GHz, this approach is hampered by the large spectral width of the water vapour signal (*cf.* section 4.5). Still all receivers presented in table 3.2, with the exception of MIRA-5, WASPAM and the two WaRAMs, are operated in reference beam calibration, a design choice taken because the signal from the middle atmosphere is rarely larger than a few tenths of a degree. LANGER (1995) has thoroughly investigated how the baseline is affected by the receiver's sensitivity to the mirror sideband and sidebands of higher order<sup>9</sup>. Further baseline effects are introduced by the presence of undesired weak resonators in the quasi-optical set-up (*cf.* section 4.3.1). Some of the standing waves in WaRAM2 spectra, which arise from these resonators, adversely affect retrieval, as will be discussed below.

Figure 5.10 demonstrates some typical 4.5 s total-power calibrated measurement by WaRAM2, and the result of a 3 h integration. The presence of standing waves is clearly visible in both spectra, as is the benefit of the PLM averaging out the modulation. Yet the eye is immediately caught by the elimination of standing waves in the integrated spectra (right panel), regardless of PLM operation. This is due to the strongest resonator in the receiver being formed between the antenna and the liquid nitrogen surface in the cold calibration load. The optical path between the antenna and the liquid surface extends as nitrogen evaporates, which introduces an effect similar to a PLM. The extension in resonator length induces variations in the observed modulation, *cf.* equation (4.2), like

$$\Delta I_{\text{tr}}(\nu, t) \propto \cos\left(2\pi \frac{2 [d_0 + \Delta d(t)] \nu}{c}\right). \quad (5.1)$$

$d_0, \Delta d(t)$  denote initial distance between reflective elements and extension after time  $t$ . Since  $\Delta d(t) \ll d_0$  and  $\Delta d(t) \Delta \nu / c \ll 1$  for the frequency range discussed here, the cosine argument in equation (5.1) may be approximated as

$$\frac{2 [d_0 + \Delta d(t)] \nu}{c} \approx \frac{2 \nu d_0}{c} + \frac{2 \nu_{\text{H}_2\text{O}} \Delta d(t)}{c} \approx \frac{2 \nu d_0}{c} + \frac{\Delta d(t)}{6.75 \cdot 10^{-3} \text{ m}}.$$

<sup>9</sup> A sideband of higher order denotes heterodyne conversion at multiples of the local oscillator frequency.

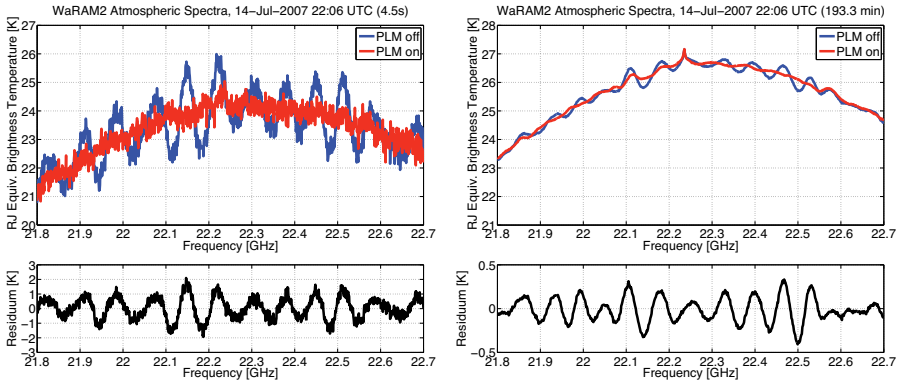


Figure 5.10: (Left panels) Two 4.5s total-power calibrated measurement cycles by WaRAM2 present how standing wave modulations may be averaged out by proper configuration of the PLM. The residuum (original minus less distorted spectrum) is given in black below. (Right panels) Same as before, but demonstrated for the result of a 3h integration. Standing waves in the measurement without path length modulation are reduced, because the strongest resonator includes the liquid nitrogen surface, so it grows in extent as nitrogen evaporates.

Thus it becomes clear that the extension in resonator length essentially introduces a “phase shift” in the associated standing wave. When the cold calibration load is refilled with liquid nitrogen, the level initially amounts to  $(3.0 \pm 0.2) \cdot 10^{-1}$  m, and the nitrogen completely boils off in  $(75 \pm 3)$  h. This yields a resonator expansion rate of  $(4.0 \pm 0.4) \cdot 10^{-3}$  m h<sup>-1</sup>, and the “phase shift” introduced by this expansion covers an entire period in about  $(6.75/4.0)$  h = 1.7 h. In other words, spectra must be averaged over several hours to observe PLM-like elimination of standing waves. A PLM of course operates at a much higher frequency. Since it is intended to average out standing waves on individual spectra, the associated “phase shift” must cover an entire period multiple times during the capture time for an individual raw spectrum.

A closer inspection of figure 5.10 indicates that the residual modulation in the integrated spectra still is of the same order of magnitude as the stratospheric signal. Before attempting a retrieval, further steps are taken to reduce the standing waves. A common approach is to reduce the quality of the undesired resonators by tilting the involved reflectors. A similar effect

may be attained in WaRAM2 by observing the cold calibration load at an oblique angle, which is feasible because of the large opening of the DEWAR vessel, and the beam waist being located inside the DEWAR. Best results have experimentally been obtained for tilting the beam by  $6^\circ$ . Figures 5.11–5.14 present some comparisons of either configuration. The figure captions

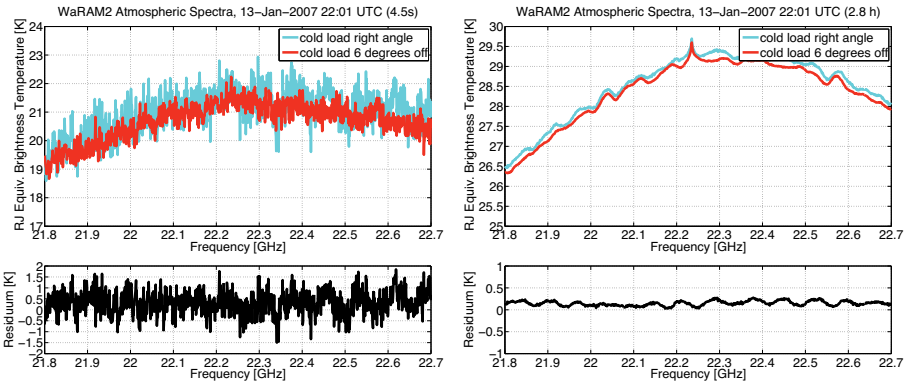


Figure 5.11: (Left panels) Two 4.5s total-power calibrated measurement cycles by WaRAM2, with the PLM turned on, are plotted, observing the cold calibration load at different angles. The residuum (original minus less distorted spectrum) is given in black below. (Right panels) Same as before, but for a 3h integration.

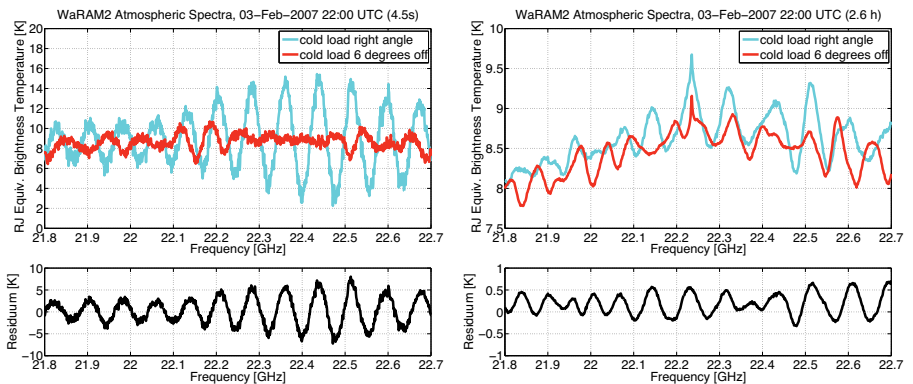


Figure 5.12: See figure 5.11 for general description. The PLM is off.

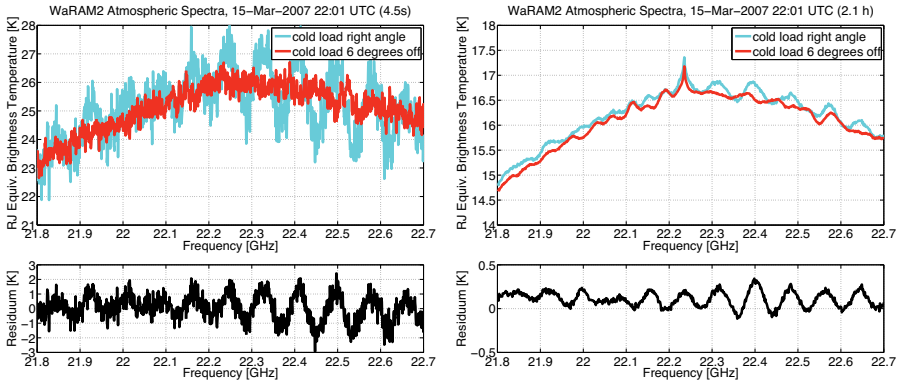


Figure 5.13: See figure 5.11 for general description. The PLM is on.

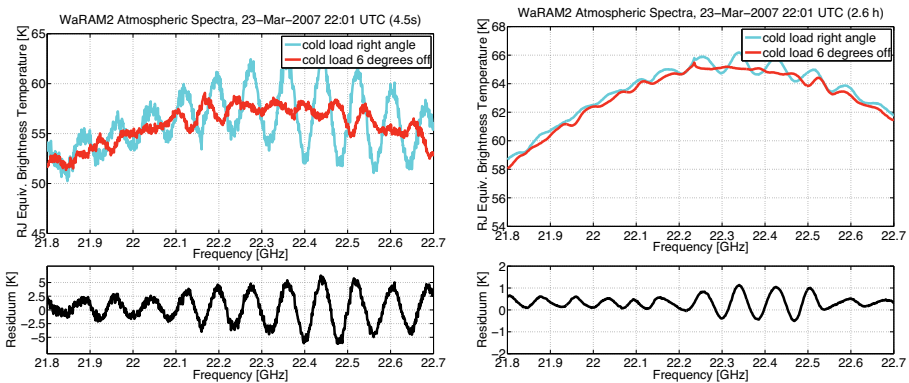


Figure 5.14: See figure 5.11 for general description. The PLM is off. The difference in magnitude of the standing waves results from the atmospheric signal being closer to the cold calibration load signal.

tell whether the PLM was turned on or off in the individual measurements. The data exhibit a striking degree of variability in the magnitude of standing waves, which is associated to the tropospheric background: For a smaller background, the atmospheric signal is further away from the two calibration points in total power calibration, equation (4.5), which causes all deviations of the cold load signal in particular to be amplified. This is a severe concern

since a small tropospheric background is a favourable condition for observations of the weak stratospheric signal.

The residuals presented in figures 5.11–5.14 indicate that atmospheric brightness temperatures derived from calibration against  $6^\circ$  tilted view of the cold load are systematically lower than at right angle. This is because a higher radiance is received from the cold load in the tilted configuration. Recalling the intensity transmitted by a FABRY-PÉROT type resonator, equation (4.2),

$$\frac{I_{\text{tr}}}{I_0} = 1 - r_1^2 - r_2^2 + 2r_1 r_2 \cos(2\delta) + \dots,$$

there is not only a modulation of the transmitted intensity with frequency, but also intensity removed from the original signal according to terms  $-r_1^2$  and  $-r_2^2$ . Regarding reflections at the antenna, these apply to all signal paths in the same way. However the reflectance of the liquid nitrogen surface introduces a systematic offset, because it only occurs in the cold load signal path. Yet at the same time it injects a signal from outside the cold load, presumably at room temperature, increasing the radiance received from the cold load. The result of these opposing effects has not been numerically established so far. Instead the systematic error in radiance received from the cold calibration load is approximated by a method described in section 5.2.1 below.

The difficulties in eliminating standing waves from WaRAM2 spectra have initially been attributed to the most pronounced modulation not being fixed in frequency space. The data have not allowed deciding if this variability resulted from phase shifts in standing waves or changes in periodicity (QUACK, 2004). The discussion of equation (5.1) above establishes how both notions relate to each other. Since phase shifts in standing waves can not be explained by the physical models discussed here, the case has been hardened for a variable length resonator being present in the system, which has eventually been identified between the antenna and the liquid nitrogen surface. HOFFMANN (2008) has verified this finding by help of a basic numerical experiment. He also discusses a long-periodic standing wave, which only shows up in WaRAM measurements at Ny-Ålesund, where it has blocked hitherto efforts to establish a proper retrieval of stratospheric information.

The evolution of variable standing waves is hard to track in the data, as

they average out when averaging the individual spectra. Figure 5.15 illustrates a method that has been conceived as part of the present work to extract such information from the data. It involves relating the cold load spectra, which contain the standing wave of interest, to a reference signal, in this case provided by the hot calibration load. The instrumental Y-factor spectra, obtained from channel-wise evaluation of  $C_{\text{HOT}}/C_{\text{COLD}}$ , present such a re-

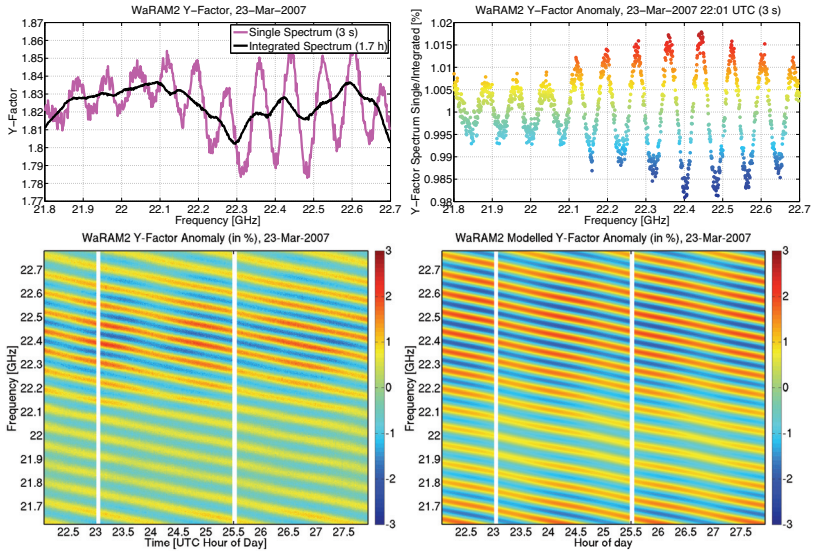


Figure 5.15: (Upper left) The spectral characteristic of the instrumental Y-factors hampers direct discussion of standing wave evolution over time based on individual spectra. However, if integrating long enough, the standing wave contribution averages out. (Upper right) The spectral characteristic is removed from the individual spectrum presented on the left by dividing it, channel-by-channel, by the mean Y-factor spectrum. This result is herein referred to as "Y-factor anomaly". The magnitude is coded in the same colours as in the bottom panels. (Bottom left) With the magnitude of the Y-factor anomaly coded in colour, the spectra are now plotted versus time. This allows to readily assess the evolution of standing waves in the measurements. (Bottom right) The Y-factor anomaly evolution on the left has been approximated by three individual resonators,  $d_{0,1} = 1.738$  m,  $d_{0,2} = 1.878$  m,  $\Delta d_1 = \Delta d_2 = 3.9 \cdot 10^{-3}$  m h $^{-1}$ , and  $d_{0,3} = 1.900$  m (fixed). The intensity of the modulation from the first resonator is 35% compared to the second resonator, from the third resonator it is 10%.

lation, but their spectral characteristic still limits their value. This effect can be reduced by dividing with the mean Y-factor spectrum over time, which takes advantage of the fact that the liquid nitrogen standing wave tends to average out. The resultant "Y-factor anomaly" is now mostly carrying information about standing wave variations with time, which can readily be visualised.

The beats in figure 5.15 (lower left panel) uncover that more than one resonator varying with time must be present in the system. The lower right panel presents an attempt to emulate this by a superposition of standing waves from three individual resonators. Numerical input for the emulation has been obtained from analysis of equation (5.1),

$$\Delta I_{\text{tr}}(\nu, t) \propto \cos \left( 2\pi \frac{2 [d_0 + \Delta d(t)] \nu}{c} \right).$$

The resonator expansion rate,  $m = \partial \Delta d / \partial t$ , is constant<sup>10</sup>, so we can write  $\Delta d(t) = mt$ . The second summand of the cosine argument thus yields a relation between  $m$  and the number of standing wave periods  $N_\nu$  per time  $T$  that are observed at a given frequency,  $\nu$ , corresponding to a single spectrometer channel,

$$2\pi N_\nu = 2\pi \cdot \frac{2\nu}{c} \cdot mT \implies m = \frac{cN_\nu}{2\nu T}.$$

$N_\nu$  may be obtained by a discrete FOURIER analysis of data from any single channel.  $m$  may be evaluated at higher accuracy by combining the results for all individual channels. The FOURIER analysis can further be exploited, since the phase angles obtained must be equal to the first summand of the cosine argument modulo  $2\pi$ ,

$$\varphi(\nu) = \left( 2\pi \cdot \frac{\nu}{c} \cdot 2d_0 \right) \bmod 2\pi.$$

The discontinuities in  $\varphi(\nu)$  can be overcome by seeking locations  $\nu_l$  where  $|\varphi(\nu_l) - \varphi(\nu_{l+1})| > 2\pi$ , and accordingly adding or subtracting  $2\pi$  to  $\varphi(\nu)$  at  $\nu_{l+1}$  and all following locations. Solving for  $d_0$  then yields a multitude of individual solutions like

$$d_0 = \frac{\varphi(\nu_2) - \varphi(\nu_1)}{4\pi} \cdot \frac{c}{\nu_2 - \nu_1},$$

---

<sup>10</sup> Nitrogen evaporates at a constant rate, when temperature inside the DEWAR has stabilised, and the DEWAR is of cylinder shape.

or alternatively allows a least squares fit of  $d_0$  as the slope of  $\varphi(v)$  with respect to  $v$ .

The data used in the emulated standing wave superposition in figure 5.15 (lower right panel) correspond to three resonators, two of variable length and one of fixed length. The variable resonators span between the liquid nitrogen surface on one side and different parts of the antenna on the other. The resonator expansion rate matches what is expected from the evaporation rate of liquid nitrogen. The third resonator forms between the antenna aperture and the liquid nitrogen DEWAR bottom. This analysis provides valuable qualitative insight about the front-end elements involved in standing wave generation. It has been attempted to numerically correct for standing waves described by these parameters in total-power calibration, yet unsuccessful. Hence standing wave modulations remaining on integrated atmospheric spectra must numerically be accounted for in the retrieval.

With respect to WaRAM(2) data, QUACK (2004) has already described that the quality of results depends critically on proper treatment of standing waves. In his approach, the presence of long-periodic modulations in the spectra has prevented the use of the full 1 GHz bandwidth data in the retrieval. An 0.1 GHz interval around the line centre is considered instead. The spectra are pre-processed according to a two-layer model of the atmosphere, *cf.* section 4.5, which involves subtracting tropospheric background and a slope, followed by scaling to correct for tropospheric signal attenuation. After pre-processing, the spectra correspond to a measurement taken at tropopause level.

Standing waves are iteratively eliminated from these data by taking the following steps: A first retrieval is performed. The periodicity of the strongest wave is then identified by a FOURIER analysis of the residuum. A synthesised wave of the same periodicity is manually fitted to the residuum, and subtracted from the spectrum that is input to the next iteration of the retrieval. After four repetitions, the iteration is stopped. It would in principle be possible to replace this iteration by having the retrieval fit amplitudes and phases of fixed-periodicity standing waves, following an extension to the optimal estimation method by KUNTZ et al. (1997). However QUACK (2004) reports that use of this extension results in a loss of information from the measurement, as expressed by the retrieval effectively being constrained to *a priori* values. On the other hand the results obtained from an iterative

retrieval, as described above, exhibit oscillations when compared to FAS-COD tropical water vapour and a mean profile from UARS/HALOE. These can most likely be explained by inadequately constrained retrieval, as introduced by an incomplete correction for standing waves.

In the context of the present work, considerable additional effort has been expended in finding an adequate representation of standing wave artefacts. Since no long-periodic standing waves could be detected in WaRAM2 data since December 2006, the retrieval is now carried out using the data over the full 1 GHz bandwidth. This also benefits the lower altitude limit of WaRAM2. Regarding elimination of standing waves, the KUNTZ et al. (1997) method is adopted, which is by default provided for in ARTS/Qpack. Standing waves are identified in a similar manner to the iterative approach taken above. The method is presented in more detail by KOPP (2000). It comprises a strongly regularised retrieval<sup>11</sup> from the uncorrected spectrum, followed by iterative discrete FOURIER transforms of the residuum and subtraction of the strongest wave from the residuum. As stated by KOPP (2000), it is not feasible to instantaneously deduce all periodicities from a single FOURIER spectrum: Due to the finite bandwidth of the original spectrum, the FOURIER spectrum maxima are spread out similar to  $\text{sinc}^2(x)$ . This may affect the locations in particular of the smaller maxima in the FOURIER spectrum, hence they are extracted one-by-one. To limit the loss of information due to the standing wave fit, as described above, the number of standing waves considered in this approach has initially been limited to four. However it turns out that the kind of oscillations on the retrieved H<sub>2</sub>O profiles observed above persist under this condition. A major breakthrough has been obtained when attempting to more completely capture the standing waves on the spectra, by increasing their number to 20 in the final retrieval.

Figure 5.16 demonstrates this method for a measurement carried out on February 2, 2007. The corrected spectrum indicates that despite minor modulations still present, a considerable improvement in detecting the water vapour line is obtained. The total correction from the fit, plotted in the lower left panel, does not appear as if a signal from the line centre were captured by

---

<sup>11</sup> A strongly regularised retrieval forces the result to the *a priori* information while extracting less information from the measurement. Without this, the retrieval rarely converges for the uncorrected spectra.

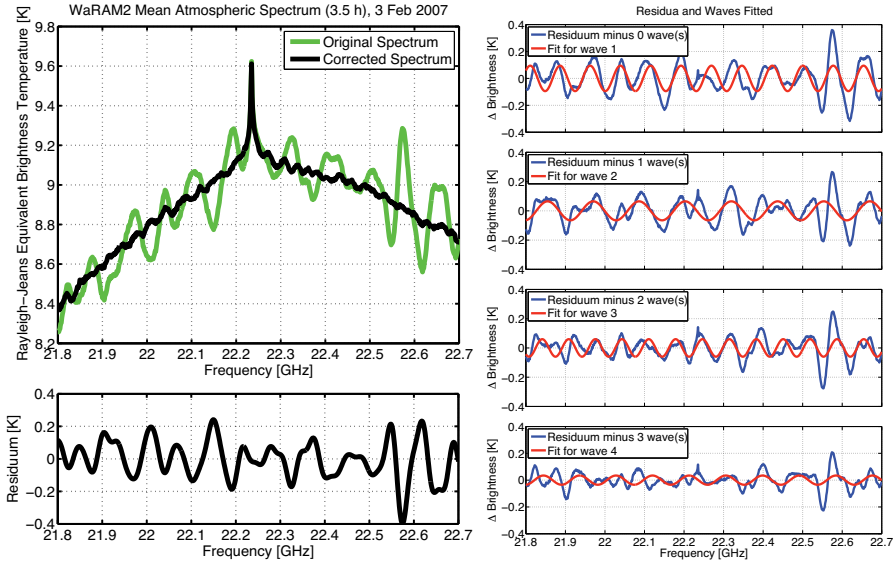


Figure 5.16: (Left column) The upper panel displays an example of an uncorrected atmospheric spectrum and the result after fitting 20 standing waves, according to the approach taken in the present work. The lower panel plots the total correction from the fit. (Right column) Individual plots of the residua (blue) after fitting 0, 1, 2, and 3 waves, complemented by a synthesised wave (red) corresponding to the strongest signal in the FOURIER spectrum of the respective residuum.

the linear combination of standing waves. Concluding remarks about measurement information being cancelled out by the fit of standing waves will be given in the discussion of averaging kernels in the next section. Note that corrected spectra as given in figure 5.16 are by-products of the search for standing wave periodicities. Only the resulting periodicities are used in actual retrievals of geophysical parameters, along with the uncorrected atmospheric spectra. The retrieval may assign different amplitudes and phases to the fixed periodicities, so standing wave corrections in the final results may differ from the one presented here.

### 5.1.5 Synthetic Retrieval

In order to explore the sensitivity attainable with the WaRAM2 sensor, a numerical experiment is carried out. Recalling the discussion in section 2.3 about current challenges in (stratospheric) water vapour observations, this experiment is chosen to shed first light on the sensor's fundamental capability to capture the atmospheric tape-recorder signal. Figure 5.17 presents lower stratospheric  $\text{H}_2\text{O}$  abundance as derived from HALOE measurements, zonal average over the latitude band  $12^\circ\text{N}$ – $12^\circ\text{S}$ , based on MOTE et al. (1995). These data give a representative idea about the magnitude of the tape recorder signal, but since they are originally given as  $\text{H}_2\text{O} + 2\text{CH}_4$ , methane levels had to be subtracted, which has been done according to methane derived from HALOE (BRASSEUR et al., 1999). In a nutshell, the numerical experiment comprises calculating artificial spectra at 22 GHz from these data, retrieving  $\text{H}_2\text{O}$  profiles from the artificial spectra, and comparing results to input.

Artificial spectra are calculated from HALOE water vapour results using the WaRAM2 forward and sensor models. The forward calculation stretches across a larger atmospheric region than covered by the HALOE data used here, they are therefore blended with the WaRAM2 *a priori* water vapour profile<sup>12</sup>. White GAUSSIAN noise is added to the artificial spectra, with a

<sup>12</sup> Blending in this case means that to each end of the HALOE profile, the difference is taken with *a priori* VMR four pressure levels further up or down. At the three intermediate pressure levels, VMR in the blended profile is configured to cover 25%, 50%, and 75% of this difference, respectively.

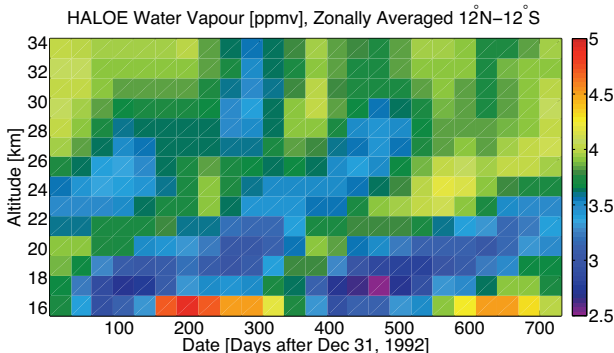


Figure 5.17: Tropical lower stratospheric  $\text{H}_2\text{O}$  abundance from HALOE data, zonal average  $12^\circ\text{N}$ – $12^\circ\text{S}$ .

standard deviation corresponding to a 24 hours of atmospheric observations with WaRAM2. This is the maximum time that can be obtained with a single refill of the cold calibration load with liquid nitrogen.<sup>13</sup>

Water vapour abundance is retrieved from the artificial spectra using a basic WaRAM2 sensor model, and the results are given in figure 5.18. Baseline artefacts are not considered, like offset, slope, or periodical signals, since no such effects have been included when calculating the artificial spectra. The results thus give an indication about the ultimate sensitivity in absence of detrimental effects, or provided complete knowledge of all baseline effects. They appear much less detailed than the HALOE data, which comes as no surprise given the coarse vertical resolution of ground-based microwave retrieval. At upper altitude levels, H<sub>2</sub>O abundance is over-estimated compared to original HALOE levels. This is consistent with forcing by the WaRAM2 *a priori*, which is about 1 ppmv larger than the HALOE data at the upper altitude limit used here.

At first sight, the retrieval from the artificial spectra does not seem to reproduce the tape-recorder signal. Yet taking into account vertical resolution, a more adequate representation of the data must be chosen — the six altitude levels given by the checkerboard plot above correspond to the pressure grid for retrieval, but yield little more than one independent piece of information (*cf.* RODGERS, 2000). Hence figure 5.19 chooses a single altitude level to compare HALOE data with the retrieval from artificial spectra. This compar-

<sup>13</sup> The nitrogen takes about 2 days to evaporate, but about half of the measurement time is required for calibration.

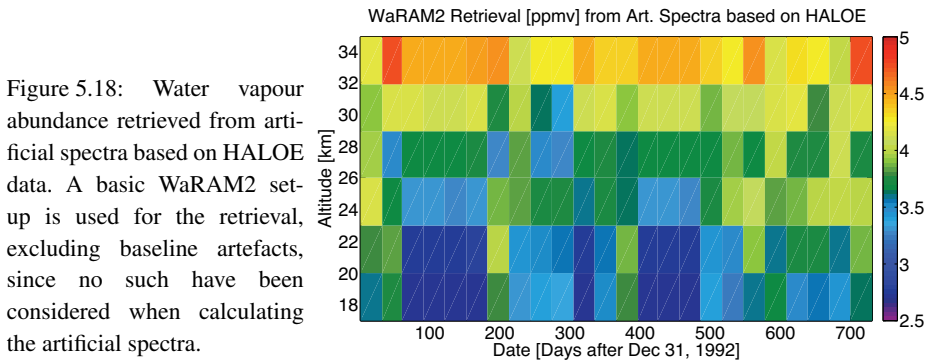


Figure 5.18: Water vapour abundance retrieved from artificial spectra based on HALOE data. A basic WaRAM2 set-up is used for the retrieval, excluding baseline artefacts, since no such have been considered when calculating the artificial spectra.

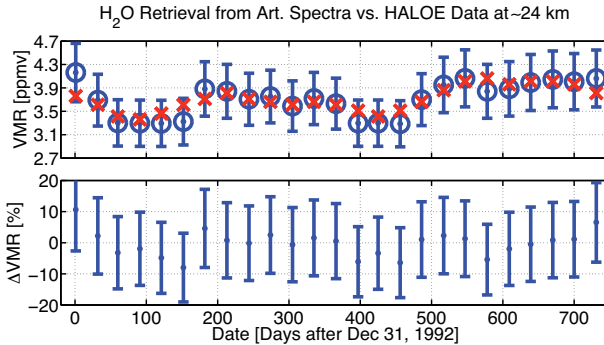


Figure 5.19: (Upper panel) Blue markers denote water vapour VMR at  $\sim 24$  km as retrieved from artificial spectra based on HALOE results. Error bars indicate total retrieval error. Measurement noise on the artificial spectra corresponds to a 24-hour integration of atmospheric signal with WaRAM2. Red crosses give water vapour VMR at the same altitude from the original HALOE results. (Lower panel) The plot presents the same data as above, but expressed as relative deviation of the retrieved VMR from the corresponding HALOE value.

ison is carried out at the lowest altitude accessible by WaRAM2,  $\sim 24$  km, that is commonly found in ground-based observations at 22 GHz.

The new representation bears much more evidence for a signal akin to the seasonal cycle in water vapour entering the stratosphere, and retrieved data match HALOE mostly well within the error bounds. This gives an initial indication of the general suitability of WaRAM2 retrieval to observe the tape-recorder signal. To obtain further significant information, a considerable refinement of the numerical experiment would be desirable, but is set aside in favour of dealing with real data. In particular, no comparisons at higher altitude levels are carried out, where the retrieval is unreliable due to enhanced contribution from *a priori* information.

## 5.2 Results

This section treats the results of the atmospheric observations with WaRAM2 in 2007. Measurements depend on liquid nitrogen being refilled to the cold calibration load. This is taken care of by our cooperation partners at Univer-

sidad de Los Andes, Mérida. Unfortunately, nitrogen could only be provided at irregular intervals. Table 5.1 sums up the days of operation referred to in the following.

### 5.2.1 Cold Load Radiance

With respect to the discussion of systematic calibration errors in section 5.1.4, experimental insight ought to be gained about the radiance actually seen at the cold calibration load. Dropping frequency dependence in the notation, the simplest expression to describe the received radiance is given by

$$I_{\text{N}_2(\text{aq})}(\nu) \propto [1 - r] \cdot I_{Pl}(T_{\text{N}_2(\text{aq})}, \nu) + r \cdot I_{Pl}(T_{lab}, \nu), \quad (5.2)$$

where  $r$  stands for the reflectance of the liquid nitrogen surface,  $I_{Pl}(T, \nu)$  for PLANCK's law, and  $T_{\text{N}_2(\text{aq})}$ ,  $T_{lab}$  for the temperatures of liquid nitrogen and the laboratory, respectively. The laboratory is conceived as a black body in this formulation. In the frequency range under consideration, the black body radiance at two distinct temperatures  $T_1, T_2 > 70$  K differs predominantly by a frequency-independent factor  $C$ , i.e.  $I_{Pl}(T_1, \nu) = C \cdot I_{Pl}(T_2, \nu)$ .<sup>14</sup> The resulting error is less than 1‰. Hence equation (5.2) can be rearranged to express the radiance from the cold load as PLANCK radiance at some

<sup>14</sup> This is not the well-known RAYLEIGH-JEANS approximation of PLANCK's law, because the formulation with a frequency-independent factor  $C$  does not imply linearity in  $T$ .

Table 5.1: The list reports start times of measurements by WaRAM2 in 2007 for which results are presented. Operation usually begins on Fridays, except for weeks 11 (Thu), 23 (Wed), and 28 (Sun). The various atmospheric integration times are due to different atmospheric conditions (*cf.* section 4.5).

Week	Day	Time started	Int. time
of 2007			
2	12	12 Jan 2007, 4:45 UTC	3.7 h
5	33	2 Feb 2007, 5:45 UTC	5.4 h
11	74	15 Mar 2007, 7:00 UTC	3.2 h
12	82	23 Mar 2007, 5:15 UTC	2.4 h
15	103	13 Apr 2007, 6:05 UTC	3.7 h
16	110	20 Apr 2007, 5:10 UTC	3.5 h
23	157	6 Jun 2007, 5:15 UTC	1.4 h
25	173	22 Jun 2007, 5:25 UTC	1.5 h
27	182	1 Jul 2007, 4:55 UTC	4.3 h
28	194	13 Jul 2007, 6:15 UTC	3.8 h

apparent temperature  $T_X$ , which is warmer than liquid nitrogen,

$$I_{N_2(\text{aq})} \propto I_{Pl}(T_X), \text{ where } T_X = T_{N_2(\text{aq})} + \Delta T.$$

The use of a wrong temperature/radiance in total-power calibration introduces a systematic error to the retrieval. When calculating spectra from the profiles,  $\hat{\mathbf{x}}$ , retrieved under these conditions, it turns out they match the measured spectra,  $\mathbf{y}$ , less well. This allows finding the correct  $\Delta T$  by carrying out total-power calibrations of atmospheric spectra for an ensemble of assumed cold load temperatures  $\{T_{X,i}\}$  and identifying the value that yields the best match between measured spectra and spectra calculated from retrieved profiles,  $\mathbf{F}(\hat{\mathbf{x}})$ . This requires a dedicated retrieval set-up and some kind of measure for spectra mismatch,  $\delta_i$ . With respect to the retrieval, the focus is to reproduce the spectra with radiative transfer calculations alone. Hence baseline consideration is only provided for standing waves, and retrieval convergence is instead ensured by stronger regularisation and a large start value for LEVENBERG-MARQUARDT iteration ( $\gamma_0 = 5 \cdot 10^7$ ,  $c_0 = 1.2$ ,  $c_\infty = 1.5$ , cf. section 4.6). The spectral fit thus attained often is poor, but for the approach discussed here it suffices to detect the change in  $\delta_i$  with  $T_{X,i}$ . A suitable expression for the mismatch,  $\delta_i$ , may be derived from the residuum  $\Delta \mathbf{y} = \mathbf{F}(\hat{\mathbf{x}}) - \mathbf{y}$ , by summing the squares of its spectral elements  $\Delta y_j$ , i.e.  $\delta_i = \sum_j (\Delta y_j)^2$  for a given  $T_{X,i}$ .

Figure 5.20 displays the results of this analysis on the WaRAM2 data-set. Retrievals from the dry atmosphere data of February 2nd and 3rd, as well as April 14th, converge particularly poorly, so these data have been exempted from the plot. Values given for each  $T_{X,i}$  comprise the average mismatch of the retrieval from the remaining 17 days of measurement. The resultant curve is quite smooth and allows to determine the apparent temperature of the cold calibration load as  $T_X = (75.8 \pm 0.5)$  K, which is significantly higher than its physical temperature,  $T_{N_2(\text{aq})} = 73.3$  K at 4765 m a.s.l. or  $\sim 575$  hPa

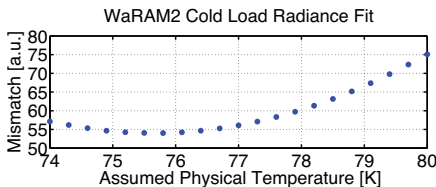


Figure 5.20: Retrieval mismatch, as defined in body text, plotted against different physical cold load temperatures assumed in the total-power calibration of the atmospheric spectra.

ambient pressure.  $T_X$  is used for total-power calibration throughout the remaining analysis.

## 5.2.2 Retrieval Characteristics

To gain some knowledge about the overall retrieval performance, the general expressions for retrieval characteristics given in section 4.6 can be numerically inspected for linearisation of the forward model about the *a priori* profile. Qpack provides a standard routine to obtain these results in form of the `qpackls_invchar.m` script. In addition, centre altitudes are computed for the individual averaging kernels as described by PALM (2006). The associated data are given in figure 5.21.

The upper left panel displays averaging kernels and the total measurement response of the retrieval in the altitude range where the measurements are most accurate. An ideal inverse method would yield  $A_{i,i} = 1$  at the individual retrieval grid levels  $i$  and  $A_{i,j} = 0$  at all other levels  $i \neq j$ . In practise, the averaging kernels are peaked functions, and their full width at half-maximum gives an indication about the vertical resolution of the observing system (*cf.* upper right panel). The individual maxima of the averaging kernels are considerably less than 1, which is caused by the retrieval process, sampling the profile at two or more times the actual resolution. Sensitivity must instead be read from the total measurement response  $\eta_i = \sum_j A_{i,j}$ , i.e. the area under the averaging kernel, which is also given in the same panel.

Below 25 km and above 50 km,  $\eta$  exhibits some marked deviations to values larger than 1. These correspond to information from other grid levels being overly carried over to the result at the respective level. Information content of the retrieval is considered satisfactory within the two levels indicated. This is also supported by the vertical resolution, as read from averaging kernels FWHM in the upper right panel. It starts at about 8 km for lower altitudes and significantly increases when approaching 50 km altitude. An upper altitude limit of 50 km is consistent with a spectrometer resolution bandwidth of 1.1 MHz. Also the averaging kernels peak appropriately as seen from the centre altitudes plotted in the same panel.

The bottom panel shows the total statistical error of the retrieved parameters. It comprises the observational error, which is related to the measure-

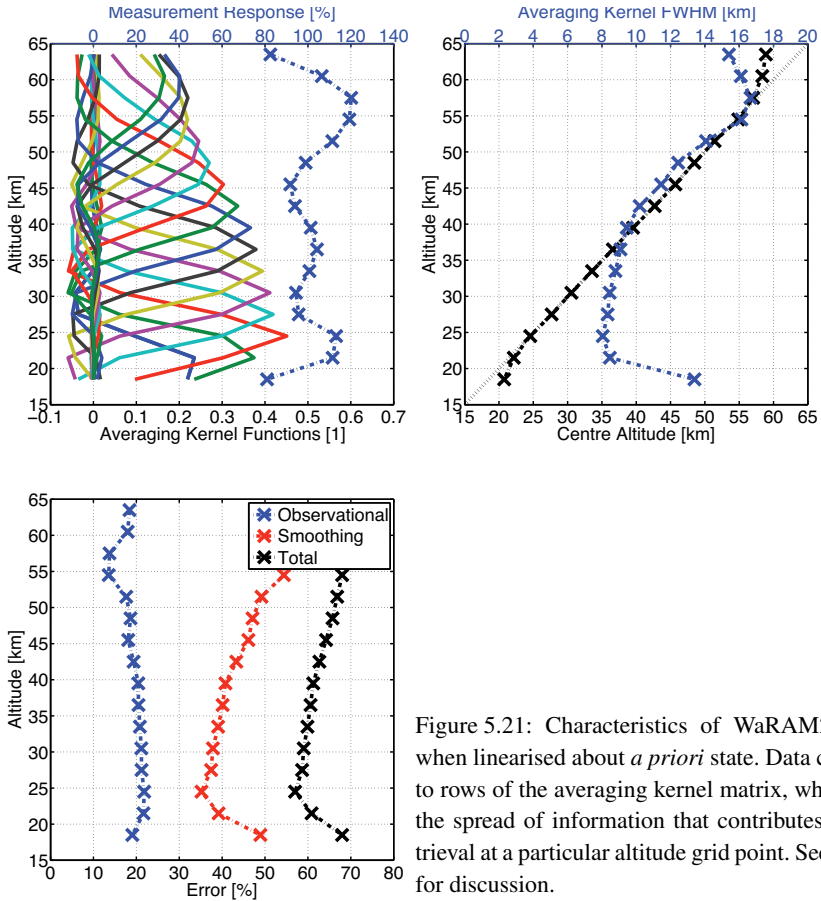


Figure 5.21: Characteristics of WaRAM2 retrieval when linearised about *a priori* state. Data correspond to rows of the averaging kernel matrix, which denote the spread of information that contributes to the retrieval at a particular altitude grid point. See body text for discussion.

ment noise, and the smoothing error, describing the *a priori* contribution. The observational error is rather large at 20%, which is due to omitting the even spectrometer channels, i.e. it lacks the correlation previously found in recorded spectral intensities. Still the smoothing error by far prevails over observation error. It is dominated by the uncertainty from how the tropospheric contribution is accounted for in the retrieval. Systematic errors may be introduced e.g. by calibration, antenna pointing error, and errors in the spectroscopic database. These are called parameter errors and require variational analysis to study. The magnitude of WaRAM2 parameter errors discussed by QUACK (2004) is more than an order of magnitude smaller than

the statistical error reported above, and may thus be neglected in the analysis here.

### 5.2.3 Retrieved Stratospheric Water Vapour

Retrieval results from the observations in 2007 are outlined in figure 5.22. To allow some analysis of retrieval stability, two separate retrievals are carried out for data from day 1 and 2 in each period of operation. All results reproduce the general characteristics of water vapour distribution in the stratosphere. They exhibit no oscillations, which marks a major improvement over earlier WaRAM2 results. Water vapour anomaly, defined as the absolute deviation from the mean over all results, is constrained to  $\pm 0.5$  ppmv. This corresponds well with the correlative data given above. Yet day-to-day variability appears unrealistically large for some of the results (weeks 2, 16 and 28). READ et al. (2007) estimate water vapour day-to-day variability in the tropical lower stratosphere water vapour to be no larger than 5%. On the

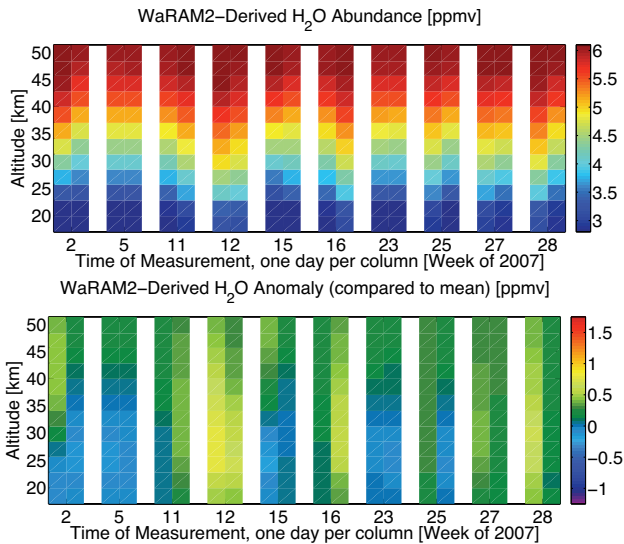


Figure 5.22: WaRAM2 retrieved water vapour from the measurements reported in table 5.1.

other hand, DEUBER (2005) has identified enhancements in mid-latitude stratospheric water vapour in excess of 20% over the course of two days, which have been traced back to pronounced mixing with subtropical air-masses. If large day-to-day variability persists in refined WaRAM2 results, it might eventually be possible to decide their being of instrumental or atmospheric origin.

A first look at how these results compare to correlative data is taken by recalling figure 5.19, which has indicated good sensitivity to seasonal variations in WaRAM2 retrievals from artificial data. This comparison is now carried out using real data in figure 5.23. One must keep in mind that the data-sets differ by 14 years in time, so no quantitative analysis is intended. However the plot is quite instructive with respect to the limitations implied in the analysis by the limited coverage of WaRAM2 data, only stretching across half a year. The significant seasonal signal that can be read from HALOE data in figure 5.19 is much less apparent in the data presented here.

For the time being, the magnitude of the error in WaRAM2 results pro-

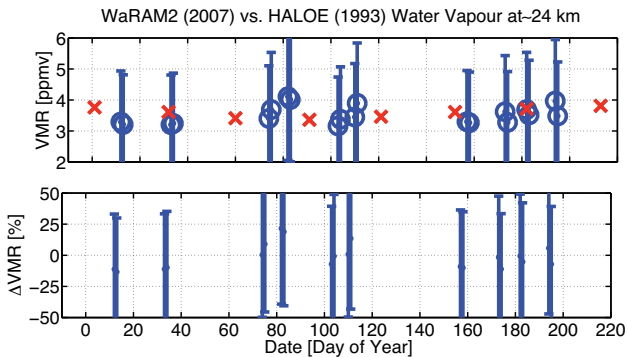


Figure 5.23: The comparison in figure 5.19 is recalled to give a qualitative impression of retrieval performance when using real data. The two data-sets are 14 years apart, thus no quantitative analysis is intended. (Upper panel) Blue markers denote water vapour VMR at  $\sim 24$  km as retrieved from WaRAM2 measurements in 2007. Error bars indicate the total retrieval error. Red crosses give water vapour VMR at the same altitude from HALOE results in 1993, zonal averages,  $12^{\circ}\text{N}$ – $12^{\circ}\text{S}$ . (Lower panel) presents relative deviation of the retrieved VMR from the corresponding HALOE value.

hibits definitive conclusions about the seasonal signal present in the data. It should be taken into account that the comparison is carried out below the lower altitude limit derived in section 5.2.2. Retrieval from WaRAM2 could be substantially improved if the tropospheric background contribution could be estimated more accurately. The total error would improve by reducing the smoothing error and by introducing more observations to the analysis.

### 5.2.4 Discussion

It is advisable to have a more detailed look at the averaging kernels for individual retrievals when discussing the quality of WaRAM2 results. Figure 5.24 picks results for three different days, with markedly different sensitivity to lower stratospheric water vapour. Closer analysis of this variability uncovers that it is associated by different sensitivity to contributions from the troposphere. In other words, a variable part of the retrieval response at lower stratospheric levels is due to signal from the upper troposphere. This is a severe concern, because water vapour abundance rises exponentially when descending into the troposphere, so it must be expected that these mismatched responses majorly contribute to the water vapour abundance retrieved at lower stratospheric levels. Figure 5.25 takes a look at how peak responses and centre altitudes of lower stratospheric averaging kernels evolve for all retrievals presented here. The data indicate that satisfactory stability is attained for retrieval levels 30km upwards. The variability at lower levels could not be attributed to different integration times of the underlying spectra, despite these account for differences in the noise by more than a factor of two across the data-set.

A special effort has been made to refine the retrieval pressure grid and the regularisation to better separate tropospheric from stratospheric contributions in the retrieval, however no significant improvement could be achieved. It occurs as if such artefacts must be lived with when attempting to cover both regimes in a continuous state vector. Relief from this problem may be conceived by splitting the state vector into two components, which separately address tropospheric and stratospheric contributions. This approach is supported by the observation that the tropopause essentially poses a blind spot in water vapour retrieval, which is caused by the profile characteris-

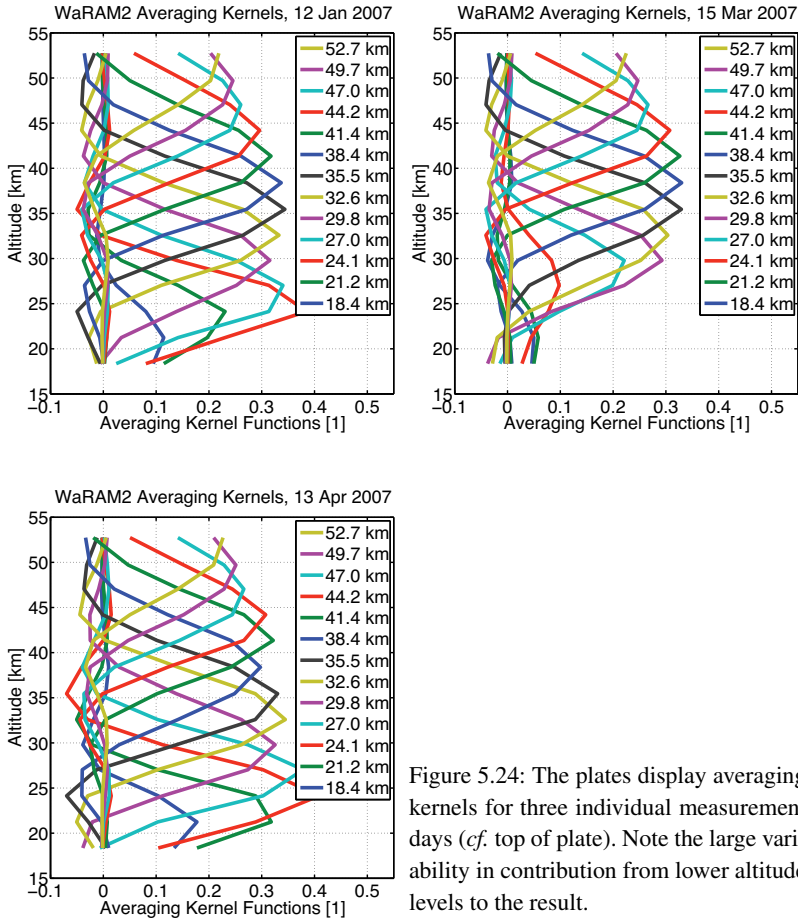


Figure 5.24: The plates display averaging kernels for three individual measurement days (*cf.* top of plate). Note the large variability in contribution from lower altitude levels to the result.

tic being exponential below the tropopause and almost constant above. Yet splitting the state vector also introduces new difficulty in providing an accurate model of atmospheric emission and the *a priori* ensemble in particular. For this reason it has so far been abstained from this set-up, but its realisation is currently being studied.

Given the past experience with relating the retrieval sensitivity to standing waves, it has been reckoned the observed variability in sensitivity could be connected to modifications in the baseline retrieval set-up. Presently, a new set of standing wave periods is fitted for each measurement day, which

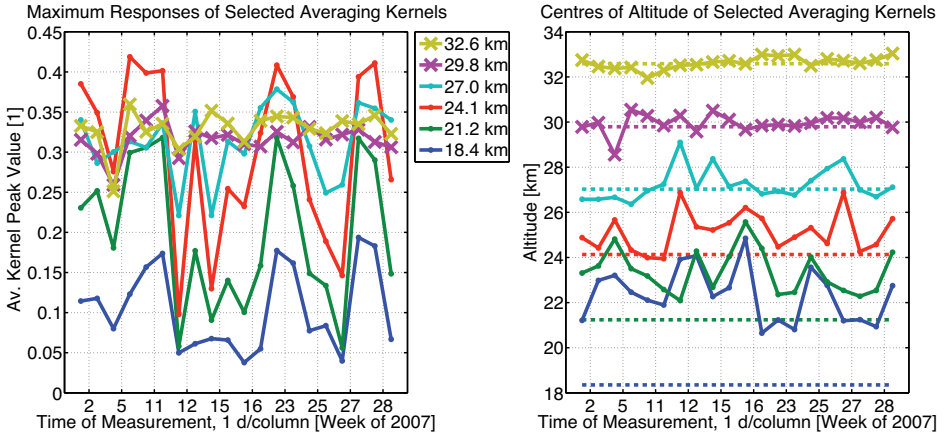


Figure 5.25: (Left panel) Magnitude of peak responses in WaRAM2 lower stratospheric averaging kernels, plotted versus time of measurement (discontinuous axis). Constant values indicate retrieval stability against various atmospheric scenarios. This is sufficiently attained only for the two uppermost retrieval grid levels plotted here, highlighted by crosses. (Right panel) Averaging kernel centre altitudes, plotted in the same manner. Retrieval stability is best when values are constant with time, and take their respective nominal value. The two uppermost grid levels, highlighted by crosses, again yield the most favourable results. Note how sensitivity at lower grid levels is increasingly pushed away from its nominal level, supporting the notion of a blind spot around the tropopause.

may potentially render significant differences to the instrument, the combination of sensor and retrieval. It would be preferable to have a uniform set of standing wave periods applied in all retrievals in the same way. However, no such set could be extracted from the spectra so far, very probably due to the different magnitude the standing waves attain for different tropospheric backgrounds, as well as distortions which could be introduced by a non-linear front-end or spectrometer.

Inspection of the baseline contributions to retrievals, as presented in figure 5.26, reveals that the retrievals might not be too sensitive to standing waves in the end. Instead some impact results from the offset that is fitted to atmospheric spectra. The plot shows that at certain levels, a 1 K offset fitted to the atmospheric spectrum contributes to the estimated profile like a 0.3 ppmv change in true atmospheric state. Figure 5.27 summarises the

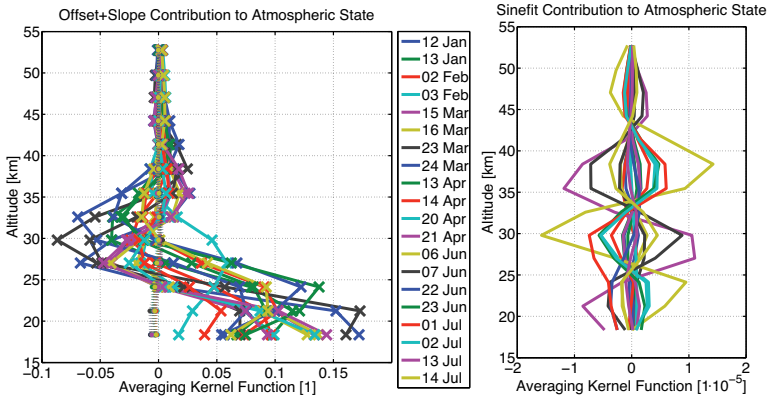


Figure 5.26: (Left panel) Sensitivity of the atmospheric part of the state vector to retrieved baseline offsets (solid lines, crosses) and slopes (dotted lines, discs). All data have been plotted in the same figure to indicate the general magnitude of the effect. While the fitted offset has some effect, the slope is uncritical. (Right panel) Sensitivity of atmospheric state to retrieved standing waves. Only the contribution of the wave with the largest amplitude is plotted for any single day. Note the difference in scale compared to the left panel. The plot suggests that retrieving standing waves does not effect noticeable distortions to the water vapour profile.

offsets actually retrieved from the measurements, ranging from  $-1.2\text{K}$  to  $0.5\text{K}$ . Hence at lower stratospheric levels, a systematic error of up to 10% must be assumed in individual results.

Consideration of offsets in atmospheric spectra is standard practise for retrievals from the much stronger ozone signature at  $142\text{GHz}$ , taken by IUP, U Bremen, with their OzoRAM sensor at Ny-Ålesund. (M PALM, IUP, U Bremen, pers. corr.). It has been implemented for WaRAM2 to have a uniform set-up that needs no manual tuning to individual atmospheric spectra for retrievals to converge. Despite the fact that this goal has been successfully achieved, the error introduced in stratospheric retrieval during this process presents a strong case to abandon offset consideration in favour of more accurately addressing instrumental and observational effects that could possibly have triggered the need for offset consideration.

From the experience gained so far, a number of potential issues come to mind that will be studied in future work. The spill-over between tropospheric and stratospheric information has already been mentioned above. It

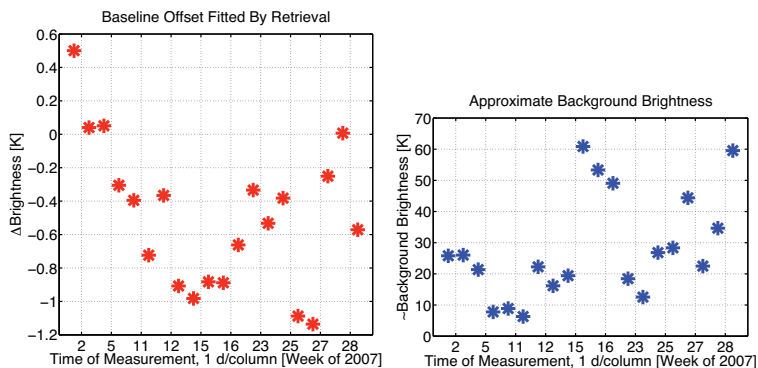


Figure 5.27: (Upper panel) The magnitude of the baseline offset fitted by the retrieval for each individual measurement (discontinuous time axis). (Lower panel) Approximate background brightness of the respective atmospheric spectra. The retrieved baseline offset appears to be uncorrelated with the background brightness.

will supposedly be overcome by separating the retrieval for these two parts of the state vector. Another point of concern is how extinction of radiation by clouds is represented in the retrieval. ARTS-1-0 provides the LIEBE et al. (1993) models for a crude quantification of extinction (absorption and scattering) by suspended liquid and ice droplets. These have not been deployed in the retrieval so far, in order to limit the number of free parameters and also because clear-sky conditions may be expected as a result of the spectra integration procedure discussed in section 4.5. They might play an important role when dealing with the spectra that show larger tropospheric background. As part of the required studies, an alternative route will be explored where the tropospheric absorption is described in terms of a polynomial continuum. This approach appeals for the reduction of free parameters, but may impose new limits on the bottom range for retrieval.

### 5.3 Comparison

Results from different sensors ought not be compared in terms of direct differences, because this introduces excess variance to the analysis. This can be avoided by simulating one retrieval with the other (PALM, 2006, according to RODGERS and CONNOR (2003)). Given the averaging kernel matrix,

$\mathbf{A}$ , and *a priori* state,  $\mathbf{x}_a$ , corresponding to an estimate,  $\hat{\mathbf{x}}$ , for which a comparison is desired, the simulated state,  $\hat{\mathbf{x}}_{sim}$ , is obtained from the original correlative data,  $\hat{\mathbf{x}}_{cor}$ , as

$$\hat{\mathbf{x}}_{sim} = \mathbf{x}_a - \mathbf{A}(\hat{\mathbf{x}}_{cor} - \mathbf{x}_a). \quad (5.3)$$

When comparing coarsely resolved data, like those from WaRAM2, with better resolved correlative results, this simulation will also provide for “resolution matching”. This means that the simulated retrieval  $\hat{\mathbf{x}}_{sim}$  will be smoothed to what could be seen with the lower resolved retrieval. To give a better impression of the comparison results, the data are also presented in relative units,

$$\Delta\hat{\mathbf{x}} = \frac{\hat{\mathbf{x}}_{WaRAM2} - \hat{\mathbf{x}}_{sim}}{\hat{\mathbf{x}}_{sim}}. \quad (5.4)$$

Given the premature state of WaRAM2 results, comparison has been restricted to a single correlative data-set. To this end, Aura/MLS has been selected from the available pool of correlative data. This choice has been motivated by the wealth of characterisation MLS data has undergone and its matching well in space and time with WaRAM2 measurements.

### 5.3.1 Aura/MLS

Water vapour results from the Aura/MLS 183 GHz receiver (*cf.* section 3.2.1) are obtained online<sup>15</sup> from Giovanni<sup>16</sup>. This is a web service that queries the user about the desired location and time, and provides profiles for up to three MLS measurements that match most closely. Data are requested for 9°N, 71°W, which intersects with the WaRAM2 field of view at  $\sim 30$  km altitude. They could be obtained for all but two days in the WaRAM2 data-set with distances ranging between 100 km – 1500 km. Distances for individual matches are reported below, alongside the comparison plots for single altitudes. WaRAM2 data are daily means, whereas MLS reports individual snapshots around 6:40 or 18:20 UTC, depending on day of comparison.

<sup>15</sup> <http://disc.sci.gsfc.nasa.gov/giovanni/>

<sup>16</sup> GES DISC DAAC Interactive Online Visualization and Analysis Infrastructure; Goddard Earth Sciences, Data and Information Services Center, Distributed Active Archive Center

An overview of the MLS results is given in figure 5.28. The same results when simulated with WaRAM2 retrieval, according to equation (5.3), are displayed in figure 5.29. At altitudes below 30km, the simulation introduces considerable deviation from the original MLS data. This coincides with the bottom end of reliable altitude range in WaRAM2, as identified for the current set-up in section 5.2.4. These deviations result from tropospheric signal being carried over to higher altitudes by WaRAM2 averaging kernels.

Figure 5.30 presents an overview of WaRAM2 results compared to the simulated MLS results above. Data are expressed in relative amounts according to equation (5.4). Best agreement is attained at about 35km altitude, with WaRAM2 reporting lower values than simulated MLS both below and above this altitude. Regarding lower altitudes, this disagreement is attributed to numerical artefact, which is brought about by tropospheric water vapour being injected to simulated MLS data. The disagreement in upper stratospheric results is smaller and remains almost constant at about  $-10\%$ . More detailed discussion is given below.

A more detailed comparison for 24km altitude, including error bars for

Figure 5.28: MLS water vapour profiles which best match WaRAM2 measurement time and location as obtained from Giovanni. Data are provided on a pressure grid, transformation to altitude is based on ECMWF operational analyses.

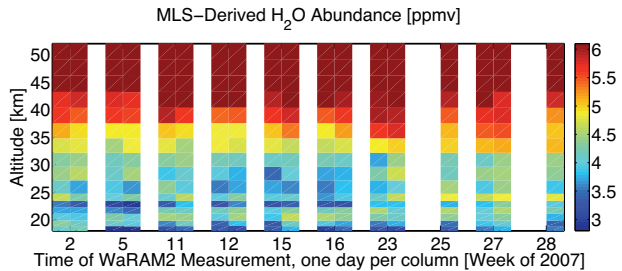
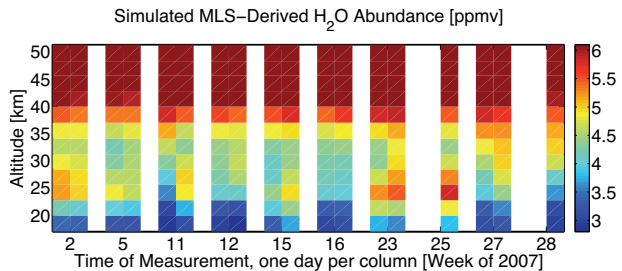


Figure 5.29: Data from figure 5.28 as would be seen by WaRAM2, according to equation (5.3). The simulation introduces considerable deviation at altitudes lower than 30km, which is the bottom end of reliable altitude range in the current WaRAM2 set-up.



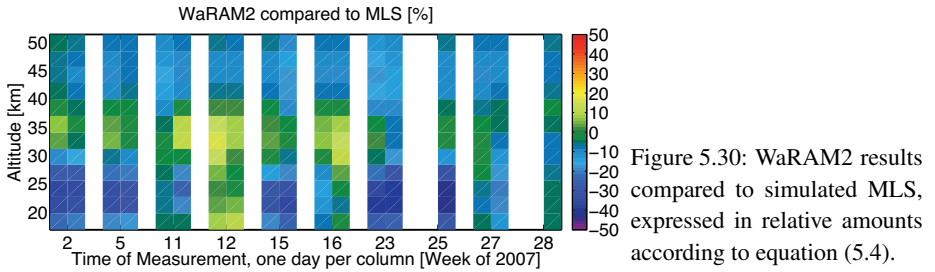


Figure 5.30: WaRAM2 results compared to simulated MLS, expressed in relative amounts according to equation (5.4).

WaRAM2 retrieval, is given in figure 5.31. Simulated MLS data spread over unrealistically large range, 3.5 – 6.0 ppmv, and in general appear overestimated, as has already been attributed to tropospheric signal. WaRAM2 results range between 3.0 – 4.0 ppmv, which is well within expectation, despite the same averaging kernels applying for this retrieval. Yet in WaRAM2 retrieval, the misplaced tropospheric signal is corrected for by regularisation through *a priori* information. This is not possible for the simulated MLS

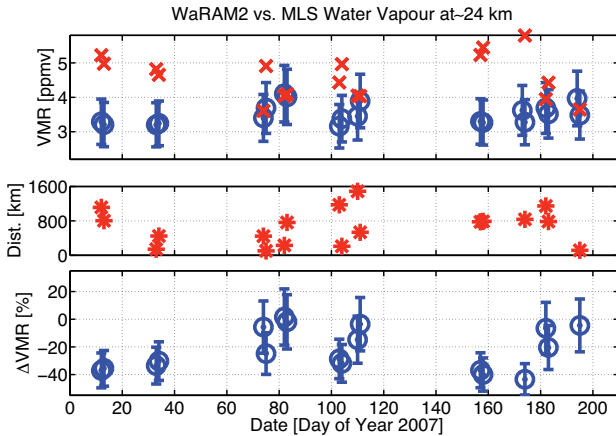


Figure 5.31: (Upper panel) Absolute water vapour abundance from WaRAM2 (blue circles, with error bars) at  $\sim 24$  km, compared to simulated MLS (red crosses). This altitude level is below the reliable range of current WaRAM2 retrieval. Variability in simulated MLS likely results from tropospheric signal carried over by WaRAM2 averaging kernels. (Middle panel) Distance of MLS measurement from WaRAM2. (Lower panel) Same as upper panel, but data are given in relative units.

data, since the original data are merely convolved with WaRAM2 averaging kernels. This analysis supports the conclusion drawn earlier that below 30km, WaRAM2 data must currently be classified unreliable.

Comparison at 33 km is illustrated in more detail in figure 5.32. This level is within the reliable range of WaRAM2, and its results match simulated MLS within 10% ( $\sim 0.4$  ppmv), most even better, except for days 82 (16%) and 112 (13%). In all cases the results agree well within WaRAM2 error bars. This indicates the instrument operates to expectation at this altitude. However, apart from the large magnitude of error that would be allowed, the data-set is yet too short to draw first conclusions about seasonal variation being detectable from the results.

Eventually a look at the 44 km data is taken in figure 5.33. Again WaRAM2 matches simulated MLS well within error bars, but in mutual comparison WaRAM2 data appear biased to lower water vapour VMRs,  $\mu_V$ . The mean difference amounts to 11% ( $\sim 0.7$  ppmv). At the same time WaRAM2 results exhibit considerably less variability at this altitude than at 34 km (standard deviation  $\sigma_{\mu_V, W} = 0.11$  at 44 km, compared to  $\sigma_{\mu_V, W} = 0.24$  at 34 km). This is not found in simulated MLS data ( $\sigma_{\mu_V, M} = 0.23$  at 34 km and  $\sigma_{\mu_V, M} = 0.20$  at 44 km), so excess regularisation may have forced the retrieval to stick

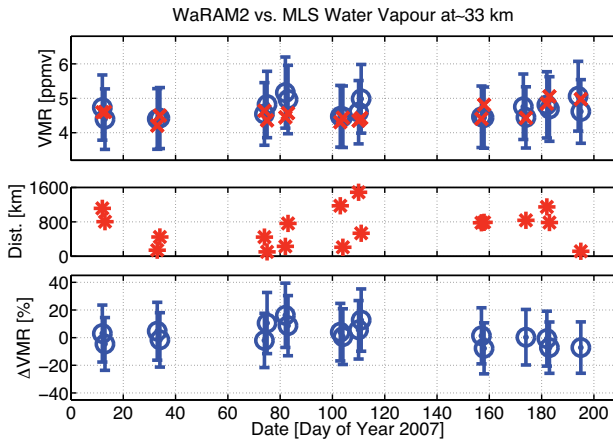


Figure 5.32: Same as figure 5.31, but data are taken at  $\sim 33$  km, within the reliable range of WaRAM2 retrieval.

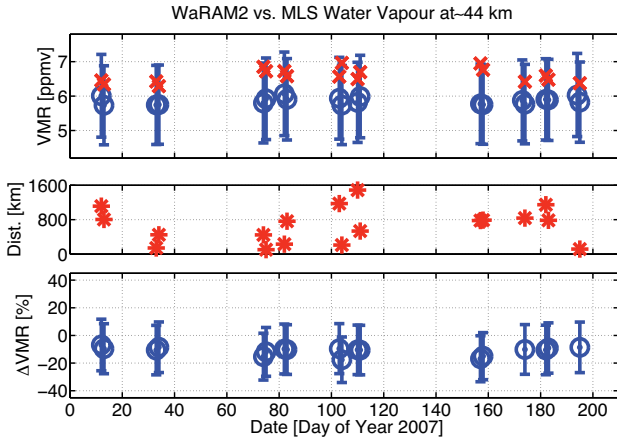


Figure 5.33: Same as figure 5.31, but data are taken at  $\sim 44$  km, within the reliable range of WaRAM2 retrieval.

too close to *a priori*. This observation is left to further study in a more mature revision of WaRAM2 results.



## 6 Conclusions

This work deals with the abundance and distribution of tropical stratospheric water vapour. Tropical latitudes are of particular concern since large-scale diabatic ascent through the cold tropical tropopause forms an important mechanism how water vapour enters the stratosphere. It is complemented by localised convective injections of ice into the extratropical stratosphere during summer. These two mechanisms behave differently from a climate change point of view. While in the former, stratospheric water vapour should decrease in response to lowering temperatures at the tropopause, the latter gives rise to an increase in stratospheric water vapour due to warming at Earth's surface, causing stronger convection.

Given the large disagreement, in particular at low volume mixing ratios, between observations of water vapour, considerable effort is devoted to discuss various observation techniques. The discrepancies found between sensors are far in excess of the expected accuracies, and in some cases the interpretation of atmospheric processes may change when using data from different instruments. No significant progress could so far be achieved as to resolve the underlying issues. With this in mind, the discussion of observing methods given here is intended as an initial point of reference to rate the capabilities and shortcomings of the different sensors in use.

The main focus of this work is the analysis of tropical stratospheric water vapour observations, which have been carried out with the ground-based microwave radiometer WaRAM2 at the high-altitude Mérida Atmospheric Research Station. It is the only sensor of this kind to operate in the tropics. A numerical experiment is presented, which supports the general suitability of such measurements to study seasonal variability in tropical stratospheric water vapour. Several problems are identified in the raw data with respect to frequency stability and linearity of the receiver, and baseline artefacts are investigated in detail. The instrument is characterised well enough to present

a time series of water vapour from the aforementioned observations. It is based on an updated retrieval set-up, which utilises the entire spectral bandwidth recorded by the sensor, and eliminates undesired oscillations found in earlier results obtained from WaRAM2 measurements. Reliable data range from 30 – 50 km altitude at roughly 10 km vertical resolution. Comparison against correlative data from Aura/MLS yields good agreement at 33 km. At 44 km, WaRAM2 derived water vapour on average is 0.7 ppmv (10%) lower than MLS.

The analysis indicates that the most critical retrieval issue is how the tropospheric background is considered when processing the spectra. Consideration of a baseline offset aids retrieval convergence, but at the same time introduces an error that limits the lower altitude for retrievals to 30 km. This may be overcome by separating the retrievals for the tropospheric background and the stratosphere, a modification which is currently being investigated. Such an improvement holds promise to extend the retrieval into the lower stratosphere, which is of utmost importance to utilise the sensor's capability for observations of the tape recorder signal. To the other end of the range, WaRAM2 sensitivity could be pushed into the mesosphere by use of a better resolving spectrometer. This could form a valuable asset for the study of upper stratospheric and mesospheric dynamical aspects.

# Appendix



# A Humidity Expressions

Depending on context, different formulations are used to express the water vapour content of air, or humidity. An overview of some of these is given here for reference.

## Water Saturation Vapour Pressure

Saturation (vapour) pressure denotes the partial pressure of a vapour in equilibrium with its liquid and solid phases. If partial pressure is higher than saturation pressure of the considered species, it tends to condense or deposit, depending on nucleation being possible. In other words, saturation pressure governs the maximum possible concentration of a gas, but supersaturation may be of major importance, and is in fact with respect to water vapour.

Saturation pressure is fundamentally obtained from integration of the CLAPEYRON equation, which however relies on temperature-dependant parameters that must be obtained empirically. VÖMEL (2006) has assembled several scientifically relevant formulations of water saturation pressure, which are too lengthy to sensibly be reproduced here. Some of them are discussed by MILOSHEVICH et al. (2006), along with implications of their use in analysis of radiosonde data, which are commonly reported as relative humidity with respect to water. As a first impression, the relatively simple (and inaccurate) SONNTAG revision of the MAGNUS formulae is given here (according to HÄCKEL, 2005):

$$e_{aq}(\vartheta) = 6.11213 \text{ hPa} \cdot \exp\left(\frac{17.5043 \vartheta}{241.2^\circ\text{C} + \vartheta}\right), \text{ and}$$
$$e_{ice}(\vartheta) = 6.11153 \text{ hPa} \cdot \exp\left(\frac{22.4433 \vartheta}{272.186^\circ\text{C} + \vartheta}\right),$$

where  $e_{aq}$  and  $e_{ice}$  are saturation pressure over water and ice respectively, at temperature  $\vartheta$  [ $^\circ\text{C}$ ].

### Absolute Humidity

Absolute humidity,  $\rho_w$ , denotes the mass of water vapour,  $m_w$ , per volume  $V$ . Using the ideal gas law, it may be rearranged for water vapour partial pressure,  $e_w$ , and temperature,  $T$ ,

$$\rho_w = \frac{m_w}{V} = \frac{e_w M_w}{RT},$$

where  $R$  is the universal gas constant and  $M_w$  molar mass of water.

### Relative Humidity

Relative humidity,  $RH_{(aq)}$  or  $RH_{i(ce)}$ , is the ratio of water vapour partial pressure and saturation pressure with respect to water or ice at a given temperature,

$$RH_{(aq)} = \frac{e_w}{e_{aq}(T)},$$

$$RH_{i(ce)} = \frac{e_w}{e_{ice}(T)}.$$

$RH$  is commonly expressed as percentage. Supersaturation is common in the atmosphere, so  $RH$  may be larger than 100%.

### Mixing Ratio

The mixing ratio is given by the mass of water vapour per mass of dry air in a particular volume,

$$\mu = \frac{M_w}{M_{air}} \frac{e_w}{p - e_w},$$

where  $p$  denotes ambient pressure.

### Specific Humidity

Specific humidity instead denotes the mass of water vapour per mass of moist air in a particular volume,

$$s = \frac{M_w}{M_{air}} \cdot \frac{e_w}{p - \left[1 - \frac{M_w}{M_{air}}\right] e_w}.$$

It is connected to mixing ratio like

$$s = \frac{\mu}{1 + \mu} \iff \mu = \frac{s}{1 - s}.$$

### Volume Mixing Ratio (VMR)

VMR is the ratio of the number of water molecules and the total number of molecules in a particular volume,

$$\mu_V = \frac{e_w}{p}.$$

### Integrated Water Vapour (IWV)

IWV denotes the integral of absolute humidity in a vertical column starting from ground,

$$IWV = \int_{z_0}^{z_{\infty}} dz \rho_w(z),$$

where  $z$  is altitude. This is equivalent to the total mass of water vapour in the vertical column, divided by its base area.

### Precipitable Water Vapour (PWV)

PWV is the liquid water level that would be obtained in a vertical column if all water vapour in the column were condensed and gathered at the ground,

$$PWV = \frac{IWV}{\rho_{aq}},$$

where  $\rho_{aq}$  stands for the density of liquid water at sea level pressure. Since  $\rho_{aq} \approx 1000 \text{ kg m}^{-3}$  (originally identity by definition), PWV can be obtained from IWV by replacing the canonical unit of IWV,  $[\text{kg m}^{-2}]$ , with  $[\text{mm}]$ .



## B Bibliography

- ANDERSON, GP, et al. (1986), AFGL atmospheric constituent profiles (0–120 km), *Technical Report TR-86-0110*, AFGL, URL <http://www.dtic.mil/cgi-bin/GetTRDoc?AD=ADA175173&Location=U2&doc=GetTRDoc.pdf>. [6, 10, 75]
- ANDERSON, PS (1995), Mechanism for the behavior of hydroactive materials used in humidity sensors, *J Atmos Ocean Tech*, 12(3), 662–667, DOI 10.1175/1520-0426(1995)012%3C0662:MFTBOH%3E2.0.CO;2. [19]
- BALDWIN, MP, M DAMERIS, and TG SHEPHERD (2007), Atmosphere - How will the stratosphere affect climate change?, *Science*, 316(5831), 1576–1577, DOI 10.1126/science.1144303. [15]
- BARBER, RJ, J TENNYSON, GJ HARRIS, and RN TOLCHENOV (2006), A high-accuracy computed water line list, *Mon Not R Astron Soc*, 368(3), 1087–1094, DOI 10.1111/j.1365-2966.2006.10184.x. [56]
- BEHRENDT, A, et al. (2007), Intercomparison of water vapor data measured with lidar during IHOP\_2002. Part II: Airborne-to-airborne systems, *J Atmos Ocean Tech*, 24(1), 22–39, DOI 10.1175/JTECH1925.1. [53]
- BERG, H (2000), Weiterentwicklung der Millimeterwellenradiometrie stratosphärischer Spurengase in Emission und Absorption, Doctoral thesis, in *FZKA-Berichte, Wissenschaftliche Berichte*, vol. 6515, Forschungszentrum Karlsruhe, Germany, URL <http://www-imk.fzk.de/asf/mira/Publicat/Dokus/FZKA6515.pdf>. [62, 63]
- BEVIS, M, et al. (1992), GPS Meteorology: Remote Sensing of Atmospheric Water Vapor using the Global Positioning System, *J Geophys Res*, 97(D14), 15,787–15,801, DOI 10.1029/92JD01517. [50]
- BOUSQUET, P, et al. (2006), Contribution of anthropogenic and natural sources to atmospheric methane variability, *Nature*, 443(7110), 439–443, DOI 10.1038/nature05132. [10]
- BOWMAN, KP, LL PAN, T CAMPOS, and R GAO (2007), Observations of fine-scale transport structure in the upper troposphere from the High-performance Instrumented Airborne Platform for Environmental Research, *J Geophys Res*, 112, D18,111, DOI 10.1029/2007JD008685. [34]
- BRAATHEN, GE (2006), Report from the NDACC meeting on atmospheric water vapour measurement, *Technical report*, NDACC, URL [http://www.iapmw.unibe.ch/research/collaboration/ndsc-microwave/workshop/2006/Bern\\_Report\\_H2O\\_workshop2006.pdf](http://www.iapmw.unibe.ch/research/collaboration/ndsc-microwave/workshop/2006/Bern_Report_H2O_workshop2006.pdf). [35]
- BRASSEUR, GP, JJ ORLANDO, and GS TYNDALL (Eds.) (1999), *Atmospheric Chemistry and Global Change*, Topics in Environmental Chemistry, Oxford University Press, Oxford, UK. [5, 99]

- BREWER, AW (1949), Evidence for a world circulation provided by the measurements of helium and water vapour distribution in the stratosphere, *Q J Roy Meteor Soc*, 75(326), 351–363, DOI 10.1002/qj.49707532603. [8, 24]
- Britannica (2008), Horace Bénédicte de Saussure, in *Encyclopædia Britannica*, URL <http://www.britannica.com/EBchecked/topic/525586/Horace-Benedict-de-Saussure>, retrieved from Encyclopædia Britannica Online. [19]
- BUEHLER, S, et al. (2005), ARTS, the atmospheric radiative transfer simulator, *JQSRT*, 91(1), 65–93, DOI 10.1016/j.jqsrt.2004.05.051. [74]
- BURNS, WE (2003), *Science in the Enlightenment*, ABC-CLIO, Santa Barbara, California, USA. [24]
- CARLEER, MR, et al. (2008), Validation of water vapour profiles from the Atmospheric Chemistry Experiment (ACE), *Atmos Chem Phys Discussions*, 8, 4499–4559, SREF-ID 1680-7375/acpd/2008-8-4499. [46]
- CLANCY, RT, and DO MUHLEMANN (1993), *Ground-Based Microwave Spectroscopy of the Earth's Stratosphere and Mesosphere*, pp. 335–381, in JANSSEN (1993a). [56]
- COFFEY, MT, et al. (2008), Airborne Fourier transform spectrometer observations in support of EOS Aura validation, *J Geophys Res*, 113, D16S42, DOI 10.1029/2007JD008833. [46]
- CORTESI, U, et al. (2005), SAFIRE-A (spectroscopy of the atmosphere by using far-infrared emission-airborne): Assessment of measurement capabilities and future developments, *Adv Space Res*, 36(5, Sp. Iss. 2005), 888–893, DOI 10.1016/j.asr.2005.03.109. [46]
- CRUZ-POL, SL, CS RUF, and SJ KEIHM (1998), Improved 20-32 GHz Atmospheric Absorption Model, *Radio Sci*, 33(5), 1319–1333, DOI 10.1029/98RS01941. [59]
- DE WACHTER, E, et al. (2008), Stratospheric water vapour profiles over Seoul, S-Korea, Poster presentation at SPARC, 4th General Assembly, Bologna, Italy, 31.08.2008, URL <http://www.iap.unibe.ch/publications/pub-detail.php?lang=en&id=3078>. [40]
- DE WACHTER, E, et al. (to appear), Effects of Resonances in Corrugated Horn Antennas for a 22-GHz Balancing Radiometer, *IEEE Geosci Remote S*, DOI 10.1109/LGRS.2008.2005851. [63]
- DEMTRÖDER, W (2007), *Laserspektroskopie — Grundlagen und Technik*, 5 ed., Springer-Verlag, Berlin/Heidelberg, Germany, DOI 10.1007/978-3-540-33793-5. [33]
- DESSLER, AE, TF HANISCO, and S FUEGLISTALER (2007), Effects of convective ice lofting on H<sub>2</sub>O and HDO in the tropical tropopause layer, *J Geophys Res*, 112, D18,309, DOI 10.1029/2007JD008609. [11]
- DEUBER, B, N KÄMPFER, and DG FEIST (2004), A New 22-GHz Radiometer for Middle Atmospheric Water Vapor Profile Measurements, *IEEE T Geosci Remote*, 42(5), 974–984, DOI 10.1109/TGRS.2004.825581. [40]
- DEUBER, B (2005), *Microwave Remote Sensing of Water Vapour in the Middle Atmosphere — Calibration, Validation and Applications in Atmospheric Studies*, Doctoral thesis, IAP, Universität Bern, Switzerland, URL <http://www.iap.unibe.ch/publications/pub-detail.php?lang=en&id=2496>. [107]
- DI GIROLAMO, P, et al. (2008), Simulation of satellite water vapour lidar measurements: Performance assessment under real atmospheric conditions, *Remote Sens Environ*, 112(4), 1552–1568, DOI 10.1016/j.rse.2007.08.008. [53]

- DINELLI, BM, et al. (2008), Measurement of the tropical UTLS composition in presence of clouds using millimetre-wave heterodyne spectroscopy, *Atmos Chem Phys Discussions*, 8, 14, 169–14,216, SREF-ID 1680-7375/acpd/2008-8-14169. [43]
- DUBOIS, P (1955), *Das Observatorium Lindenberg in seinen ersten 50 Jahren 1905–1955, Geschichte der Meteorologie in Deutschland*, vol. 1, Deutscher Wetterdienst (self-published). [7]
- DURRY, G, and G MEGIE (1999), Atmospheric CH<sub>4</sub> and H<sub>2</sub>O Monitoring With Near-Infrared InGaAs Laser Diodes by the SDLA, a Balloonborne Spectrometer for Tropospheric and Stratospheric In Situ Measurements, *Appl Opt*, 38(36), 7342–7354, DOI 10.1364/AO.38.007342. [35]
- DURRY, G, et al. (2004), In situ sensing of the middle atmosphere with balloonborne near-infrared laser diodes, *Spectrochim Acta A*, 60(14), 3371–3379, DOI 10.1016/j.saa.2003.11.050. [35]
- DURRY, G, et al. (2008), Laser diode spectroscopy of H<sub>2</sub>O at 2.63  $\mu$ m for atmospheric applications, *Atmos Res*, 90(3-4), 573–580, DOI 10.1007/s00340-007-2884-3. [36]
- ERIKSSON, P, C JIMÉNEZ, and SA BUEHLER (2004), Qpack, a general tool for instrument simulation and retrieval work, *JQSRT*, 91(1), 47–64, DOI 10.1016/j.jqsrt.2004.05.050. [75]
- FALLY, S, et al. (2007), Water vapour retrievals from ground-based FTIR observations at Ile de la Réunion: Focus on isotopologues, *Geophys Res Abstracts*, 9, 08,331, SREF-ID 1607-7962/gra/EGU2007-A-08331. [45]
- FISCHER, H, et al. (2008), MIPAS: an instrument for atmospheric and climate research, *Atmos Chem Phys*, 8(8), 2151–2188, SREF-ID 1680-7324/acp/2008-8-2151. [45, 47]
- FLURY, T, K HOCHE, SC MÜLLER, and N KÄMPFER (2008), First measurements of lower mesospheric wind by airborne microwave radiometry, *Geophys Res Lett*, 35, L19,802, DOI 10.1029/2008GL034663. [41]
- FORKMAN, P, P ERIKSSON, and A WINNBERG (2003), The 22 GHz radio-aeronomy receiver at onsala space observatory, *JQSRT*, 77(1), 23–42, DOI 10.1016/S0022-4073(02)00073-0. [40]
- FRIED, A, et al. (2008), Tunable infrared laser instruments for airborne atmospheric studies, *Atmos Res*, 92(3), 409–417, DOI 10.1007/s00340-008-3136-x. [32, 35]
- FUEGLISTALER, S, M BONAZZOLA, PH HAYNES, and T PETER (2005), Stratospheric water vapor predicted from the Lagrangian temperature history of air entering the stratosphere in the tropics, *J Geophys Res*, 110, D08,107, DOI 10.1029/2004JD005516. [12, 13]
- GARDINER, T, et al. (2005), Trace Water Vapour Measurements and Calibration, pp. 41–42, Natural Environment Research Council, URL [http://utls.nerc.ac.uk/research/reports/Water\\_Vapour\\_proceedings.pdf](http://utls.nerc.ac.uk/research/reports/Water_Vapour_proceedings.pdf). [35]
- GASIEWSKI, AJ (1992), Numerical Sensitivity Analysis of Passive EHF and SMMW Channels to Tropospheric Water Vapor, Clouds, and Precipitation, *IEEE T Geosci Remote*, 30(5), 859–870, DOI 10.1109/36.175320. [43]
- GATTINGER, RL, DA DEGENSTEIN, and EJ LLEWELLYN (2006), Optical Spectrograph and Infra-Red Imaging System (OSIRIS) observations of mesospheric OH A<sup>2</sup> $\Sigma^+$  – X<sup>2</sup> $\Pi$  0 – 0 and 1 – 1 band resonance emissions, *J Geophys Res*, 111, D13,303, DOI 10.1029/2005JD006369. [49]

- GERDING, M, C RITTER, M MULLER, and R NEUBER (2004), Tropospheric water vapour soundings by lidar at high Arctic latitudes, *Atmos Res*, 71(4), 289–302, DOI 10.1016/j.atmosres.2004.07.002. [52]
- GOBIET, A, et al. (2007), Retrieval of temperature profiles from CHAMP for climate monitoring: intercomparison with Envisat MIPAS and GOMOS and different atmospheric analyses, *Atmos Chem Phys*, 7(13), 3519–3536, SREF-ID 1680-7324/acp/2007-7-3519. [51]
- GOLDSMITH, PF (1998), *Quasioptical Systems*, Series on Microwave Technology and RF, IEEE Press/Chapman & Hall, New York. [61]
- GREENE, MT (2000), High achiever - The discovery of the stratosphere laid the foundations of geophysics, *Nature*, 407, 947, DOI 10.1038/35039642. [7]
- GROSSKLOSS, R, P KERSTEN, and W DEMTRÖDER (1994), Sensitive Amplitude- and Phase-Modulated Absorption-Spectroscopy with a Continuously Tunable Diode Laserspektroskopie, *Atmos Res*, 58(2), 137–142, DOI 10.1007/BF01082348. [33]
- GUSTINCIC, JJ (1977), A Quasi-Optical Receiver Design, *Microwave Symposium Digest, MTT-S International*, 77(1), 99–101, URL <http://ieeexplore.ieee.org/stamp/stamp.jsp?arnumber=1124373&isnumber=24841>, retrieved January 9, 2008. [63]
- HANSFORD, G, et al. (2006), Lightweight dew-/frost-point hygrometer based on a surface-acoustic-wave sensor for balloon-borne atmospheric water vapor profile sounding, *Rev Sci Instrum*, 77(1), 014,502, DOI 10.1063/1.2140275. [24]
- HARRIES, JE, et al. (1996), Validation of measurements of water vapor from the halogen occultation experiment (HALOE), *J Geophys Res*, 101(D6), 10,205–10,216, DOI 10.1029/95JD02933. [48]
- HARTMANN, G, et al. (1996), Measurements of O-3, H<sub>2</sub>O and ClO in the middle atmosphere using the millimeter-wave atmospheric sounder (MAS), *Geophys Res Lett*, 23(17), 2313–2316, DOI 10.1029/96GL01475. [42]
- HELTEN, M, et al. (1998), Calibration and performance of automatic compact instrumentation for the measurement of relative humidity from passenger aircraft, *J Geophys Res*, 103(D19), 25,643–25,652, DOI 10.1029/98JD00536. [22]
- HERMAN, RL, and AJ HEYMSFIELD (2003), Aircraft icing at low temperatures in Tropical Storm Chantal (2001), *Geophys Res Lett*, 30(18), 1955, DOI 10.1029/2003GL017746. [34]
- HINTSA, EJ, et al. (1999), On the accuracy of in situ water vapor measurements in the troposphere and lower stratosphere with the Harvard Lyman-alpha hygrometer, *J Geophys Res*, 104(D7), 8183–8189, DOI 10.1029/1998JD100110. [15, 30]
- HOCHSCHILD, G, J GROSS, P HOFFMANN, and G KOPP (2008), Observation of stratospherical trace gases by millimeter wave radiometry in tropical South America, URL [http://www-imk.fzk.de/asf/mira/Publicat/Dokus/Poster\\_MicroRad2008.pdf](http://www-imk.fzk.de/asf/mira/Publicat/Dokus/Poster_MicroRad2008.pdf), poster presentation at Microrad 2008, Firenze, Italy. [40]
- HOENK, ME, G CARDELL, F NOCA, and RK WATSON (2000), A surface acoustic wave hygrometer for high-resolution measurements of atmospheric humidity (A), *J Acoust Soc Am*, 108(5), 2495, URL <http://link.aip.org/link/?JASMAN/108/2495/1>. [24]
- HOFFMANN, C (2008), Optimierung der Mikrowellenradiometer OzoRAM und WaRAM, Diploma thesis, IUP, Universität Bremen, Germany, URL [http://www.iup.uni-bremen.de/ram/publ/diplomarbeit\\_choffmann.pdf](http://www.iup.uni-bremen.de/ram/publ/diplomarbeit_choffmann.pdf). [63, 93]

- HOFFMANN, L, et al. (2008), CRISTA-NF measurements of water vapor during the SCOUT-O3 Tropical Aircraft Campaign, *Adv Space Res*, DOI 10.1016/j.asr.2008.03.018. [49]
- HOLTON, JR, et al. (1995), Stratosphere-Troposphere Exchange, *Rev Geophys*, 33(4), 403–439, DOI 10.1029/95RG02097. [8]
- HOOGVEEN, RWM, et al. (2005), Superconducting Integrated Receiver development for TELIS, in *Sensors, Systems, and Next-Generation Satellites IX, Proc SPIE*, vol. 5978, DOI 10.1117/12.627660. [43, 44]
- HOUMMADY, M, et al. (1995), Surface acoustic wave (SAW) dew point sensor: application to dew point hygrometry, *Sensors Actuat B-Chem*, 27(1-3), 315–317, DOI 10.1016/0925-4005(94)01609-L. [24]
- HÄCKEL, H (2005), *Meteorologie*, 5th ed., Eugen Ulmer KG. [19, 123]
- IAEA (2008), Reference Materials for Trade and Development: Quality and Comparability. Supplement to the Nuclear Technology Review 2008, *Information Document for the 52nd IAEA General Conference*, International Atomic Energy Agency (IAEA), URL [http://www.iaea.org/About/Policy/GC/GC52/GC52InfDocuments/English/gc52inf-3-att3\\_en.pdf](http://www.iaea.org/About/Policy/GC/GC52/GC52InfDocuments/English/gc52inf-3-att3_en.pdf). [11]
- IPCC (2007), *The Physical Science Basis, Climate Change 2007*, vol. 1, Cambridge University Press, Cambridge, UK, URL <http://www.ipcc.ch/ipccreports/assessments-reports.htm>, contribution of Working Group I to the Fourth Assessment Report of the IPCC. [13, 14]
- JANSSEN, MA (1993a), *Atmospheric Remote Sensing by Microwave Radiometry*, John Wiley & Sons, Inc, New York City, USA. [55, 128, 131, 135]
- JANSSEN, MA (1993b), *An Introduction to the Passive Microwave Remote Sensing of Atmospheres*, chap. 1, pp. 1–35, in JANSSEN (1993a). [39, 60]
- KELLY, KK, et al. (1989), Dehydration In The Lower Antarctic Stratosphere During Late Winter And Early Spring, 1987, *J Geophys Res*, 94(D9), 11,317–11,357, DOI 10.1029/JD094iD09p11317. [30]
- KELLY, KK (2006), NOAA/CSD frost point instrument, URL <http://cloud1.arc.nasa.gov/docs/ave-costarica2/FP.pdf>. [25]
- KHAPLANOV, M, J GUMBEL, N WILHELM, and G WILT (1996), Hygrosonde - A direct measurement of water vapor in the stratosphere and mesosphere, *Geophys Res Lett*, 23(13), 1645–1648, DOI 10.1029/96GL01482. [31]
- KIEMLE, C, et al. (2008), First airborne water vapor lidar measurements in the tropical upper troposphere and mid-latitudes lower stratosphere: accuracy evaluation and intercomparisons with other instruments, *Atmos Chem Phys*, 8(17), 5245–5261, SREF-ID 1680-7324/acp/2008-8-5245. [53]
- KLEIN, B, et al. (2008), The Next Generation of Fast Fourier Transform Spectrometer, in *Proc ISSTT*, vol. 19, URL <http://www.mpifr-bonn.mpg.de/staff/bklein/FFTS/ISSTT2008-FFTS.pdf>. [66]
- KLEIN, U (1993), Aufbau und Betrieb eines breitbandigen, bodengestützten Millimeterwellen-Radiometers zur Messung atmosphärischer Spurenstoffe, Doctoral thesis, Reihe Physik, Shaker Verlag, Aachen, Germany. [89]
- KLEY, D, and EJ STONE (1978), Measurement Of Water-Vapor In Stratosphere By Photo-Dissociation With Ly-Alpha-(1216 Å) Light, *Rev Sci Instrum*, 49(6), 691–697, DOI 10.1063/1.1135596. [28]

- KLEY, D, et al. (1979), In Situ Measurements Of The Mixing-Ratio Of Water Vapor In The Stratospheres, *J Atmos Sci*, 36(12), 2513–2524, DOI 10.1175/1520-0469(1979)036%3C2513:SMOTMR%3E2.0.CO;2. [12, 29]
- KLEY, D, et al. (1982), Transport Of Water Through The Tropical Tropopause, *Geophys Res Lett*, 9(6), 617–620, DOI 10.1029/GL009i006p00617. [30]
- KLEY, D, JM RUSSELL, III, and C PHILLIPS (Eds.) (2000), *SPARC Assessment of Upper Tropospheric and Stratospheric Water Vapour*, WCRP-113, WMO/TD No. 1043, World Meteorol Org, Geneva, Switzerland, URL [http://www.aero.jussieu.fr/~sparc/WAVASFINAL\\_000206/WWW\\_wavas/WavasCompleat.pdf](http://www.aero.jussieu.fr/~sparc/WAVASFINAL_000206/WWW_wavas/WavasCompleat.pdf). [17, 18]
- KOPP, G (2000), Inversion arktischer stratosphärischer Spurengasprofile für die Ozonforschung aus Messungen eines bodengebundenen Mikrowellenradiometers, Doctoral thesis, in *Technik und Umwelt, Wissenschaftliche Berichte*, vol. FZKA 6563, Forschungszentrum Karlsruhe, Germany, URL <http://www-imk.fzk.de/asf/mira/Publicat/Dokus/FZKA6563.pdf>. [65, 97]
- KOZLOV, MG, MA KUSTIKOVA, and KA TOMSKII (2005), Optical Hygrometer, *Measurement Techniques*, 48(7), 731–735, DOI 10.1007/s11018-005-0212-z. [27]
- KRUPA, R (1998), Millimeterwellen-Radiometrie stratosphärischer Spurengase unter Anwendung balancierter Kalibrierung, Doctoral thesis, in *Technik und Umwelt, Wissenschaftliche Berichte*, vol. FZKA 6048, Forschungszentrum Karlsruhe, Germany. [65, 86]
- KUNTZ, M, G HOCHSCHILD, and R KRUPA (1997), Retrieval of ozone mixing ratio profiles from ground-based millimeter wave measurements disturbed by standing waves, *J Geophys Res*, 102(D18), 21,965–21,975, DOI 10.1029/97JD01410. [96, 97]
- KUWAHARA, T, et al. (2008), Ground-based Millimeter-wave Observations of Water Vapor Emission (183 GHz) at Atacama, Chile, *Adv Space Res*, 42, 1167–1171, DOI 10.1016/j.asr.2007.11.030. [41]
- KYRÖLÄ, E, et al. (2004), GOMOS on Envisat: an overview, *Adv Space Res*, 33(7), 1020–1028, DOI 10.1016/S0273-1177(03)00590-8. [50]
- LABITZKE, K (1998), *Die Stratosphäre*, Springer-Verlag, Berlin, Germany. [7]
- LAMBERT, A, et al. (2007), Validation of the Aura Microwave Limb Sounder middle atmosphere water vapor and nitrous oxide measurements, *J Geophys Res*, 112, D24S36, DOI 10.1029/2007JD008724. [42, 47]
- LANGER, J (1995), Charakterisierung eines Radiometers für atmosphärenphysikalische Messungen, Diploma thesis, IUP, Universität Bremen, Germany. [89]
- LE TEXIER, H, S SOLOMON, and RR GARCIA (1988), The role of molecular hydrogen and methane oxidation in the water vapour budget of the stratosphere, *Q J Roy Meteor Soc*, 114(480), 281–295, DOI 10.1002/qj.49711448002. [10]
- LEBLANC, T, IS McDERMID, and RA ASPEY (2008), First-year operation of a new water vapor Raman lidar at the JPL table mountain facility, California, *J Atmos Ocean Tech*, 25(8), 1454–1462, DOI 10.1175/2007JTECHA978.1. [52]
- LIEBE, HJ (1989), MPM — An atmospheric millimeter-wave propagation model, *Int J Infrared Milli*, 10(6), 631–650, DOI 10.1007/BF01009565. [59]
- LIEBE, HJ, GA HUFFORD, and MG COTTON (1993), Propagation Modeling of Moist Air and Suspended Water/Ice Particles at Frequencies Below 1000 GHz, in *AGARD 52nd*

- Specialists Meeting of the Electromagnetic Wave Propagation Panel*, Palma de Mallorca, Spain, URL [http://www.its.bldrdoc.gov/pub/conference\\_papers/AGARD-542\\_liebe\\_hufford\\_cotton\\_1993/index.php](http://www.its.bldrdoc.gov/pub/conference_papers/AGARD-542_liebe_hufford_cotton_1993/index.php). [59, 112]
- LINDNER, K (2002), Messung von stratosphäischem Chlormonoxid und Wasserdampf in der Arktis: Erweiterung und Optimierung des passiven Mikrowellenradiometers RAM in Ny-Ålesund, Spitzbergen, Doctoral thesis, IUP, Universität Bremen, Germany, URL <http://nbn-resolving.de/urn:nbn:de:gbv:46-diss000002681>. [40]
- LUNTAMA, JP, et al. (2008), Prospects of the EPS GRAS Mission for Operational Atmospheric Applications, *B Am Meteorol Soc*, DOI 10.1175/2008BAMS2399.1. [51]
- MASTENBROOK, HJ, and SJ OLTMANS (1983), Stratospheric Water Vapor Variability for Washington, DC / Boulder, CO: 1964-82, *J Atmos Sci*, 40(9), 2157–2165, DOI 10.1175/1520-0469(1983)040%3C2157:SWVFW%3E2.0.CO;2. [24, 25]
- MAY, RD (1998), Open-path, near-infrared tunable diode laser spectrometer for atmospheric measurements of H<sub>2</sub>O, *J Geophys Res*, 103(D15), 19,161–19,172, DOI 10.1029/98JD01678. [34]
- MBL (2008), Adolph Richard Aßmann, in *Magdeburger Biographisches Lexikon*, URL <http://www.uni-magdeburg.de/mbl/Biografien/1452.htm>. [7]
- MEZRIN, MY, and EV STAROKOLTSEV (2001), Aircraft condensation hygrometer and some results of measuring humidity in the zone of the equatorial tropopause, *Atmos Res*, 59, 331–341, DOI 10.1016/S0169-8095(01)00123-5. [24]
- MILOSHEVICH, LM, et al. (2006), Absolute accuracy of water vapor measurements from six operational radiosonde types launched during AWEX-G and implications for AIRS validation, *J Geophys Res*, 111, D09S10, DOI 10.1029/2005JD006083. [20, 22, 26, 123]
- MILZ, M, et al. (2005), Water vapor distributions measured with the Michelson Interferometer for Passive Atmospheric Sounding on board Envisat (MIPAS/Envisat), *J Geophys Res*, 110, D24,307, DOI 10.1029/2005JD005973. [45]
- MOTE, PW, et al. (1995), Seasonal-Variations Of Water-Vapor In The Tropical Lower Stratosphere, *Geophys Res Lett*, 22(9), 1093–1096, DOI 10.1029/95GL01234. [99]
- MOTE, PW, et al. (1996), An atmospheric tape recorder: The imprint of tropical tropopause temperatures on stratospheric water vapor, *J Geophys Res*, 101(D2), 3989–4006, DOI 10.1029/95JD03422. [12]
- MOTTE, E, et al. (2008), A 22 GHz Mobile Microwave Radiometer for the Study of Stratospheric Water Vapor, *IEEE T Geosci Remote*, 46(10), 3104–3114, DOI 10.1109/TGRS.2008.2000626. [40]
- MURPHY, DM, and TT KOOP (2005), Review of the vapour pressures of ice and super-cooled water for atmospheric applications, *Q J Roy Meteor Soc*, 131(608), 1539–1565, DOI 10.1256/qj.04.94. [21]
- MÜLLER, SC, et al. (2008), Validation of stratospheric water vapour measurements from the airborne microwave radiometer AMSOS, *Atmos Chem Phys*, 8(12), 3169–3183, SREF-ID 1680-7324/acp/2008-8-3169. [41]
- NEDOLUHA, GE, et al. (1995), Ground-based measurements of water vapor in the middle atmosphere, *J Geophys Res*, 100(D2), 2927–2939, DOI 10.1029/94JD02952. [41, 70]
- NEDOLUHA, GE, et al. (1996), Measurements of water vapor in the middle atmosphere and

- implications for mesospheric transport, *J Geophys Res*, 101(D16), 21,183–21,193, DOI 10.1029/96JD01741. [40]
- NEDOLUHA, GE, et al. (2007), A comparison of middle atmospheric water vapor as measured by WVMS, EOS-MLS, and HALOE, *J Geophys Res*, 112, D24S39, DOI 10.1029/2007JD008757. [40]
- NOTHOLT, J (1994), The Moon as a light source for FTIR measurements of stratospheric trace gases during the polar night: Application for HNO<sub>3</sub> in the Arctic, *J Geophys Res*, 99(D2), 3607–3614, DOI 10.1029/93JD03040. [44]
- NOTHOLT, J, et al. (2005), Influence of tropospheric SO<sub>2</sub> emissions on particle formation and the stratospheric humidity, *Geophys Res Lett*, 32, L07,810, DOI 10.1029/2004GL022159. [14]
- OAKLEY, T (2008), WMO Catalogue of Radiosondes and upper-air wind systems in use by Members, URL <ftp://ftp.wmo.int/wmo-ddbs/Radiosondes.xls>, retrieved from World Weather Watch (WWW) Programme, Operational Information Service (OIS). [20]
- OELHAF, H, M BIRK, and K PFEILSTICKER (2008), MIPAS-B/TELIS/mini-DOAS, in *SCOUT-O3 Large Balloons Equatorial Field Campaign Newsletter*, edited by H OELHAF, 1, pp. 8–10, URL [http://www.ozone-sec.ch.cam.ac.uk/scout\\_o3/field\\_campaigns/large\\_balloon/newsletter/newsletter1.pdf](http://www.ozone-sec.ch.cam.ac.uk/scout_o3/field_campaigns/large_balloon/newsletter/newsletter1.pdf). [44]
- OLTMANS, SJ, et al. (2000), The increase in stratospheric water vapor from balloonborne, frostpoint hygrometer measurements at Washington, DC, and Boulder, Colorado, *Geophys Res Lett*, 27(21), 3453–3456, DOI 10.1029/2000GL012133. [24, 25]
- PALM, M (2006), Extension and combination of existing remote-sensing instruments, Doctoral thesis, IUP, Universität Bremen, Germany, URL <http://nbn-resolving.de/urn:nbn:de:gbv:46-diss000103890>. [104, 112]
- PETER, T, et al. (2006), When Dry Air Is Too Humid, *Science*, 314(5804), 1399–1402, DOI 10.1126/science.1135199. [17]
- PITERS, A (2007), H<sub>2</sub>O profiles from SCIAMACHY limb, in *Minutes from the Satellite Water Vapour Retrieval Workshop*, edited by D LOYOLA, AT2-01, Deutsches Zentrum für Luft- und Raumfahrt, URL [http://troposat.iup.uni-heidelberg.de:8082/AT2/Announcements/AT2/Reports\\_and\\_papers/2007\\_11\\_H2O\\_Workshop\\_Report.pdf](http://troposat.iup.uni-heidelberg.de:8082/AT2/Announcements/AT2/Reports_and_papers/2007_11_H2O_Workshop_Report.pdf). [50]
- PODOLSKA, JR, GW SACHSE, and GS DISKIN (2003), Calibration and data retrieval algorithms for the NASA Langley/Ames Diode Laser Hygrometer for the NASA Transport and Chemical Evolution Over the Pacific (TRACE-P) mission, *J Geophys Res*, 108(D20), 8792, DOI 10.1029/2002JD003156. [35]
- QUACK, M (2004), Aufbau eines Wasserdampfadiometers und Messung von stratosphärischen Wasserdampfprofilen in den Tropen und in der Arktis, Doctoral thesis, IUP, Universität Bremen, Germany, URL <http://nbn-resolving.de/urn:nbn:de:gbv:46-diss000011040>. [40, 55, 61, 64, 69, 70, 77, 78, 79, 93, 96, 105]
- RANDEL, WJ, et al. (2006), Decreases in stratospheric water vapor after 2001: Links to changes in the tropical tropopause and the Brewer-Dobson circulation, *J Geophys Res*, 111(D12), D12,312, DOI 10.1029/2005JD006744. [14]
- READ, WG, et al. (2007), Aura Microwave Limb Sounder upper tropospheric and lower strato-

- spheric H<sub>2</sub>O and relative humidity with respect to ice validation, *J Geophys Res*, 112, D24S35, DOI 10.1029/2007JD008752. [20, 25, 34, 106]
- RODGERS, CD (2000), *Inverse Methods for Atmospheric Sounding — Theory and Practice*, World Scientific, London, UK. [71, 74, 100]
- RODGERS, CD, and BJ CONNOR (2003), Intercomparison of remote sounding instruments, *J Geophys Res*, 108(D3), 4116, DOI 10.1029/2002JD002299. [112]
- ROEDEL, W (2000), *Physik unserer Umwelt: die Atmosphäre*, 3rd ed., Springer-Verlag, Berlin, Germany. [5]
- ROSCOE, HK (2006), The Brewer-Dobson circulation in the stratosphere and mesosphere — Is there a trend?, *Adv Space Res*, 38(11), 2446–2451, DOI 10.1016/j.asr.2006.02.078. [8, 9]
- ROSENKRANZ, PW (1993), *Absorption of Microwaves by Atmospheric Gases*, pp. 37–90, in JANSSEN (1993a). [58]
- ROSENKRANZ, PW (1998), Water Vapor Microwave Continuum Absorption: A Comparison of Measurements and Models, *Radio Sci*, 33, 919–928, DOI 10.1029/98RS01182, correction in 34, 1025, 1999. [59, 75]
- ROSENLOF, KH (2003), Atmospheric science - How water enters the stratosphere, *Science*, 302(5651), 1691–1692, DOI 10.1126/science.1092703. [36]
- ROSENLOF, KH, and GC REID (2008), Trends in the temperature and water vapor content of the tropical lower stratosphere: Sea surface connection, *J Geophys Res*, 113, D06,107, DOI 10.1029/2007JD009109. [15]
- SAYRES, DS, et al. (2008), A new cavity based absorption instrument for detection of water isotopologues in the upper troposphere and lower stratosphere, URL <http://www.arp.harvard.edu/atmobs/sciobj/instrument/IcosInstrumentPaper.pdf>, part of DS Sayres' dissertation. [36]
- SCHAELEER, B, D OFFERMANN, V KUELL, and M JARISCH (to appear), Global water vapour distribution in the upper troposphere and lower stratosphere during CRISTA 2, *Adv Space Res*, DOI 10.1016/j.asr.2008.06.019. [49]
- SCHERER, M, et al. (2008), Trends and variability of midlatitude stratospheric water vapour deduced from the re-evaluated Boulder balloon series and HALOE, *Atmos Chem Phys*, 8(5), 1391–1402, URL <http://direct.sref.org/1680-7324/acp/2008-8-1391>. [14, 19, 51]
- SCHIEDER, R, V TOLLS, and G WINNEWISSER (1989), The cologne acousto-optical spectrometers, *Exp Astron*, 1(2), 101–121, DOI 10.1007/BF00457985. [65, 80]
- SCHILLER, C, T PETER, and K ROSENLOF (2008), SPARC Water Vapour Initiative, in *SPARC Newsletter*, vol. 30, SPARC International Project Office, Department of Physics, University of Toronto, Canada, URL <http://www.atmosp.physics.utoronto.ca/SPARC/Newsletters.html>, iSSN 1245-4680. [17]
- SCHLICHT, S (2006), Untersuchungen zur Wasser-Partitionierung in Zirruswolken — Feldmessungen und Modellrechnungen, Doctoral thesis, Germany, URL <http://hdl.handle.net/2128/2573>. [34]
- SCHNEIDER, M, F HASE, and T BLUMENSTOCK (2006a), Water vapour profiles by ground-based FTIR spectroscopy: study for an optimised retrieval and its validation, *Atmos Chem Phys*, 6, 811–830, SREF-ID 1680-7324/acp/2006-6-811. [45]
- SCHNEIDER, M, F HASE, and T BLUMENSTOCK (2006b), Ground-based remote sensing of

- HDO/H<sub>2</sub>O ratio profiles: introduction and validation of an innovative retrieval approach, *Atmos Chem Phys*, 6, 4705–4722, SREF-ID 1680-7324/acp/2006-6-4705. [45]
- SEELE, C, and P HARTOGH (2000), A case study on middle atmospheric water vapor transport during the February 1998 stratospheric warming, *Geophys Res Lett*, 27(20), 3309–3312, DOI 10.1029/2000GL011616. [40]
- SEMILETOV, I, et al. (2008), International Siberian Shelf Study 2008 (ISSS-08), *Eos Trans AGU*, 89(53), Fall Meet. Suppl., Abstract U23F-03, URL <http://adsabs.harvard.edu/abs/2008AGUFM.U23F..03S>. [10]
- SHEPHERD, TG (2000), The middle atmosphere, *J Atmos Sol-Terr Phy*, 62(17-18), 1587–1601, DOI 10.1016/S1364-6826(00)00114-0. [12]
- SHEPHERD, TG (2007), Transport in the middle atmosphere, *J Meteorol Soc Jpn*, 85B, 165–191, DOI 10.2151/jmsj.85B.165. [8]
- SIEGENTHALER, A, O LEZEAUX, DG FEIST, and N KAMPFER (2001), First water vapor measurements at 183 GHz from the high alpine station Jungfrauoch, *IEEE T Geosci Remote*, 39(9), 2084–2086, DOI 10.1109/36.951108. [41]
- SILVER, JA, and DC HOVDE (1994), Near-Infrared Diode-Laser Airborne Hygrometer, *Rev Sci Instrum*, 65(5), 1691–1694, DOI 10.1063/1.1144861. [33]
- SITNIKOV, NM, et al. (2007), The FLASH instrument for water vapor measurements on board the high-altitude airplane, *Instrum Exp Tech*, 50(1), 113–121, DOI 10.1134/S0020441207010174. [31]
- SONNEMANN, GR, M GRYGALASHVYLY, and U BERGER (2005), Autocatalytic water vapor production as a source of large mixing ratios within the middle to upper mesosphere, *J Geophys Res*, 110, D15.303, DOI 10.1029/2004JD005593. [11]
- SONNEMANN, GR, et al. (2008), The quasi 5-day signal in the mesospheric water vapor concentration at high latitudes in 2003—a comparison between observations at ALOMAR and calculations, *J Geophys Res*, 113, D04.101, DOI 10.1029/2007JD008875. [11]
- ST. CLAIR, JM, et al. (2008), A new photolysis laser-induced fluorescence instrument for the detection of H<sub>2</sub>O and HDO in the lower stratosphere, *Rev Sci Instrum*, 79(6), 064.101, DOI 10.1063/1.2940221. [31]
- STEINWAGNER, J, et al. (2007), HDO measurements with MIPAS, *Atmos Chem Phys*, 7(10), 2601–2615, SREF-ID 1680-7324/acp/2007-7-2601. [45]
- STEVENS, MH, et al. (2008), First UV satellite observations of mesospheric water vapor, *J Geophys Res*, 113, D12.304, DOI 10.1029/2007JD009513. [50]
- STRAUB, C (2008), Development of a 22 GHz correlating Radiometer for the observation of Stratospheric Water Vapor, Diploma thesis, IAP, Universität Bern, URL <http://www.iap.unibe.ch/publications/pub-detail.php?lang=en&id=3065>. [40]
- TERENIN, A, and H NEUJMIN (1934), Photodissociation of Molecules in the Schumann Ultra-Violet, *Nature*, 134(3381), 255, DOI 10.1038/134255c0. [29]
- THORNBERRY, T, RS GAO, and D FAHEY (2008), Measurement of low water-vapor mixing ratios using mass spectrometry, CIRES winning proposal for the Innovative Research Program 2008, URL <http://cires.colorado.edu/science/pro/irp/2008/thornberry/>. [36]
- TROLLER, M, et al. (2006), Tomographic determination of the spatial distribution

- of water vapor using GPS observations, *Adv Space Res*, 37(12), 2211–2217, DOI 10.1016/j.asr.2005.07.002. [50]
- URBAN, J, et al. (2007), Global observations of middle atmospheric water vapour by the Odin satellite: An overview, *Planet Space Sci*, 55(9), 1093–1102, DOI 10.1016/j.pss.2006.11.021. [43]
- Vaisala (2006), Vaisala Radiosonde RS92-SGP, *Technical Report B210358EN-C*, Vaisala Oyj, URL <http://www.vaisala.com/weather/products/soundingequipment/radiosondes/rs92/vaisalaradiosonders92-sgpbrochure.pdf>. [20]
- VOGELMANN, H, and T TRICKL (2008), Wide-range sounding of free-tropospheric water vapor with a differential-absorption lidar (DIAL) at a high-altitude station, *Appl Opt*, 47(12), 2116–2132, DOI 10.1364/AO.47.002116. [53]
- VÖMEL, H, et al. (2003), The behavior of the Snow White chilled-mirror hygrometer in extremely dry conditions, *J Atmos Ocean Tech*, 20(11), 1560–1567, DOI 10.1175/1520-0426(2003)020<1560:TBOTSW>2.0.CO;2. [26]
- VÖMEL, H (2006), Water Saturation Vapor Pressure Formulations, URL <http://cires.colorado.edu/~voemel/vp.html>. [123]
- VÖMEL, H, DE DAVID, and K SMITH (2007a), Accuracy of tropospheric and stratospheric water vapor measurements by the cryogenic frost point hygrometer: Instrumental details and observations, *J Geophys Res*, 112, D08,305, DOI 10.1029/2006JD007224. [17, 19, 24, 25, 26]
- VÖMEL, H, et al. (2007b), Validation of Aura Microwave Limb Sounder water vapor by balloon-borne Cryogenic Frost point Hygrometer measurements, *J Geophys Res*, 112, D24S37, DOI 10.1029/2007JD008698. [26]
- WANG, MJ, et al. (2002), Performance Characterization of a 600–700 GHz SIS Mixer, in *Proc ISSTT*, vol. 13, pp. 445–452, Harvard University, Cambridge, MA, USA, URL <http://www.asiaa.sinica.edu.tw/~mingjye/dir-2/MJW-C8.pdf>. [44]
- WATERS, JW, et al. (1999), The UARS and EOS microwave limb sounder (MLS) experiments, *J Atmos Sci*, 56(2), 194–218, DOI 10.1175/1520-0469(1999)056<0194:TUAEML>2.0.CO;2. [42]
- WAYNE, RP (2000), *Chemistry of Atmospheres*, 3rd ed., Oxford University Press, Oxford, UK. [15]
- WEBSTER, CR, and AJ HEYMSFIELD (2003), Water isotope ratios D/H, O-18/O-16, O-17/O-16 in and out of clouds map dehydration pathways, *Science*, 302(5651), 1742–1745, DOI 10.1126/science.1089496. [36]
- WEINSTOCK, EM, et al. (1994), New Fast-Response Photofragment Fluorescence Hygrometer For Use On The Nasa Er-2 And The Perseus Remotely Piloted Aircraft, *Rev Sci Instrum*, 65(11), 3544–3554, DOI 10.1063/1.1144536. [30]
- WEINSTOCK, EM, et al. (2008), An intercomparison of water vapor measurements in the TTL and lower tropical stratosphere during AVE-WIIF, CRAVE and TC4, URL <http://avdc.gsfc.nasa.gov/PDF2/AuraST2008/Posters/Weinstock.pdf>, poster presentation at the EOS Aura Science Team Meeting, Columbia, MD, USA. [18]
- WHITEMAN, DN, et al. (2006), Raman lidar measurements during the International

- H2O Project. Part II: Case studies, *J Atmos Ocean Tech*, 23(2), 170–183, DOI 10.1175/JTECH1838.1. [52]
- WOHLTMANN, I (2002), Ozone depletion, chlorine activation and water vapor observed in Spitsbergen, Doctoral thesis, IUP, Universität Bremen, Germany, URL <http://nbn-resolving.de/urn:nbn:de:gbv:46-diss000003258>. [56, 69, 70]
- YUSHKOV, V, et al. (1995), Optical fluorescent hygrometer for water vapor low concentration measurements, in *Air Pollution and Visibility Measurements, Proc SPIE*, vol. 2506, edited by P FABIAN, V KLEIN, M TACKE, K WEBER, and C WERNER, pp. 783–794, DOI 10.1117/12.221083. [31]
- ZUBER, A, and G WITT (1987), Optical hygrometer using differential absorption of hydrogen Lyman- $\alpha$  radiation, *Appl Opt*, 26(15), 3083–3089, URL <http://www.opticsinfobase.org/abstract.cfm?URI=ao-26-15-3083>. [27]
- ZÖGER, M, et al. (1999), Fast in situ stratospheric hygrometers: A new family of balloon-borne and airborne Lyman alpha photofragment fluorescence hygrometers, *J Geophys Res*, 104(D1), 1807–1816, DOI 10.1029/1998JD100025. [19, 30]